Rheological, Mechanical and Physico-chemical Behavior of Fibrous Materials

BY

ALEXANDER KOLBASOV

B.S., Illinois Institute of Technology, 2010

THESIS

Submitted as a partial fulfillment of the requirements for the degree for Doctor of Philosophy in Mechanical Engineering in the Graduate College of the University of Illinois at Chicago, 2019

Chicago, Illinois

Defense Committee:

Alexander L. Yarin	Chair and Advisor
Kenneth Brezinsky	Mechanical and Industrial Engineering, UIC
Suman Sinha-Ray	Mechanical and Industrial Engineering, UIC
W. J. Minkowycz	Mechanical and Industrial Engineering, UIC
Kumar Natesaiyer	United States Gypsum

I dedicate this thesis to my parents Dimitri and Julia Kolbasov without whose support it would not have happened

ACKNOWLEDGEMENTS

First, I would like to express my gratitude to my advisor. Professor Alexander Yarin for being my mentor and for pushing me to continuously improve. Without his guidance and help this dissertation would not be possible. I would also like to thank my thesis committee members for their suggestions and assistance.

Portions of this thesis have been published in peer reviewed journals. Section 2.1, 3.1, and Chapter 4 were published in Rheologica Acta (Kolbasov A., Comiskey P., Sahu R., Sinha-Ray S., Yarin A., Sikarwar B., Kim S,. Jubery T,. Attinger D. (2016) Blood rheology in shear and uniaxial elongation. Rheologica Acta, 55(11-12), 901-908). Sections 2.2, 3.2, and Chapter 5 were published in Engineering Chemistry Research (Kolbasov, A., Sinha-Ray, S., Joijode, A., Hassan, M. A., Brown, D., Maze, B., Pourdeyhimi, B., and Yarin, A. L. (2016) Industrial-scale solution blowing of soy protein nanofibers. Industrial & Engineering Chemistry Research 55, 1, 323–333). Sections 2.3, 3.3 and Chapter 6 were submitted for publication in Nano Letters. Sections 2.4, 3.4 and Chapter 7 were published in the Journal of Membrane Science (Kolbasov, A., Sinha-Ray, S., Yarin, A. L., & Pourdeyhimi, B. (2017). Heavy metal adsorption on solution-blown biopolymer nanofiber membranes. Journal of Membrane Science, 530, 250-263.) Sections 2.5, 3.5 and Chapter 8 were published in the Journal of Mechanics and Physics of Solids (Kolbasov, A., Sinha-Ray, S., & Yarin, A. L. (2019). Theoretical and experimental study of punched laminate composites protected by outer paper layer. Journal of the Mechanics and Physics of Solids, 128, 117-136). Permission letters given by the publisher are in Appendix C.

CONTRIBUTION OF AUTHORS

The work on the viscoelasticity of blood in sections 2.1, 3.1, and Chapter 4 were previously published in Rheologica Acta (Kolbasov A., Comiskey P., Sahu R., Sinha-Ray S., Yarin A., Sikarwar B., Kim S,. Jubery T,. Attinger D. (2016) Blood rheology in shear and uniaxial elongation. Rheologica Acta, 55(11-12), 901-908) for which I am the primary author and conducted the shear and elongational viscosity experiments data analysis and wrote the manuscript. Dr. Comiskey assisted in performing the experiments. Dr. Sinha-Ray, Dr. Yarin and Dr. Attinger contributed to the writing of the manuscript. Sections 2.2, 3.2, and Chapter 5 were published in Engineering Chemistry Research (Kolbasov, A., Sinha-Ray, S., Joijode, A., Hassan, M. A., Brown, D., Maze, B., Pourdeyhimi, B., and Yarin, A. L. (2016) Industrial-scale solution blowing of soy protein nanofibers. Industrial & Engineering Chemistry Research 55, 1, 323–333) for which I am the primary author and conducted the experiments performed SEM analysis and wrote the manuscript. Mr. Hassan, Mr Brown and Maze assisted in performing the experiment. Dr. Joijode assisted in the experiment and contributed to the manuscript. Dr. Sinha-Ray, Dr. Yarin and Dr. Pourdeyhimi also contributed to writing the manuscript. Sections 2.3, 3.3 and Chapter 6 are unpublished. Sections 2.4, 3.4 and Chapter 7 were published in the Journal of Membrane Science (Kolbasov, A., Sinha-Ray, S., Yarin, A. L., & Pourdeyhimi, B. (2017). Heavy metal adsorption on solution-blown biopolymer nanofiber membranes. Journal of Membrane Science, 530, 250-263.) for which I am the primary author. I produced the materials designed and performed the experiment SEM imagery data analysis and wrote the manuscript. Dr. Sinha-Ray, Dr. Yarin and Dr. Pourdeyhimi also contributed to writing the manuscript. Sections 2.5, 3.5 and Chapter 8 were published in the Journal of Mechanics and Physics of Solids (Kolbasov, A., Sinha-Ray, S., & Yarin, A. L. (2019). Theoretical and experimental study of punched laminate composites protected by outer paper layer. Journal of the Mechanics and Physics of Solids, 128, 117-136) for which I am the primary author. I

designed and built the experimental setup, performed all experiments and data analysis and wrote the manuscript. Dr. Sinha-Ray and Dr. Yarin also contributed to writing the manuscript.

TABLE OF CONTENTS

TABLE OF CONTENTS (continued)

TABLE OF CONTENTS (continued)

LIST OF FIGURES

LIST OF FIGURES (continued)

FIGURE PAGE

LIST OF FIGURES (continued)

FIGURE PAGE

LIST OF FIGURES (continued)

LIST OF FIGURES (continued)

FIGURE PAGE

LIST OF FIGURES (continued)

FIGURE PAGE

LIST OF TABLES

TABLE PAGE

SUMMARY

The goal of this work is to widen the understanding of various physical mechanisms associated with fibrous materials. These aspects involve the production, characterization and application of said materials. In the first part of the thesis the rheological behavior of blood is investigated. In particular, its viscoelastic behavior which is also an essential requirement for the spinnability of a material for fiber formation. The viscoelastic behavior of blood has significant applications in forensic science and crime scene investigation. Several novel experimental setups were designed, built and used to form threads and fibers of viscoelastic liquids and to study their behavior. In the second part, it was shown that the novel fiber forming process of solution blowing can be scaled up to industrial levels. This development leads to a significant increase in the nanofiber production rate, which holds great promise for such fields as water treatment and energy storage. In the third part, a novel application of solution blowing for energy storage applications is described. Solution blowing is used to form ceramic nanofibers for use in batteries as solid electrolytes. The effect of salts on the viscoelasticity and spinnability of the spun solution is investigated and the performance of the produced solid electrolyte is characterized. In the fourth part, solution blowing is used to produce multiple novel fibrous materials for applications in water purification. Nanofibers containing various biomaterials are spun into large membranes and their capacity for heavy metal adsorption is elucidated. A novel kinetic model for adsorption on such membranes is also developed and verified experimentally. In the last part, a novel method for the characterization of thin fibrous materials, is developed. The method allows for measurements of such mechanical parameters as Young's modulus and Poisson's ratio of fibrous materials under compression in the off-plane direction.

1. INTRODUCTION

1.1 Fibrous Materials

Fibrous material are complex composite materials with inhomogeneous structure which represent a wide field in the materials science. As a result, in order to engineer a fibrous material for a given purpose multiple aspects of its mechanical behavior must be elucidated. Depending on the application, such aspects may involve individual fiber formation followed by the fiber-to-fiber interaction, which comprises the desired material. Once the material is formed, its micro- and macroscopic mechanical behavior must be understood. The results of this work are related to the fiber/thread and nanofiber formation processes, and fibrous materials comprised of multiple fibers. This work develops methods of novel nanofiber formation. It also develops several novel applications of various nanofibers, as well as introduces novel methods of characterization of fibrous materials. Accordingly, this work significantly expands industrial horizons for the new applications of fibrous materials, their formation and characterization.

1.2 Viscoelasticity of blood

Detailed understanding of blood rheology is important in medicine, because it determines the blood flow structure and affects viscous dissipation during blood circulation, as well as clot formation, etc. For instance, shear-thinning effects are known to affect blood flow and the wall shear stress in coronary arteries.

Similarly, blood rheology is important for forensic disciplines, such as bloodstain pattern analysis (BPA). The US National Academies recently advocated National Research Council USA 2009 for stronger scientific foundations of BPA, given “the complex nature of fluid dynamics.” Indeed, rheology affects most aspects of blood spatter originating from crime

or accident, Specifically, blood rheology determines significantly the pattern of: (a) blood dripping process, where blood viscosity and elasticity control the final stages of drop formation; (b) breakup of blood jets and sheets, especially in transition from dripping to jetting; (c) the oscillations of drops during flight; (d) behavior of droplets and jets upon impact; and (e) the evaporation-driven flow in drying bloodstains. Accordingly, understanding of blood rheology is important for crime scene reconstruction. It should be emphasized that blood flow pattern is significantly influenced by the blood rheology in the situations where the Reynolds, Deborah, or capillary numbers are sufficiently large.

1.3 Industrial-scale solution blowing

The effect of viscoelasticity in blood rheology are significant. However, viscoelasticity plays an even greater role in fiber forming processes, such as solution blowing. It should be emphasized that solution blowing is a novel technique which widely extended material repertoire of nanofiber-based materials. For example, it allows one to develop biocompatible and biodegradable nonwovens formed from biopolymer-containing nanofibers. However, until solution blowing was demonstrated only on laboratory-scale devices. The scale-up of solution blowing of biopolymer-containing nanofiber nonwovens to the industrial level represents a significant step in the development of this method for commercial applications.

1.4 Solution blowing ceramic solid-state electrolytes

Energy storage is potentially one of the biggest challenges facing mankind in this century. An improvement in battery technology allowed for development of smart phones and electric cars. These developments were made possible by the use of Lithium ion batteries. However, as the fires onboard of Boeing 787 and self-ignitions of Samsung Galaxy 7 showed,

these batteries have significant safety problems. Solid-state electrolytes hold great promise of remediating these problems to sustain both high performance and safety. Ceramic nanofibers were useful for improving performance of solid-state electrolytes. However, production of such electrolytes using electrospinning significantly limited their feasibility due to low production rates. The scalable solution blowing will allow for an increased production rate by orders of magnitude higher than that of electrospinning which is a significant step toward commercial production of improved solid-state electrolytes for battery technologies.

1.5 Heavy Metal Adsorption on Solution-Blown Biopolymer Nanofiber Membranes

Removal of heavy metals from industrially-polluted waters is a pressing problem worldwide. Many key industries, such as mining, alloys and steel manufacturing, electroplating, electronics facilities, fertilizer production, etc. release a wide variety of heavy metals into the environment. Heavy metal ions pollute water in lakes and rivers, are transported by ground water, and are accumulated in soil, plants, fish and chitin and chitosan in the exoskeletons of crabs, lobsters and shrimps, as well as squids and octopuses, thus entering the food chain. Heavy metals remain in nature over long periods of time. Heavy metals are known to be severe health hazards and cause severe damage to human organisms, in particular, to liver (in the form of copper poisoning), kidney (in the form of cadmium poisoning), or nervous system (as a result of lead poisoning). Nevertheless, the key industries mentioned above, are inevitable and essential for maintaining and enhancement of the economy of developed and developing countries. This makes sustaining water purity an important goal, which should be achieved efficiently and cost-effectively, for which solution-blown biopolymer nanofiber membranes might be a key.

The reason behind the toxicity of heavy metals is in their tendency to attach to the molecules inside of living organisms and interfere with body functioning. This makes the use of adsorptive biowaste-derived nanofibers for heavy metal removal such a desirable goal. Biowaste possesses an intrinsic capability of adsorbing heavy metals without any pretreatment or chemical synthesis. The yield of the adsorption processes is higher, especially facilitated by a higher surface are of nanofibrous membranes. It should be emphasized that nanofibrous adsorbents are fixed, in distinction from high-surface area powders which are easily swept away by flow. The expended repertoire of spinnable materials in solution blowing, including biowaste-derived solutions, as well as high production rates, makes such nonwovens promising filtration medium for heavy metals.

1.6 Importance of paper properties in the off-plane (z-) direction

In addition to their chemical functionality, mechanical behavior of fibrous materials is extremely important. However, any such materials (e.g., paper), are planar, i.e. extend in the in-plane (x- and y-) directions and are very thing in the off-plane z-direction. Accordingly, such material are un-isotropic, whereas their mechanical behavior in the z-direction cannot be studied using the existing approaches. In particular, in the case of paper used as the outer layers in gypsum wallboard mechanical behavior in the z-direction is of utmost importance, and thus the main motivation of this section of the present thesis. It should be emphasized that paper consists of one or more layers of intertwined cellulose fibers and is used a diverse field of applications starting from printing and going to packaging and construction. Specifically, paper is often used as a laminate component and its properties in the z-direction contribute to the overall performance of the material, in particular, wallboard.

2. BACKGROUND AND LITERATURE REVIEW

2.1 Blood Rheology in Uniaxial Elongation

(This section has been previously published in Kolbasov A., Comiskey P., Sahu R., Sinha-Ray S., Yarin A., Sikarwar B., Kim S,. Jubery T,. Attinger D. (2016) Blood rheology in shear and uniaxial elongation. Rheologica Acta, 55(11-12), 901-908)

Blood is one of the most common liquids, with relevance to disciplines as varied as the food industry, medicine and forensics. Blood is a complex aqueous liquid, with about half of its volume consisting of micrometer-size particles such as red and white blood cells. An indicator of the concentration of particles in the blood is the hematocrit, which is the relative volume of red blood cells versus the total blood volume (Bevel and Gardner 2008, Walker et al. 1990). Blood also starts coagulating as soon as it flows out of the human body.

Several properties of blood have been already characterized. The density of blood,1060 kg/m^3, is close to that of water. Blood is known to be a non-Newtonian fluid, i.e. a fluid with a viscosity that varies with the flow conditions. The shear viscosity of blood decreases with shear rate in the simple-shear flow, i.e. blood is a shear-thinning fluid. Blood viscosity also increases with increasing hematocrit and decreasing temperature. Based on measurements, the following correlation has been proposed for the shear viscosity of blood: $\mu = \mu_{ref}\, g(H) f(\dot{\gamma}) k(T)$, where $\mu_{ref}$is the viscosity at a reference level of temperature (typically 37°C), and the functions *g*, *f* and *k*, model the dependencies of blood viscosity on hematocrit, shear rate, and temperature, respectively(Gruttola et al. 2005). Other empirical correlations are available, for instance in Charm and Kurland (1965) based on Casson's equation, to describe the measured viscosity of human blood for shear rates from 2 s^{-1} to 10^5 s^{-1}.While many publications have addressed the shear-thinning aspects of blood rheology(cf. Gruttola et al. 2005; Charm and Kurland 1965),

few have described blood as a viscoelastic fluid (Chien et al. 1975; Brust et al. 2013 and Copley et al. 1975).

A detailed understanding of the blood rheology is important in biology, where it plays a role in the flow structure and affects viscous dissipation during circulation (Chien et al. 1975). For instance, shear thinning effects are known to affect blood flow and the wall shear stress in coronary arteries (Johnston et al. 2004). Similarly, blood rheology matters for forensics disciplinessuch as bloodstain pattern analysis, a discipline for which the US National Academies recently advocated (Committee on Identifying the Needs of the Forensic Sciences Community, National Research Council 2009) for stronger scientific foundations, given “the complex nature of fluid dynamics”. Indeed, rheology affects most aspects of a bloody crime or accident, such as (a) blood’s dripping process, where viscosity and elasticity control the final stages of the drop formation(Thoroddsen et al. 2008), (b) the breakup of jets (Lin and Reitz 1998; Eggers and Villermaux 2008) and sheets(Lin and Reitz 1998; Eggers and Villermaux 2008; Rein 1993), especially in the transition from dripping to jetting(Clasen et al. 2009), (c) the oscillations of dropsduring flight (Attinger et al. 2000) (d) the fate of droplets and jets upon impact(Chen and Li 2010; Caviezel et al. 2008; Bartolo et al. 2006 and Yaril 2005), and (e) the evaporation-driven flow in drying bloodstains(Allain and Limat 1995). Understanding of the rheology of blood is therefore important for crime scene reconstruction. Attinger et al. (2013) provides values of shear rates relevant to bloodstain pattern analysis. Indeed, blood flow will be significantly influenced by blood rheology in any situation where the Reynolds, Deborahor capillary numbers have finite values.

For polymer solutions, viscoelasticity is typically caused by coil-stretch transition ofmacromolecules, which happens in strong elongational flows (De Gennes 1974). For blood, there is no clear link between its viscoelasticity and its microscopic or molecular structure, which explains the mostly phenomenological rheological approach adopted in hemodynamics

(Apostolidis and Beris 2014; Yilmaz and Gundogdu 2008; Merrill 1969; Meiselman et al. 2007). Recently, Brust et al. (2013) measured with a custom-made capillary breakup extensional rheometer a relaxation time of 7.8 ± 0.6 ms and 1.5 ± 0.2 ms for respectively,human blood and blood plasma, both at 37 ºC.This result shows that whole blood and blood plasma can beviscoelastic. Viscoelasticity might influence blood spatters and bloodstain pattern analysis.For instance, viscoelasticity influencesthe deformation, spreading and atomization of drops according to the dataavailable in Bertola (2009); Jiang et al. (2010); Yue et al. (2006); Cooper-White et al. (2002) ; Joseph et al. (1999); Mighri et al. (1998) and Carre et al. (1996). In this manuscript, we measure the rheology of swine blood in shear and uniaxial elongation. Swine blood is a safer substitute for human blood, with physiological and physicalproperties comparable to humanblood(Behrooz et al. 2011) and Windberger et al. 2003).For instance, the red blood cells in swine blood and human blood assemble in rouleaux at low shear rates, contrary to the blood of cattle and sheep(Huang et al. 1987; Wickham et al. 1990 and Williams and Taylor 2013).

2.2 Industrial-scale solution blowing of soy protein nanofibers

(This section has been previously published in Kolbasov, A., Sinha-Ray, S., Joijode, A., Hassan, M. A., Brown, D., Maze, B., Pourdeyhimi, B., and Yarin, A. L. (2016) Industrial-scale solution blowing of soy protein nanofibers. Industrial & Engineering Chemistry Research 55, 1, 323–333)

For a long time meltblowing is considered as the most important commercial method of forming nonwovens comprised of micro- and nanofibers. These fibers are aerodynamically-blown using several petroleum-derived molten polymers, mostly polypropylene, but also such materials as polyester, polyamide, polyurethane, thermoplastic elastomers, polyethylene, ethylene, and different copolymers (Yarin et al. 2014; Pinchuk et al 2002). On the other hand, aerodynamic blowing of polymer

solutions to form nonwovens comprised of polymer nanofibers is a relatively new technique (Yarin et al. 2014; Sinha-Ray et al. 2010; Zhuang et al. 2013; Oliveira et al. 2012; Behrens et al. 2014). Subsonic solution blowing of petroleum-derived polymers results in nonwovens comprised of nanofibers with cross-sectional diameters of the order of 100 nm, whereas supersonic solution blowing is capable of reducing nanofiber diameter to the 20-50 nm range (Sinha-Ray et al. 2013). The fundamental theory of solution blowing process and numerical results obtained in its framework were published recently (Sinha-Ray et al. 2015).

It should be emphasized that solution blowing widely extended material repertoire of nanofiber forming and rapidly aimed biocompatible and biodegradable nonwovens formed from biopolymer-containing nanofibers. For example, such biopolymers as the plant-derived soy protein, lignin, zein and cellulose acetate, as well as the animal-derived silk protein (sericin) and bovine serum albumin were solution blown (Medeiros et al. 2009; Sinha-Ray et al. 2011; Sinha-Ray et al. 2012; Khansari et al. 2012; Khansari et al. 2013; Zhang et al. 2013). However, all these works operated only laboratory-scale devices, and scale-up of solution blowing of biopolymer-containing nanofiber nonwovens to the industrial level has not been demonstrated so far, as to our knowledge.

The present work aims solution blowing of soy protein-poly(ethylene oxide) nanofibrous nonwovens using multi-orifice nosepieces made by BIAX-Fiberfilm Corporation. The following two section describe the experimental details. Then, results and discussion are presented. The theoretical aspects are discussed next. After that conclusions are drawn in the final section.

2.3 Solution blowing ceramic solid-state electrolytes – towards mass production

With the trend to developing battery technology to higher energy density level, the concern on the safety issues always follows. Thus, considerable research has focused on replacing the flammable liquid electrolytes with solid electrolytes. To date, numerous solid electrolytes haven been developed, which includes organic polymers (Liu et al. 2015; Cheng et al. 2018; Mindemark et al. 2018), inorganic sulfides (Hood et al. 2018; Kamaya et al. 2011; Chang et al.

2018; Kudu et al. 2018), oxides (Thangadurai and Weppner 2006; Thangadurai and Narayanan 2014; Inaguma et al. 1993) and so on (Manthiram et al. 2017; Maekawa et al. 2009). Among all these electrolytes, oxide based solid electrolytes have attracted high interest due to several advantages: Oxide solid electrolytes have fast Li-ion conductivity (> 10^{-4}S cm^{-1}) at room temperature (Stramare et al. 2003). Their wide electrochemical stability window (Thangadurai and Narayanan 2014) could maximize the energy density of the Li batteries. More importantly, oxide based electrolytes own high stiffness to prevent the Li dendrite growth (Khurana et al. 2014; Monroe and Newman 2005), thus solve the major safety issue of Li metal battery. The nonflammability nature and high stability at wide range of temperatures of oxide electrolytes could also ensure the batter safety and expand the potential application to all kinds of environments.

Conventionally, ceramic solid-state electrolytes (SSE) are produced through solid state reaction method (Sharafi et al. 2016; Sharafi et al. 2017; Cheng et al. 2014), which is simple and ease to large-scale production. However, this approach includes repeated long time and high temperature calcination (Baek et al. 2014; Gao et al. 2018), results in huge energy consumption. In addition, coarse grains (Gao et al. 2018) and impurities caused by the huge Li loss at high temperature (Gao et al. 2018; Kotobuki et al. 2011; Larraz et al. 2013) are also negligible issues. Wet chemical processes (Kim et al. 2015; Lin et al. 2016; Jin and McGinn 2013; Han et al. 2017; Fu et al. 2017; Zhang et al. 2017) are also important approaches to achieve the ceramic SSE with better control of chemical composition and morphology (Lin et al. 2016; Rosero-Navarro and Tadanaga 2018). However, the time consuming (Jin and McGinn 2013; Li et al. 2017) issue still exist. Meanwhile, the yield is lower and largely subject to the size of the reactor (Joseph et al. 2018). Some other ways like physical or chemical deposition (Lü et al. 2016; Oudenhoven et al. 2011) and electrospinning (Liu et al. 2015; Liu

et al. 2017 Liu et al. 2017) have all been described to form good processability of ceramic SSE. However, the mass production from these methods is hard to reach.

Solution blowing is a novel method appropriate for mass production of nanofibers (Sinha-Ray et al. 2010; Sinha-Ray et al. 2011; Yarin et al. 2014; Kolbasov et al. 2016; Tiwari et al. 2009). It is significantly faster than electrospinning (Tiwari et al. 2009) and in distinction from the latter is driven aerodynamically, rather than electrically. In this work, solution blowing technique has been utilized to mass produce ceramic solid-state electrolyte for the first time. A typical perovskite type solid electrolyte lithium lanthanum titanite ($Li_{3x}La_{(2/3)-x(1/3)-2x}TiO_3$ (LLTO was chosen as a target material, where the detailed composition of LLTO is further chosen by the reported high ionic conductivity cubic LLTO with the formula $Li_{0.33}La_{0.557}TiO_3$. The solution blowing parameter for fiber mat has been detailed studied to guide the future works. The received ceramic fiber mat were investigated by X-ray diffraction (XRD) and Scanning Transmission Electron Microscopy (STEM) to show its good crystallinity. The ceramic fibers were later mixed into PVDF-co-HFP polymer to form composite polymer electrolyte (CPE). The LLTO fiber enhanced CPE membrane shows great thermal stability, ion conductivity as well as extremely long cycle life against Li metal at a relatively low overpotential.

2.4 Heavy Metal Adsorption on Solution-Blown Biopolymer Nanofiber Membranes

(This section has been previously published in Kolbasov, A., Sinha-Ray, S., Yarin, A. L., & Pourdeyhimi, B. (2017). Heavy metal adsorption on solution-blown biopolymer nanofiber membranes. Journal of Membrane Science, 530, 250-263.)

The availability of clean drinking water is an ever growing concern. According to Environmental Business International, the annual market for heavy metal removal industry in USA is nearly $55 billion, whereas the industrial waste water treatment market is nearly as big

as $1.8 billion to meet the EPA standard. Despite a United Nations resolution establishing human right to water as an essential human right, according to some estimates, over four billion people will live without a sufficient source of clean water by the year 2025 (Friberg and Elinder 1985). In particular, the water shortage is due to a continuous contamination of rivers and lakes with heavy metals by the industrial run off. Critical industries such as mining, metallurgical, alloys and steel manufacturing, electroplating, electronics, fertilizer production, etc. release a wide variety of heavy metals into the environment (Garg et al. 2007) [3]. Heavy metals do not degrade, and remain in nature over a long time ((Friberg and Elinder 1985; Garg et al. 2007) accumulating in soil, plants and animal wildlife. Heavy metals are known to be severe health hazards and cause severe damage to the human body. The damage can be caused to the liver by copper poisoning, to the kidney by cadmium (Kurniawan et al. 2006), or lead to the deterioration of the nervous system as a result of the lead poisoning (Fu and Wang 2011).

Multiple industries are responsible for lead pollution in water. To name a few, these are printed circuit industry (via solder plating and etching operations), different electronics assembly plants (via solder flux cleaning), battery recycling plants, and landfill leachate (via organometallics, such as tetraethyl lead). Old paints used in building also contain lead. As a result, demolition wallboards which are dumped in landfill can also contain lead. In addition, most of the old water delivery pipes contain lead. On being corroded, these pipes can leach lead into drinking water. Therefore, water remediation from lead ions and the related safety issues are quite acute. Accordingly, the administrative regulations of waste water discharge have become very strict (Barakat 2011). The scientific view is that any amount of lead, how minimal it may be, is bad in drinking water. However, according to WHO, the legal limit of lead in water is 10 ppb and according to EPA, that amount is 15 ppb.

One of the most severe damages was caused in Minamata City of Japan, where a huge outbreak of the Minamata disease was linked to a continuous release of methylmercury for

over almost 40 years by Chisso Corporation's industrial wastewater into Minamata Bay and the Shiranui Sea. There is a more recent example of a contamination event in Flint, Michigan. There as the authorities switched the water supply, the pipes delivering drinking water got contaminated with lead and resulted in a complete disruption of water supply in the city. The total cost of this crisis was estimated as about $400M. Another significant problem with potable water exists in various parts of India, where water is contaminated by severe arsenic poisoning. As a result, significant efforts were directed onto research of new methods for limiting the discharge of heavy metals and purification of contaminated water.

A number of methods of purification of waste water have been proposed and explored in the past. These methods include chemical precipitation, adsorption, ultra-filtration, reverse osmosis, ion exchangers, chemical oxidation/reduction and electro-dialysis (Farooq et al. 2010; Sud et al. 2008; Gardea-Torresdey et al. 2000; Zhang et al. 1998; Patterson 1985). The equipment for all these methods is costly, the processes typically involve the extremely high capital costs, and each one of them has significant drawbacks. One such example is chemical precipitation, the most commonly used method of water purification, which has two significant limiting factors. First, this method results in a toxic sludge as a by-product, the disposal of which is expensive. Second, it is effective in removing large quantities of metal from water but only up to the solubility limit of the precipitate, which is on the order of 10 ppm for most heavy metals. This is by orders of magnitude above the allowed limit for water.

Due to the above-mentioned reasons, the application of bioabsorbents extracted from agricultural waste would be very attractive. Multiple industries create animal or plant-derived waste during their operation, and a proper disposal of these biomaterials incurs additional costs. It was already demonstrated that many of these biomaterials can be used for heavy metal adsorption with or without chemical modification (Ngah and Hanafiah 2008). The abundance

of bio-waste sources makes them ideal for low-cost water purification purposes (Bailey et al. 1999, Babel and Kurniawan 2003).

The higher the surface area of an adsorbent is, the higher is the yield of the adsorption processes. This factor makes production of agro-waste-based adsorbents with high surface area, such as in nanofibers/nanofiber-based nonwovens extremely desirable. Such a novel process of mass production of the agrowaste-based nanofibers was recently developed using solution blowing, in which soy proteins and other biopolymers were transformed into nanofiber mats (Khansari et al. 2013; Sinha-Ray et al. 2010; Sinha-Ray et al. 2011; Khansari et al. 2012; Sinha-Ray 2012; Khansari et al. 2013, Yarin et al. 2014). In particular, soy proteins are a relatively inexpensive and abundant by-product of biodiesel produced from soy (Klass 1998; Ahmend et al. 1994). Soy proteins are already used in plastics, fillers and adhesives (Johnson et al. 1984; Kalapathy et al. 1995; Hettiarachchy et al. 1995), and solution blowing of soy-containing nanofiber mats possessing high surface area is a logical step in further utilization of soy, for example as nano-textured bio-adsorbents. Moreover, our group recently demonstrated that solution blowing of soy protein nanofibers can be scaled up to the industrial level (Kolbasov et al. 2016). There are indications that multiple other bio-adsorbents can be transformed into nanofiber-based nonwovens (Ignatova et al. 2013; Haider and Park 2009; Devarayan et al. 2013) and used for metal extraction from polluted water (Guo et al. 2008). Here it is demonstrated that such biopolymers as lignin, oats, soy protein, sodium alginate and chitosan can form nano-textured membranes which are effective in heavy metal adsorption from aqueous solutions. As an example of a heavy metal solution, lead solution is used in the present work. The novel physico-chemical aspects of metal ion adsorption on such biopolymers are also addressed.

2.5 Theoretical and Experimental Study of Punched Laminate Composites Protected by Outer Paper Layer

(This section has been previously published in Kolbasov, A., Sinha-Ray, S., & Yarin, A. L. (2019). Theoretical and experimental study of punched laminate composites protected by outer paper layer. Journal of the Mechanics and Physics of Solids, 128, 117-136)

Lightweight laminate composites allow manufacturing lightweight structures with high strength to weight ratio. Because of their immense ability of energy absorption (Gibson 1988, Wang 2009), these materials are widely utilized starting from furniture (Chen 2012) to construction elements, e.g., gypsum wallboards (Wittbold 2011) or aircraft parts (Hanssen 2006). Typically, a laminate composite is fabricated by sandwiching a lightweight softer core material between two sheets of thin but stiff skin. The core material can vary from foam structures (e.g., metal, ceramic foam, etc.) to honeycomb structures. In metal foam-based laminate composites different metal foams are used, such as steel, aluminum, nickel, titanium, and copper foams, etc. (Liu 2017). These metallic foam structures are extremely important as structural elements which withstand blast loading (Radford 2006, Hou 2010). To improve the impact resistance of metal foam core layers in such sandwich panels, the most beneficial strategy is to improve the skin properties. This is achieved in fiber metal laminates (FML) (Villanueva 2004).

In addition to the high-speed impact applications, laminate composites serve under static loading, which can arise in a wide range of applications from load bearing to nail piercing and handling (racking and stacking failure) (Gibson 1988, Bouterfa 2017, Bouterfa 2016). It should be emphasized that the skin materials used in laminate composites (sandwich panels) are different in their elastic properties from the core materials. The mechanical properties of the skin material in the out-of-plane direction are of the utmost importance, albeit scarcely studied, as to our knowledge. There is no experimental methods of evaluation of the potential effect of

the skin alone, without building the sandwich panel. The existing methodology relies on testing the performance of the entire sandwich panel, which significantly slows innovation. In this work, an alternative strategy is proposed, which elucidates the out-of-plane mechanical behavior of the skin alone and its potential effect on the underlying core in the case of punching. In additional to the mechanical and physical insights, the present results could potentially expedite the innovation cycle in the sandwich panel industry. In the present work, paper is explored as an example of the skin material. Papers of different basis weight, thickeness, and the number of plies is available. They are manufactured using different forming technology with different chemical constituents being involved. The reason for choosing paper as an example of the skin material in the present work stems from the fact that paper is already used in various sandwich structures, e.g., in gypsum wallboard, structural elements, etc. During paper manufacturing process different binding materials are added to the pulp suspension to increase bonding between filaments (Leech 1953, Ibrahim 2003, Hirn 2015). The mechanical properties of paper and their modification play an important role in multiple applications of such laminate materials. In most of these sandwich structures, paper skin is very thin (~0.05") compared to the overall thickness, and the filaments are primarily oriented in the paper (which constitutes a highly anistropic material). In many cases, multiple layers are sometimes combined to form thicker papers and paper boards (Xia 2002). Overall, paper possesses different mechanical properties in the machine direction (MD), cross direction (CD) and the out-of-plane direction (ZD). Measuring paper properties in the MD and CD directions is well developed and frequently used to characterize paper (Havlínová 2009, Uddin 2014, Medhekar 2010, Rudra 2013). However, in multiple applications such as creasing, folding or cutting the out-of-plane properties of paper are important (Stenberg 2002). Several tests, such as burst, tear or stretching have been developed and standardized to quantify the performance of different papers (Koubaa 1995, ASTM D828, ASTM D689, TAPPI 403), albeit none of them

quantifies paper characteristics in the out-of-pane direction. Several attempts have been made to develop models of paper behavior in the out-of-plane direction (Xia 2002, Stenberg 2003, Mann 1979, Harrysson 2008, Van 1973, Cox 1952, Waterhouse 1991). However, none of these works attempted to explore the protective effect of paper on the underlying core in laminated materials, which is in focus in the present work.

3. RESEARCH OUTLINE

3.1 Blood rheology in uniaxial elongation

(This section has been previously published in Kolbasov A., Comiskey P., Sahu R., Sinha-Ray S., Yarin A., Sikarwar B., Kim S,. Jubery T,. Attinger D. (2016) Blood rheology in shear and uniaxial elongation. Rheologica Acta, 55(11-12), 901-908)

Despite being at the same time a very common and precious fluid, the rheological properties of blood have not been thoroughly investigated. In this manuscript, the rheology of swine blood is characterized. The rheology study is performed in shear flow and in uniaxial elongation. Measurements show that blood is a shear-thinning and viscoelastic fluid. The relaxation time and elongational viscosity of blood are measured. The relaxation time is found in agreement with a recent measurement by Brust et al (2013). It is shown for the first time that the elongational viscosity can be 1000 times higher than the shear viscosity. Implications in biology and forensics are described.

3.2 Industrial-scale solution blowing of soy protein nanofibers

(This section has been previously published in Kolbasov, A., Sinha-Ray, S., Joijode, A., Hassan, M. A., Brown, D., Maze, B., Pourdeyhimi, B., and Yarin, A. L. (2016) Industrial-scale solution blowing of soy protein nanofibers. Industrial & Engineering Chemistry Research 55, 1, 323–333)

Solution blowing is one of the most industrially viable processes for mass production of nanofibers without significant change of trade practices. In this work a novel industrially scalable approach to nanofiber production by solution blowing is demonstrated using Biax die. Blends of biopolymer soy protein isolate Clarisoy 100 and poly(ethylene oxide) (M_w=600 kDa) were solution blown as aqueous solutions using a spinneret with 8 rows with 41 concentric

annular nozzles. Nanofiber mats were collected on a drum, and samples with an area of the order of 0.1-1 m^2 were formed in about 10 s. Nanofibers were relatively uniform with the diameters of about 500-600 nm. Theoretical aspects of capillary instability, dripping and fly formation in solution blowing relevant from the experimental point of view are discussed, as well as ways of their prevention are revealed.

3.3 Solution blowing ceramic solid-state electrolytes- toward mass production

Solid state electrolytes offer the great potential to reach Li batteries with both high performance and safety. Thus, how to efficiently synthesis solid state electrolytes is always an attracting topic. Here we report a new mass production approach– solution blowing and successfully synthesized the high ionic conductive solid state electrolyte– lithium lanthanum titanate (LLTO). Compared with the conventional electrospinning method, it is 15 times faster while the cost is cheaper. Composite solid polymer electrolyte was thereafter made with the mixture of synthesized LLTO nanofibers and poly(vinylidene fluoride-hexafluoropropylene), which shows high ionic conductivity of 1.9×10^{-4} S cm^{-1} with at 10 wt% nanowires adding amount. This improved conductivity was found to be increased by the additional Li ion pathways introduced by the nanowires network. The cycling performance is also promising, which shows low overpotential with extremely long 1000 cycles.

3.4 Heavy metal adsorption on solution-blown biopolymer nanofibers

(This section has been previously published in Kolbasov, A., Sinha-Ray, S., Yarin, A. L., & Pourdeyhimi, B. (2017). Heavy metal adsorption on solution-blown biopolymer nanofiber membranes. Journal of Membrane Science, 530, 250-263.)

Nanofiber membranes containing such biopolymers as lignin, oats, soy protein, sodium alginate and chitosan use in this work were formed using solution blowing. The heavy metals adsorption on these membranes from aqueous solutions was studied in equilibrium in the batch experiments, as well as under the throughflow conditions. The mechanical properties of nylon-6-based biopolymer-containing membranes important under the throughflow conditions were also evaluated using tensile tests. A novel model of metal adsorption in the throughflow experiments was also proposed here and verified by the successful comparison with the present experimental data. The results revealed attractive capabilities of these inexpensive nano-textured biopolymer adsorbents formed from waste materials using the process scalable to the industrial level. The results also elucidated the physico-chemical mechanisms of heavy metal adsorption on biopolymers.

3.5 Theoretical and experimental study of punched laminate composites protected by outer paper layer

(This section has been previously published in Kolbasov, A., Sinha-Ray, S., & Yarin, A. L. (2019). Theoretical and experimental study of punched laminate composites protected by outer paper layer. Journal of the Mechanics and Physics of Solids, 128, 117-136)

Lightweight laminate composite sandwich-like materials are one of the most used composite materials. When a laminate composite is punched normally to the surface, the outer skin layer plays a protective role, which is studied in the present work by elucidating the corresponding stress distribution in the core. First, a theoretical framework is developed to predict the stress distribution in the core corresponding to different mechanical properties of the skin. Thus, the location of the highest stress is predicted and a potential failure domain in the core of the laminate composite is established. The theory is verified by novel photoelastic

experiments developed and conducted in this work. In addition, a micromechanical model of behavior of paper filaments under compression is proposed and verified experimentally. Based on this model, a novel method of measuring Young's modulus and Poisson's ratio of compressed paper is proposed and demonstrated.

4. BLOOD RHEOLOGY IN UNIAXIAL ELONGATION

(This chapter has been previously published in Kolbasov A., Comiskey P., Sahu R., Sinha-Ray S., Yarin A., Sikarwar B., Kim S,. Jubery T,. Attinger D. (2016) Blood rheology in shear and uniaxial elongation. Rheologica Acta, 55(11-12), 901-908)

4.1 Introduction

Viscoelasticity of polymer solutions is essential for the understanding of fiber formation processes. In addition to various synthetic polymer solutions used by the industry, there exists a number of natural viscoelastic liquids such as human saliva or blood whose behavior is important in biology and forensic applications. The viscoelastic behavior plays an essential role in liquid dripping, and liquid jet breakup, which should be analyzed for a correct crime scene reconstruction. In this work, the viscoelastic behavior of blood and its relaxation time were quantified and measured. The implications of the results in several practically important situations is then described.

4.2 Materials & Methods

Uniaxial elongational flow of swine blood was measured using an in-house elongation viscometer (Tiwari et al. 2009; Yarin et al. 2014 and Sinha-Ray et al. 2011)based on self-thinning liquid threads. In addition to the simple shear test, experiments were conducted using the same three swine blood samples A, B and C.Such measurements require only a single droplet of blood. It is seen that the thinning follows the exponential law, which is indicative of blood viscoelasticity (Yarin et al. 2014). Then, the upper-convected Maxwell model (UCM) of viscoelasticity reveals the following exponential dependence of thread diameter d on time t

$$d = d_0 \exp\left(-\frac{t}{3\theta}\right), \qquad (4.1)$$

where d_0 is the initial value at t=0, and θ is the viscoelastic relaxation time. Note that UCM is one of the best models for description of strong uniaxial elongational flows, as well as is supported by the micromechanical models as shown in Yarin (1993).

The pendent drop method (Tropea et al. 2007) was used to determine the equilibrium surface tension of blood, which was found as $\gamma_{la} = 60.45\,\text{mN/m}$.

4.3 Results

Images of the blood thread thinning in time under the action of the surface tension are shown in Fig. 4.1 (sample A, fresh blood-tested on the day a pig was bled).The image analysis reveals the dependence of the thread neck radius on time, as depicted in Fig. 4.1 .It should be emphasized that the images in Fig. 4.1 reveal a practically perfect (especially in the 21-40 ms time range) top-bottom symmetry relative to the bottleneck cross-section of the blood thread during the self-thinning process. This means that gravitational drainage during the self-thinning process was negligibly small. Note also that cases where gravitational drainage would be important reveal the dependence $d = d_0 \exp(-t/2\theta)$ (Reneker et al. 2007, Yarin et al. 2014) rather than the one given by Eq. (3), $d = d_0 \exp(-t/3\theta)$, i.e.would tend to accelerate the thread thinning process.

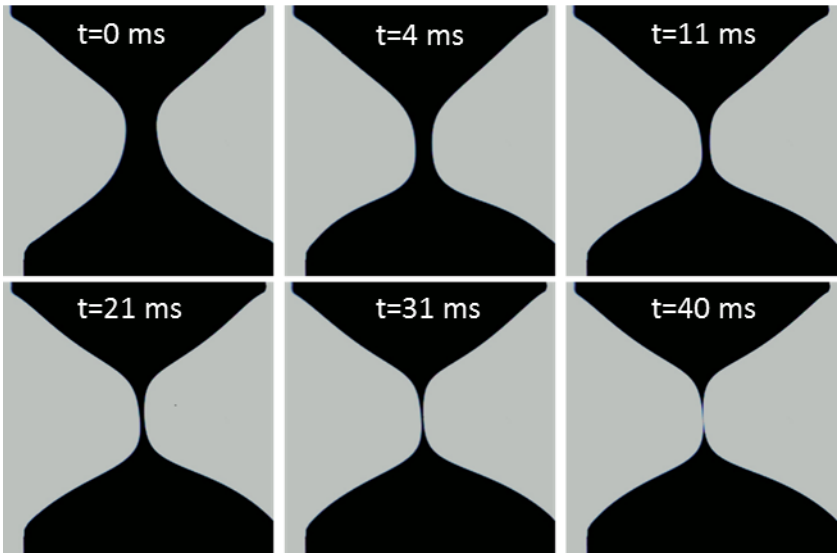

Fig. 4.1 Self-thinning thread of swine blood from sample A.

Fitting Eq. (4.1) to the experimental data, as shown in Fig. 4.2, yields the values of the relaxation time listed in Table 4.1 for blood from sample A (fresh blood, hematocrit 49%).The experimental data in Fig. 4.2 deserve an additional comment. Theconsecutive horizontal segments in the diameter-versus-timecurve in this figurestem from the discrete (digital) nature of the recorded images (cf. Fig. 4.1) and correspond to changes in the blood thread diameter within only 1 pixel of the images. This effect is obviously more pronounced when the thread thinning is slower (as for the longer time in Fig. 4.2) and/or a lower resolution camera is employed. Spatial resolution of the elongational rheometer imaging system can be increased either by using a higher resolution camera, or by increasing the optical magnification. The latter can be achieved by recording only the middle part of a thread in distinction from the entire thread in Fig. 4.1, resulting in a loss of information about the overall thread configuration, which is undesirable. Therefore, the employed variant of data acquisition and processing system are the most effective way to analyze self-thinning threads of blood with sufficient accuracy, as it was demonstrated in Tiwari et al. (2009).

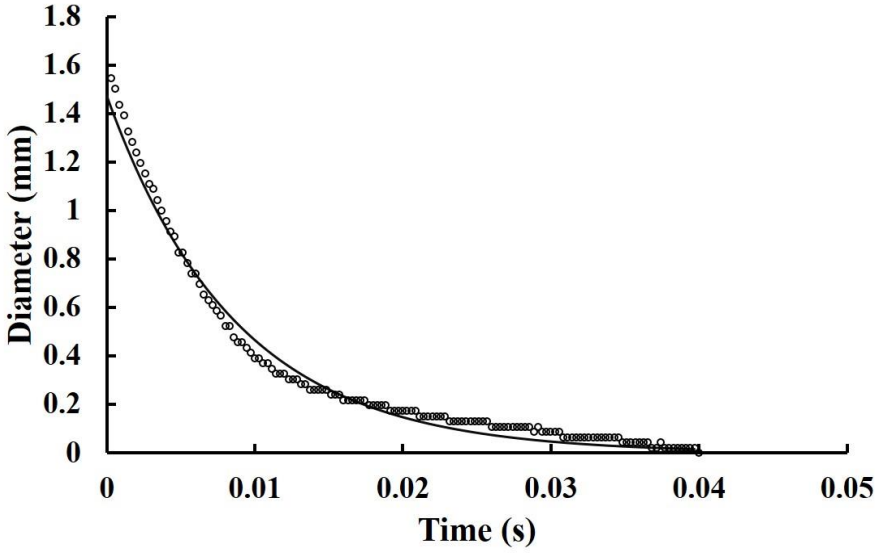

Fig. 4.2 Thread diameter as a function of time. The experimental data is shown by symbols, while Eq. (4.1) by a line.

Table 4.1 Relaxation time, elongation rate and apparent elongational viscosity at $t=t_b$ of swine blood measured in uniaxial elongational flow (sample A-fresh blood, hematocrit 49%).

Trial	**Relaxation time θ (ms)**	**Elongation rate (1/s)**	**Time at break t_b (ms)**	**Apparent elongational viscosity (Pa×s)**
1	10	66	63	21.78
2	13	51	100	45.03
3	21	32	120	37.62

Accordingly, the elongational viscosity is given as Yarin et al. (2014)

$$\mu_{el} = \frac{3\theta\gamma_{la}}{d_0}\exp\left(\frac{t}{3\theta}\right), \qquad (4.2)$$

It should be emphasized that the rate of elongation in this flow should be constant during any trial and equal to $\dot{\varepsilon} = 2/3\theta$ .Due to the trial-to-trial variation, the relaxation time θ determined by fitting Eq. (4.1) to the data (see Fig. 4.2) varies from trial to trial in the 10-21 ms range, and the elongation rate varies, accordingly, in the 32-66 s^{-1} range (cf. Table 4.1).

The values of the rate of elongation and the elongational viscosity at the time of the thread break, t_b, measured for sample A (fresh blood) are listed in Table 4.1. Note a gradual increase in the relaxation time from one trial to another in Table 4.1, which suggests that the sample may be aging, since trial 1 was preceding trial 2, which in turn, was preceding trial 3. Unfortunately, the sample-to-sample variation does not allow one to add more trials for some other blood samples to the data in Table 4.1, and explore such potential aging in more detail. Therefore, the values of the relaxation time in Table 4.1 should be considered as an order of magnitude result, which deserves comparison with an independent data.The order of magnitude of the measured relaxation time scale of the swine blood sample A matches that measured in Brust et al. (2013) for whole human blood (they reported 7.8 ± 0.6 ms).The results of the elongational experiments also showed that swine blood pre-treatment (passing through a syringe) appears to have a minor effect on the relaxation time.

As can be seen from Table 4.1, the average relaxation time of sample A (fresh blood, hematocrit 49%) is 15 ms. Fitting Eq. (4.1) to the experimental data for blood samples B and C (1-day old blood, 44% hematocrit and 40% hematocrit, respectively) revealed an average relaxation time of 2.5 ms, and 1.4 ms, respectively. It shows that lower hematocrit results in shorter relaxation time.Note also that it is known that blood begins to deteriorate with time after being drawn which implies that the aging of blood is responsible for at least a part of the

observed significant reduction in relaxation time. As we are interested in the properties of fresh blood for crime scene reconstruction, the detailed analysis for aged blood is not included.

It should be emphasized that the elongational viscosity of blood was measured for the first time, as to our knowledge.

4.4 Discussion

The comparison between the results in Table 2 and Fig. 1 show that the elongational viscositycan be significantly higher (by three orders of magnitude) than the shear viscosity. This has dramatic implications in bloodstain pattern analysis. When blood is dripping from a weapon due to the gravity-driven Rayleigh-Taylor instability, the characteristic hydrodynamic time of the dripping process is, $\tau_{dr} \approx \left(\gamma_{la} / \rho g^3\right)^{1/4}$, where ρ is the blood density and *g* is the gravitational acceleration(Chandrasekhar 1981). This time scale, $\tau_{dr} \approx 10^{-2}\,\mathrm{s}$, is comparable with the viscoelastic relaxation time of about $\theta \approx 10^{-2}$ s listed in Table 2, i.e. the Deborah number $De_{ch,dr} \approx \theta / \tau_{dr} \approx 1$. In such situations, viscoelastic effects cannot be neglected (Yarin et al. 2014), and contribute to the stabilization of the thread shown in Fig. 3a.

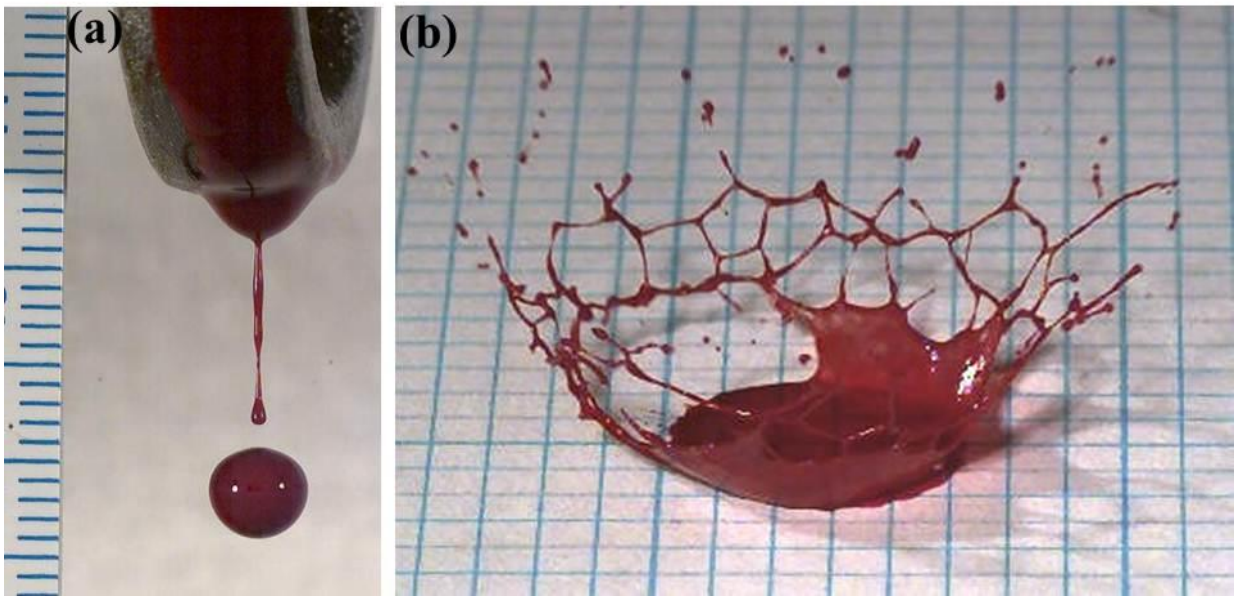

Fig. 4.3 Viscoelastic features such as formation of threads and webs of threads affect drop formation during events relevant to bloodstain pattern analysis, such as (a) a drop dripping from a weapon, and (b) the atomization of blood occurring after a drop impact onto a surface. Snapshots from high-speed visualization are reproduced with permission of the Midwest Forensic Center (Laber et al. 2008)

Viscoelasticity also plays a role in atomization processes present when the dripping drop impacts a surface, shown in Fig. 10b. For a typical impact speed and drop diameter of respectively 5m/s and 5mm, the characteristic time of the impact is 1 ms, corresponding to De=20. In situations where De>>1, the viscoelastic fluid builds up elastic stresses, practically without relaxing them. The relaxation of these elastic stresses occurs at a later time, and the existence of high elastic stresses isrevealed by the presence of a web of liquid threads in Fig. 10b.Elastic stresses indeed stabilize capillary threads against break-up instabilities, as shown in Hoyt and Taylor (1977) and Yarin (1993).

For gunshot spatters, the hydrodynamic characteristic time of the process is $\tau_{sh} \approx h / V_b$, where h~1cm is of the order of the skin and tissue thickness and V_b~300m/sis of the order of the bullet velocity. The characteristic time $\tau_{sh} \approx 10^{-4} s$ corresponds to a Deborah number $De_{sh} = \theta / \tau_{sh} \approx 100$, so that the elastic stresses built up during the bullet impact will relax during the subsequent blood flight and atomization.

4.5 Conclusion

The rheological measurements presented in this work reveal that the tensorial rheological constitutive equation of swine blood cannot be reduced to the Ostwald-de Waele power-law

model. Indeed, in uniaxial elongation the blood flow behaviour is clearly viscoelastic. The relaxation time scale and magnitude of the elongational viscosity of blood are characterized.

It is shown that the elongational viscosity can be higher than the shear viscosity by three orders of magnitude. Twosituations important in the forensic discipline of bloodstain pattern analysis, either dripping from a weapon, or splashing as a result of a drop impinging onto a surface involvethe elongational rather than the shear components of flow, as well as the characteristic times comparable or even shorter than the viscoelastic relaxation time of blood, i.e. the Deborah numbers equal or much larger than 1. As a result, the viscoelasticity of blood should be considered in the description and analysis of such processes.

It should be emphasized that the fact that blood reveals a power-law behavior in shear flows still does not mean that the tensorial Ostwald-de Waele power-law model, or any yield-stress model (e.g. the Casson model) could represent a real tensorial rheological constitutive equation of blood, since none of them is capable to account for the blood viscoelasticity demonstrated in the uniaxial elongation experiments. The uniformly valid tensorial rheological equation of blood seems to be viscoelastic with shear-thinning behavior in shear.

5. INDUSTRIAL-SCALE SOLUTION BLOWING OF SOY PROTEIN NANOFIBERS

(This chapter has been previously published in Kolbasov, A., Sinha-Ray, S., Joijode, A., Hassan, M. A., Brown, D., Maze, B., Pourdeyhimi, B., and Yarin, A. L. (2016) Industrial-scale solution blowing of soy protein nanofibers. Industrial & Engineering Chemistry Research 55, 1, 323–333)

5.1 Introduction

Nonwoven materials are used in a wide variety of applications with different requirements. Accordingly, multiple techniques have been developed for their production. While some applications can be satisfied with currently available industrial methods, others cannot. The available industrial production methods are limited by material choices and the resulting fiber morphology. As a result, low production rate methods, such as electrospinning, have to be used. This is particularly true for biomaterials. In this work a novel method of solution blowing is demonstrated to be scalable to the industrial level. This method was first scaled-up in a laboratory environment and then further at a factory. Furthermore, the nanofibers were produced from biomaterial. The morphology of such mass-produced fibers was also elucidated.

5.2 Experimental

5.2.1. Materials

For the industrial-scale solution blowing the following materials were used: poly(ethylene oxide), PEO, (M_w=200 kDa), poly(ethylene oxide) (M_w=600 kDa), and poly(vinyl alcohol), PVA, (M_w=31-50 kDa, 80% hydrolyzed), all obtained from Sigma-

Aldrich. Soy protein isolate Clarisoy 100 (CS) was obtained from ADM Specialty Food Ingredients. Distilled water was used as solvent for all the materials.

In addition, for the laboratory-scale multi-nozzle solution blowing the following materials were used: nylon-6 pellets (M_w = 35 kDa) obtained from Polysciences, formic acid (reagent grade > 95%) obtained from Sigma-Aldrich, and soy protein Pro-Fam 781 obtained from ADM Speciality Food Ingredients.

5.2.2. Solution Preparation

For the industrial-scale experiments four basic solutions were prepared first. They were: 9 wt% Clarisoy, 17 wt% PVA, 10 wt% 200 kDa PEO, and 8 wt% 600 kDa PEO aqueous solutions. The basic PVA and PEO solutions were prepared at room temperature with continuous agitation for 2 h. The Clarisoy solution was prepared at 50 °C with continuous agitation for 10 h. The other solutions were prepared by mixing these four basic solutions in different proportions. The solution agitation was performed in an open tank using a mixing blade attached to a variable-speed motor. This process causes entrapment of many air bubbles in the polymer solutions, which had to be removed. For this aim, the polymer solutions were placed on a pneumatic shaker table to facilitate faster bubble removal.

In addition, for the laboratory-scale multi-nozzle solution blowing experiments Pro-Fam 781/nylon-6 solutions were prepared by first mixing 4 g of soy protein in 35.2 g of formic acid and then leaving on a stirring plate overnight. After soy protein was completely dissolved, 4.8 g of nylon-6 was added, and then the solution was left on the stirring plate for the additional eight hours to achieve its homogeneity.

5.2.3. Setups and Experimental Procedures.

The experimental single-needle setup used in the previous works of the present group for solution blowing of monolithic and core-shell soy-protein containing nanofibrous nonwovens (Yarin et al. 2014; Sinha-Ray et al. 2011; Sinha-Ray et al. 2012; Sinha-Ray et al 2015; Khansari et al. 2012; Khansari et al. 2013; Zhang et al. 2013) is depicted in Figure 1a. In the insets in Figure 1a an in-house solution blowing die and the basic working principle of solution blowing are shown. Polymer solution is delivered from a syringe pump at a rate ~5 mL/h to a reservoir attached to the core nozzle. Air is supplied through the concentric nozzle at the pressure of 3-5 bar from a high pressure line (Figure 1a). Soy protein solution from the reservoir is issued into the surrounding high-speed air jet flow (the gas jet has velocity in the 150-200 m/s range). The gas jet accelerates and stretches the core polymer jet. The latter possesses a short (~1 mm) straight part followed by a large-scale part which undergoes not only stretching but also a substantial bending instability, i.e. flapping (Sinha-Ray et al. 2015). Stretching and bending instability result in significant thinning of the polymer solution jet, while solvent is gradually evaporating. At a certain stage, polymer precipitates, nanofibers solidify, and are collected on a solid grid-like collector, or on a wide rotating wheel.

Dies for solution blowing in setups in Figure 1 were designed to diminish propensity to clogging. That was achieved by supplying the soy protein solution jet and the surrounding gas jet co-axially. Supplying air concentrically to the central soy protein jet ensures that solvent evaporates from the polymer solution uniformly, thereby eliminating chances of an uneven drying. It should be emphasized that standard meltblowing dies do not use concentric air nozzles. As a result of utilization of such dies in solution blowing, an uneven drying would lead to ‘fly’ and ‘shot’ formation. Note also that in solution blowing process the air jet is issued from a converging nozzle resulting in a smooth convergence of air flow with the surface of the central soy protein jet and a more efficient stretching of the latter. Depending on the zero-shear

viscosity of the soy protein solution, the needle had been chosen judiciously, e.g., for a high-viscosity solution, a 13G needle had been used, while for a low-viscosity solution, a 16G needle was chosen to issue polymer jet.

Following the same principle and design criteria developed for a single-needle die, a multi-nozzle setup with 8 needles was made (Figure 5.1b). This multi-nozzle die revealed a similar level of reliability and repeatability as the single nozzle die. This intermediate scale-up provided us with the confidence for an industrial scale experiment using Biax die, which uses concentric air nozzles.

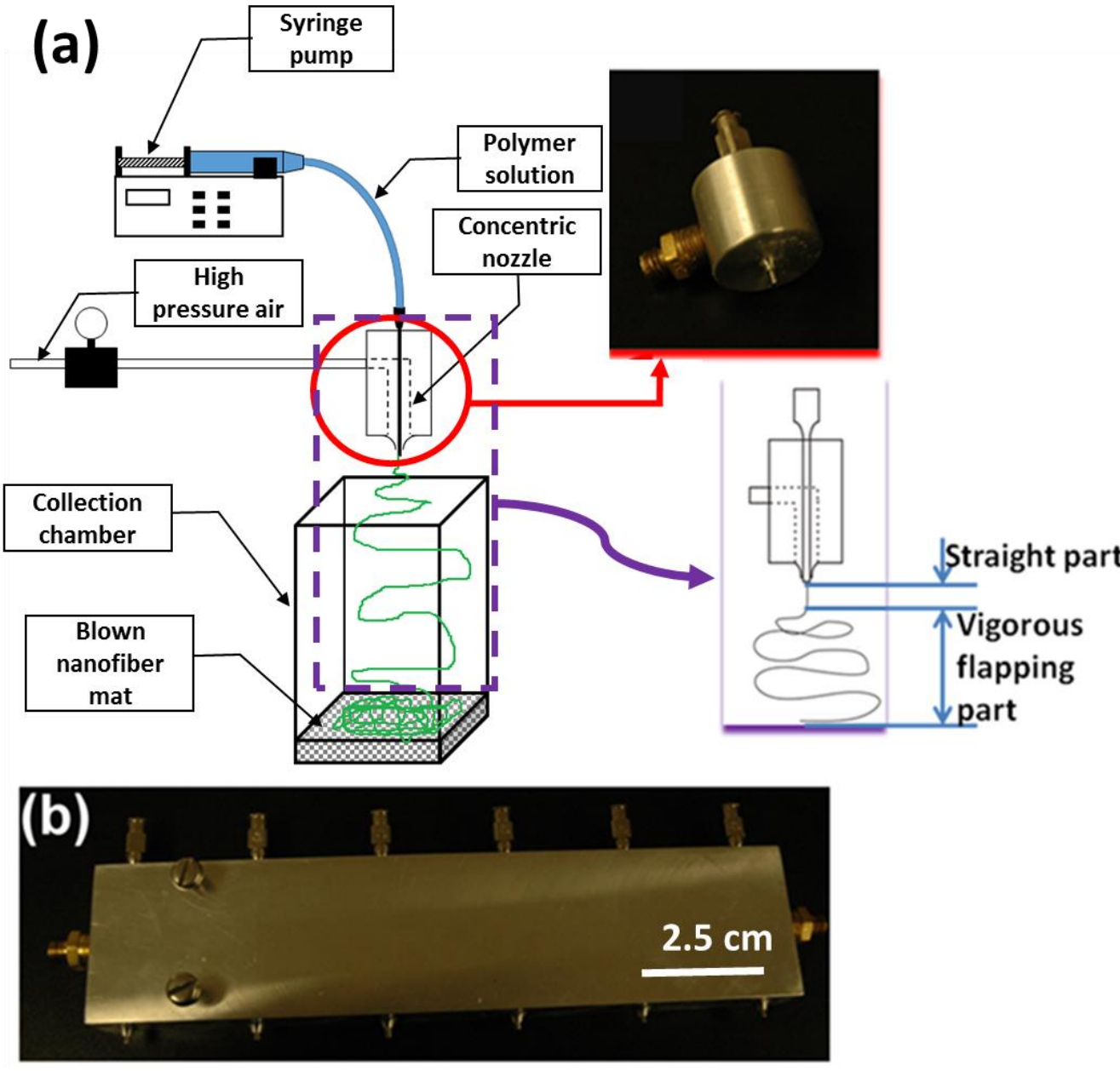

Figure 5.1. (a) Schematic of a single-needle setup for solution blowing of monolithic nanofiber mats. In the inset in panel (a), an actual single-needle die and schematic of the solution blowing process are shown (Sinha-Ray et al. 2015). (b) An actual intermediate scale multi-nozzle (single row) solution blowing die. In this die 13G (outer diameter= 0.095") needles are used.

The schematic of the experimental setup used in the industrial-scale solution blowing is shown in Figure 5.2a. Polymer solution was poured into the hopper and by gravity fed into a positive-displacement gear pump. The flow rate was controlled by adjusting the angular speed of the gear pump with 1 RPM corresponding to 10 mL/min. The pump speeds in the range 0.5-3 RPM were used in the experiment. From the pump, solution was supplied into a redistribution chamber and then to the spinneret. The spinneret consisted of an array of concentric annular nozzles with 41 nozzles per row and 8 rows (Figure 5.2b). The solution was discharged through the inner nozzles into a high temperature, high-speed air jet issued from the outer nozzles. The air temperature was controlled by the output of an electrical heater.

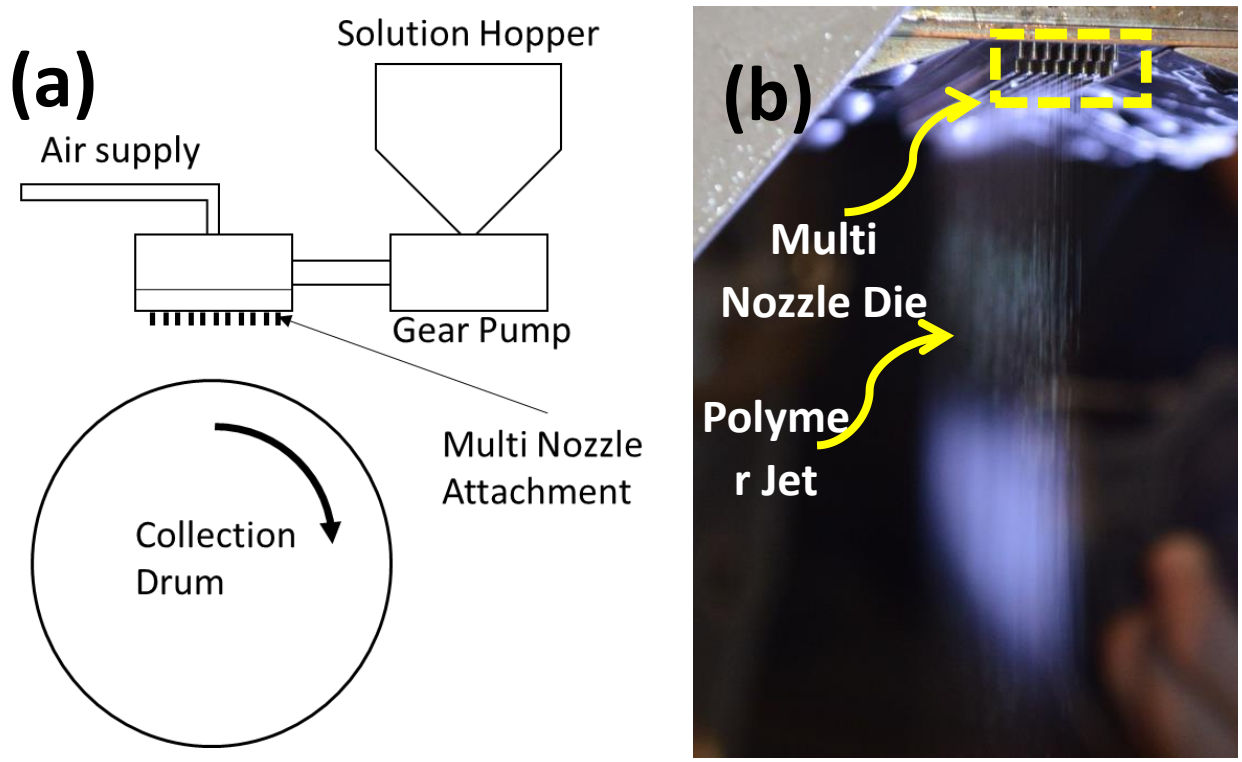

Figure 5.2. (a) Schematic of the industrial-scale solution blowing setup used in the experiments. (b) An actual multi-nozzle solution blowing process using Biax die nosepiece. It consists of 41 nozzles per row and 8 rows. The distance between the collection drum and the spinneret was about 75 cm. The oncoming air flux was not deflected back but rather spread over the drum and further down being entrained by the drum rotation. The distance between two adjacent nozzles was 3 mm. No special measures for vapor removal were taken, since only aqueous solutions were used. In the case of non-aqueous solutions the system would be facilitated by standard vapor removal equipment.

The tensile tests of solution-blown samples formed using the multi-nozzle laboratory-scale setup shown in Figure 1b were performed using a 100 N capacity Instron machine (model 5942).

5.3 Results of the laboratory-scale solution blowing experiments and tensile tests

Nanofiber mats were solution blown from 6 of the 8 nozzles of the die shown in Figure 5.1b. They were collected on a permeable plate with suction to enhance fiber retention. The resulting fiber mat shown in Figure 5.3 was collected in 5 min.

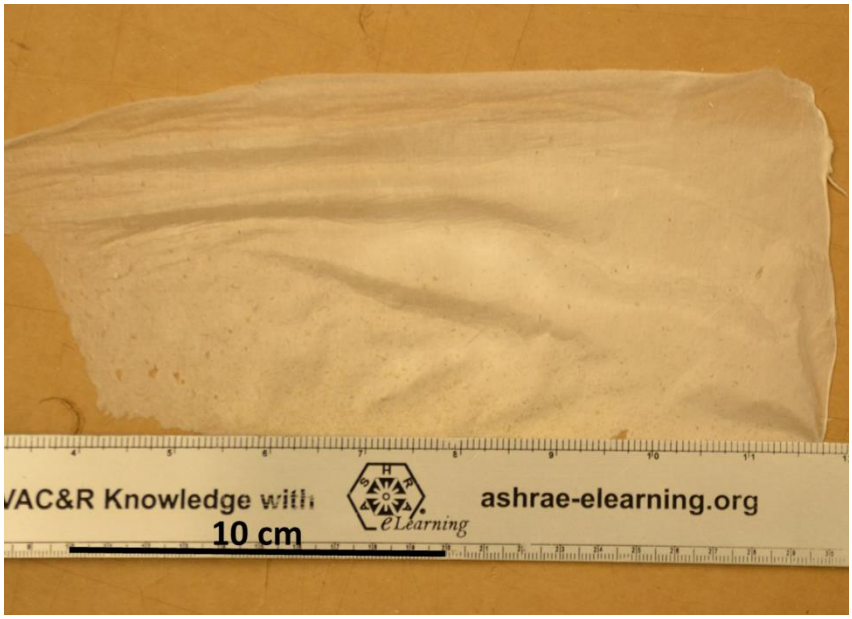

Figure 5.3. Pro-Fam 781/nylon-6 nanofiber mat with 45 wt% soy content in dry fibers. The mat was formed by solution blowing from 6 nozzles for 5 min.

To prepare samples for tensile tests, the nanofiber mat shown in Figure 5.3 had been cut into rectangular strips with 20 mm×80 mm sides. The thickness of the samples was measured using electronic calipers. The ends of the samples were clamped with the Instron pneumatic grips which were located 40 mm apart. After that, the samples were stretched at a stretching rate of 1 mm/min. The tests were conducted until sample failure past a yield point. Using the load and extension data recorded by the Instron, the true stress σ_{true} and true strain ε_{true} were calculated, with the resulting typical stress-strain curve shown in Figure 4.

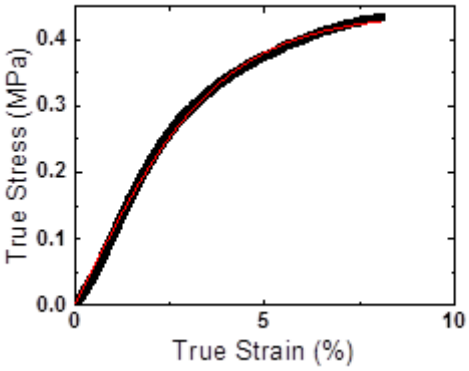

Figure 5.4. Stress-strain curve of a dry 45 wt%/55 wt% Pro-Fam 781/nylon-6 nanofiber mat measured at the stretching rate of 1 mm/min. The experimental data is shown by black symbols which merge as a thick black curve. The Green equation fitted to the data is shown by the red curve.

The elastic-plastic Green equation (Green 1956), $\sigma_{true} = Y \tanh\left(E\varepsilon_{true} / Y\right)$, was used to fit the data as shown in Figure 5.4, with E being Young's modulus and Y being the yield stress. This revealed the following values of the material parameters: $E = 9.02 \pm 3.30$ MPa and $Y = 0.83 \pm 0.46$ MPa. The value of E is lower than the value of E=31.13 MPa (with Y=0.65 MPa) reported in (Khansari et al. 2012). It should be emphasized that in the latter work only about 50% of the sample cross-section supported the load, which was accounted for. If a similar correction would be introduced in the present case, the value of the Young's modulus would be about E=18 MPa. The rest of the difference in the Young's moduli values could be attributed to the fact that in Ref.[11] the mats contained only 40 wt% of soy protein instead of 45 wt% in the present case. In addition, the volumetric porosity of the samples in (Khansari et al. 2012). could be different from that of the present sample due to a different collection method.

5.4 Results of the industrial-scale experiments and discussion

The redistribution chamber was needed to supply polymer solution uniformly to all the nozzles at the same rate. A non-uninform supply of polymer solution caused dripping or clogging due to evaporation and subsequent spraying at some nozzles (cf. Figure 5.5a). Dripping and clogging could diminish the quality of the nanofiber mat formed on the collection drum. In such cases cessation of the process and a complete cleaning of the nozzle attachment would be required, which was undesirable. A pressure transducer in the redistribution chamber was used to indicate a proper filling of the latter. Due to the low sensitivity of the transducer, backpressures below 10 psi were not registered. Two different spinnerets were used in the experiments. The inner diameters of the nozzles in the spinnerets were either 0.02” (25G) or 0.009” (32G). The nanofiber mat was collected as a nonwoven on a rotating drum.

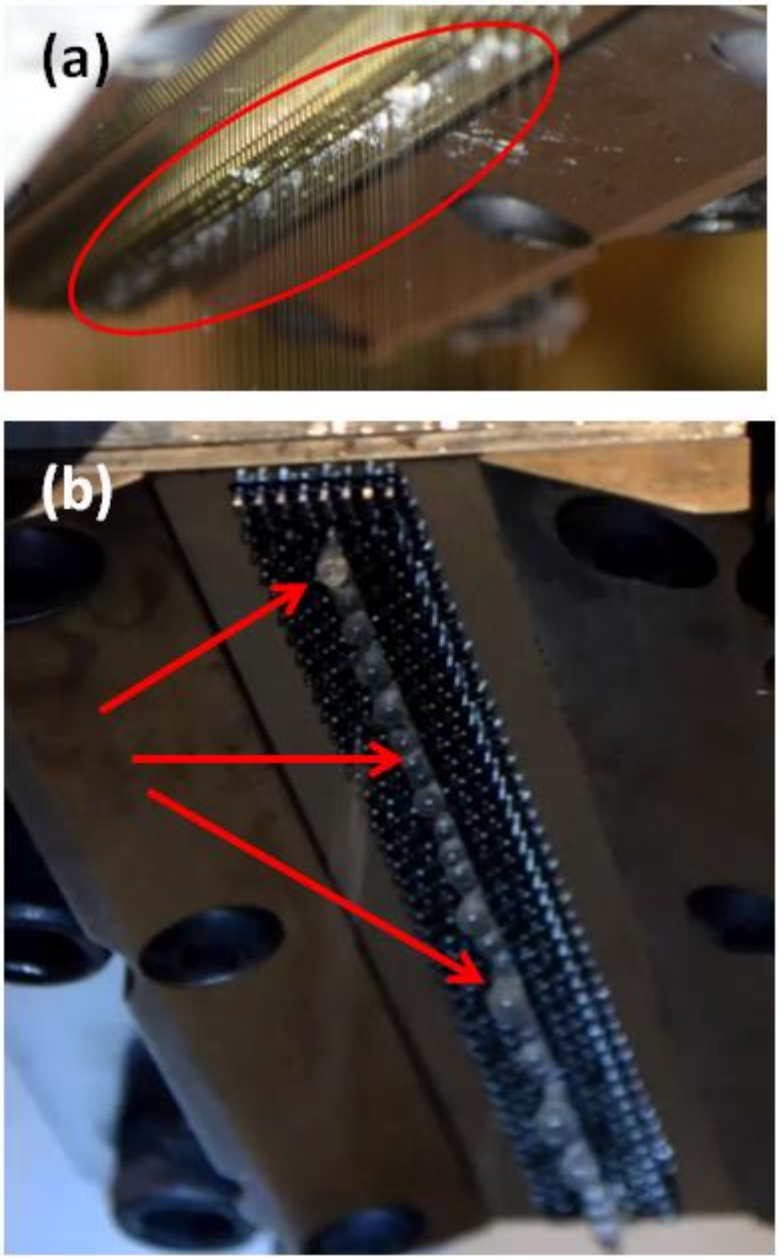

Figure 5.5. (a) Fouling, dripping and clogging of the nozzles under the improper operational conditions are shown in the highlighted zone. (b) Arrows point at the locations of drop formation at the die nosepiece when an insufficiently spinnable solution is used.

A sufficient viscoelasticity is another important criterion for continuous operation. Solutions prepared starting with the basic PVA and 200 kDa PEO solutions could not form nanofibers during the industrial-scale experiments similar to those depicted in Figure 5.2. It

should be emphasized that unlike in the laboratory-scale experiment (single needle or an intermediate-scale multi-nozzle experiment), in the industrial-scale experiment air was supplied at a higher temperature to facilitate easier solvent evaporation. As a result, the viscoelasticity (spinnability) of those solutions appeared to be too low. Because of that, the redistribution chamber was not properly filled at acceptable flow rates leading to the die clogging. As a result of low elastic forces in such cases, surface tension played a dominant role and led to drop formation at the nozzle tip due to the capillary instability (Figure 5.5b). Such drops were then detached from the nozzle by the surrounding air flow. A thin filament formed between the droplet and the nozzle (still, a manifestation of viscoelasticity) was then stretched and formed a short fiber. When dripping had happened, some fly was collected and examined under a microscope revealing significant bundling and solution drops on the laydown and beads in the fibers (Figure 5.6). The short fibers did not reach the collection drum but were dispersed by the turbulent air flow from the spinneret. Additionally, heavy dripping associated with such conditions made collection of nanofiber mats impossible. Dripping of overheated polymer solution jets is associated with the capillary instability which becomes a dominant factor when the stabilizing elastic forces are diminished (Yarin 1993; Yarin et al. 2017). Therefore, it becomes imperative to investigate the effect of the main positive factor present in the industrial-scale realization of solution blowing, namely, the strong uniaxial elongation of polymer solution jets by air flow and its effect on stabilization of the capillary instability leading to dripping. This is done in section 5.5.

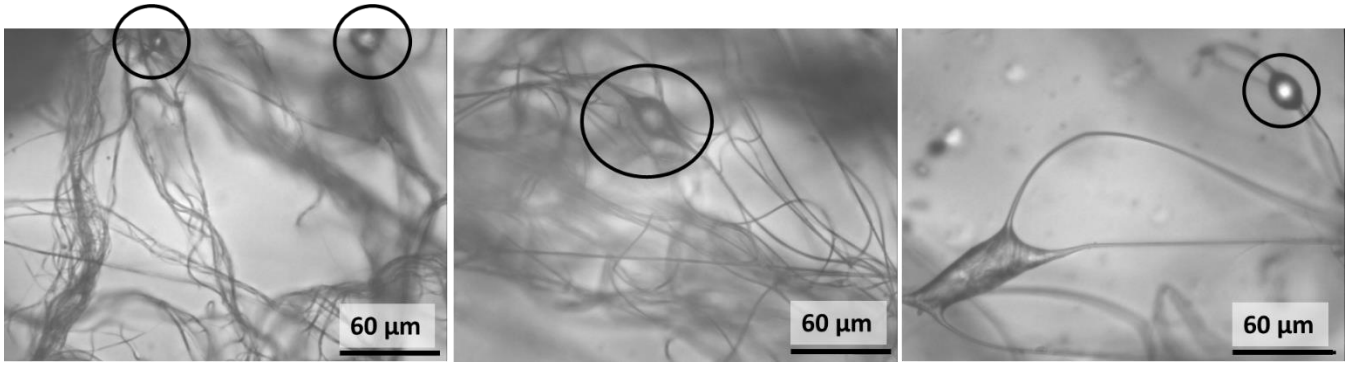

Figure 5.6. Fibers produced from solutions with insufficient elasticity were relatively short. Dripping and beading visible in the laydown resulted from the capillary instability.

A proper nanofiber production process was achieved using the 600 kDa PEO basic solution. The higher molecular weight of PEO corresponds to longer macromolecular chains of PEO, which means a higher viscoelasticity of the polymer solution. An image of such self-sustainable nanofiber solution blowing process using the industrial-scale equipment is shown in Figure 5.2b. The PEO/soy protein nanofiber mats were prepared using both 0.02" and 0.009" nozzle spinnerets with a 1:1 by volume blend of 9 wt% Clarisoy and 8 wt% 600 kDa PEO basic solutions. Figure 5.7 shows SEM images of the obtained samples. It can be clearly seen that the PEO/soy protein nanofibers blown using the larger die (0.02" nozzle) revealed multiple roping and fiber fusion as the solvent did not fully evaporate (shown by arrows in Figure 5.7a). Such roping and fiber fusion resulted in a large variation in the fibers diameters in such mats. Roping and fiber fusion was significantly reduced in nanofiber mats blown from smaller nozzles. Thus, the smaller spinneret was used to produce and collect continuous solution blown nanofiber mats. Pure 600 kDa PEO solution was also blown using a single row and subsequently a two- row spinneret.

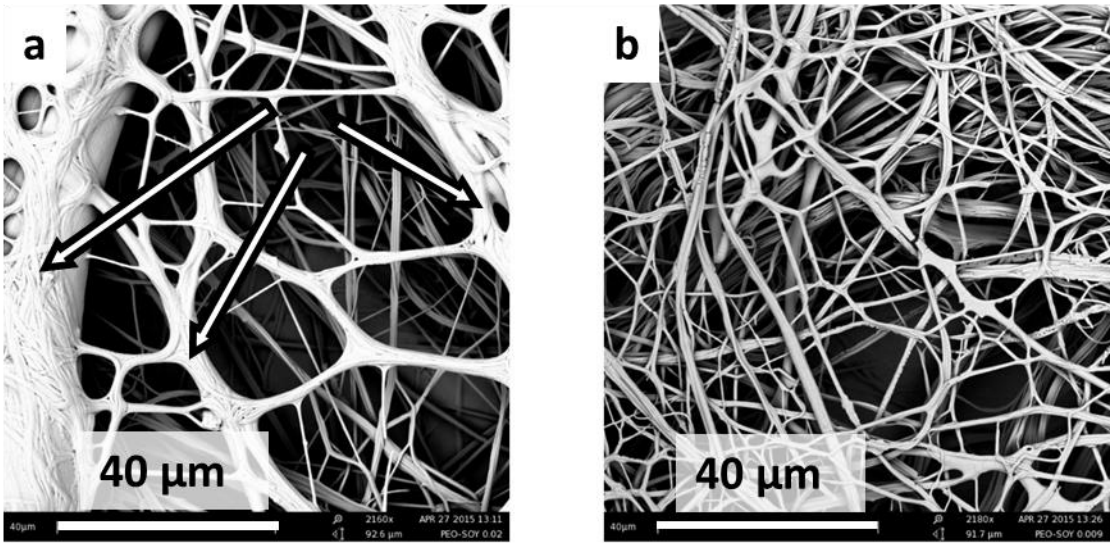

Figure 5.7. PEO/soy protein solution-blown fiber mats formed using (a) 0.02" and (b) 0.009" spinnerets.

The conditions under which nanofiber mats were blown are listed in Table 5.1. Increasing the flow rate above the tabulated values resulted in severe dripping regardless of the other control parameters. At air temperatures below 180 ^{o}F, water was not evaporating fast enough from the solution to form a fiber. A warmer air heated the die causing clogging at the nozzle exits. At air pressure below 20 psi the droplets from the adjacent nozzles merge and foul the die causing process interruptions.

Table 5.1. Process parameters for continuous fiber formation with 0.009" spinneret.

Solution	**Nozzle**	**Flow rate** mL/min/nozzle	**Solution pressure,** psi	**Air temperature ,** ^{o}F	**Air pressure,** psi
600 kDa PEO (single row)	0.009"	0.24	40	180	20
600 kDa PEO (2 rows)	0.009"	0.37	30	180	20
Soy/600 kDa PEO 1:1 by volume	0.009"	0.24	30	180	20

Macroscopic and SEM images of the collected nanofiber mats are shown in Figures 5.8-5.10, which depict samples of the order of 900-1600 cm^2 formed in about 10 s with the weight of 5.1 g. In particular, the SEM images reveal that the fiber diameters are in the 500 nm-1.5 μm range. Some pure PEO fibers blown from a single and two rows had diameter below 600 nm (13% and 9%, respectively). The mean diameter values and standard deviations for the pure PEO fibers blown from a single and two rows were 1.0 μm ± 0.53 μm and 0.94 μm ±0.42 μm, respectively. For PEO/soy protein fibers 81% of the fiber diameters were below 600 nm, while the mean diameter and standard deviation were 0.52 μm ± 0.16 μm. The corresponding fiber size distributions corresponding to mats in Figures 5.8-5.10 are shown in Figure 5.11.

Each fiber is uniform with no beads associated with capillary instability. However, some fibers seems to be ribbon-like, similarly to some previous observations with electrospun nanofiber mats (Koombhongse et al. 2001, Yarin et al. 2007).

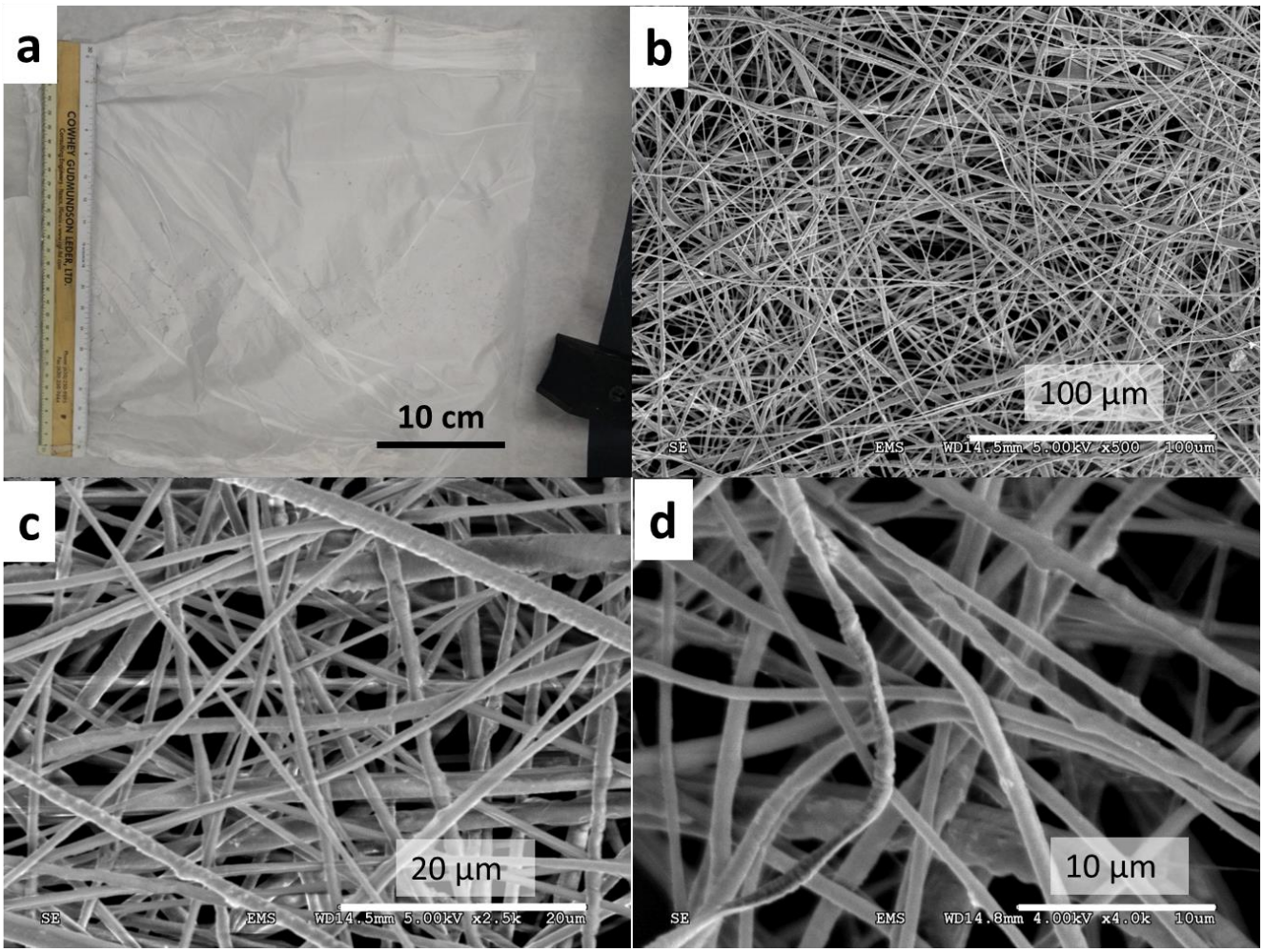

Figure 5.8. PEO nanofiber mat blown from the 600 kDa basic solution using a single row of nozzles. (a) Macroscopic view with the ruler being 30 cm, (b)-(d) SEM images at increasing magnifications.

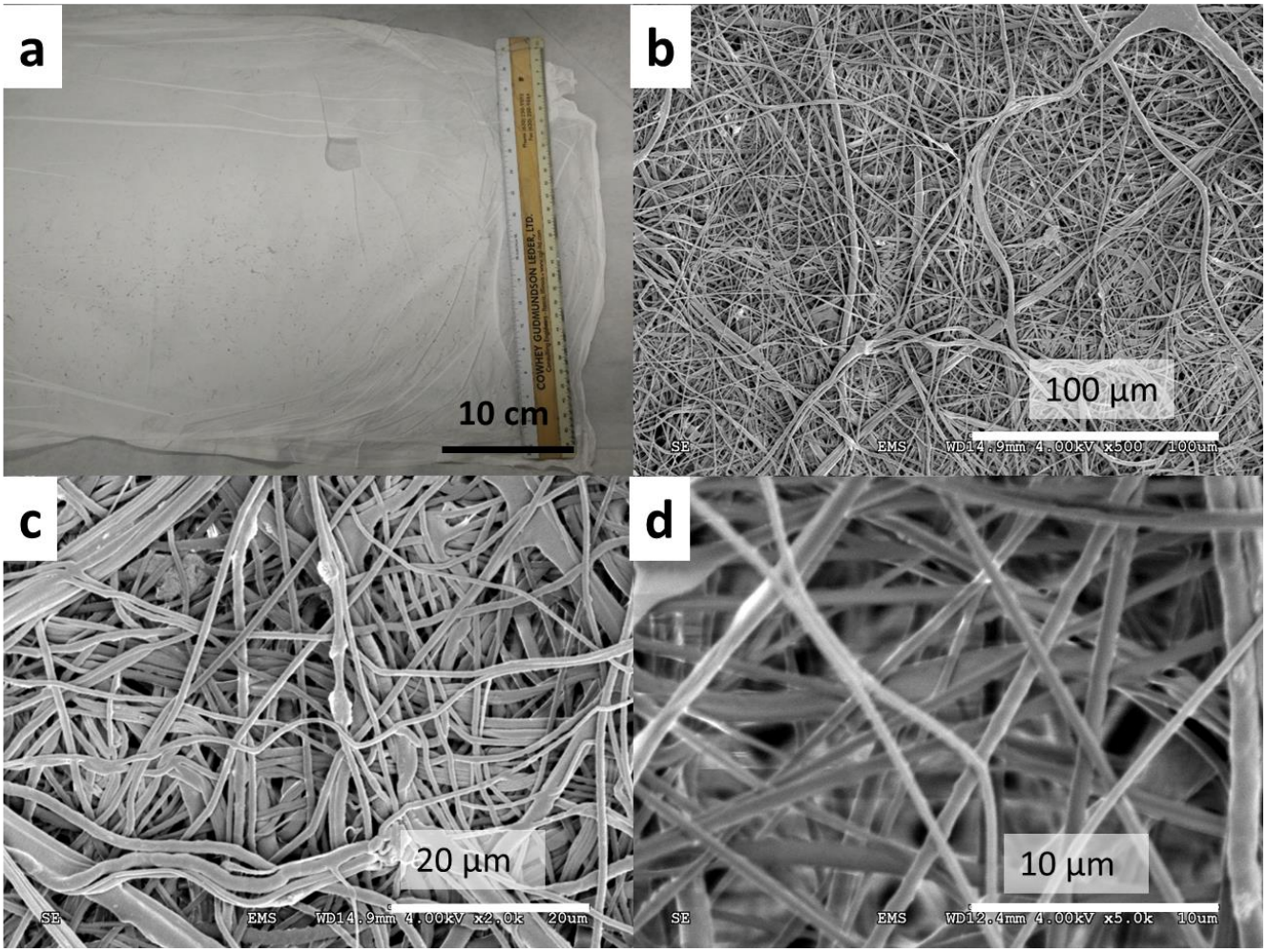

Figure 5.9. PEO nanofiber mat blown from 600 the kDa basic solution using two rows of nozzles. (a) Macroscopic view with the ruler being 30 cm, (b)-(d) SEM images at increasing magnifications.

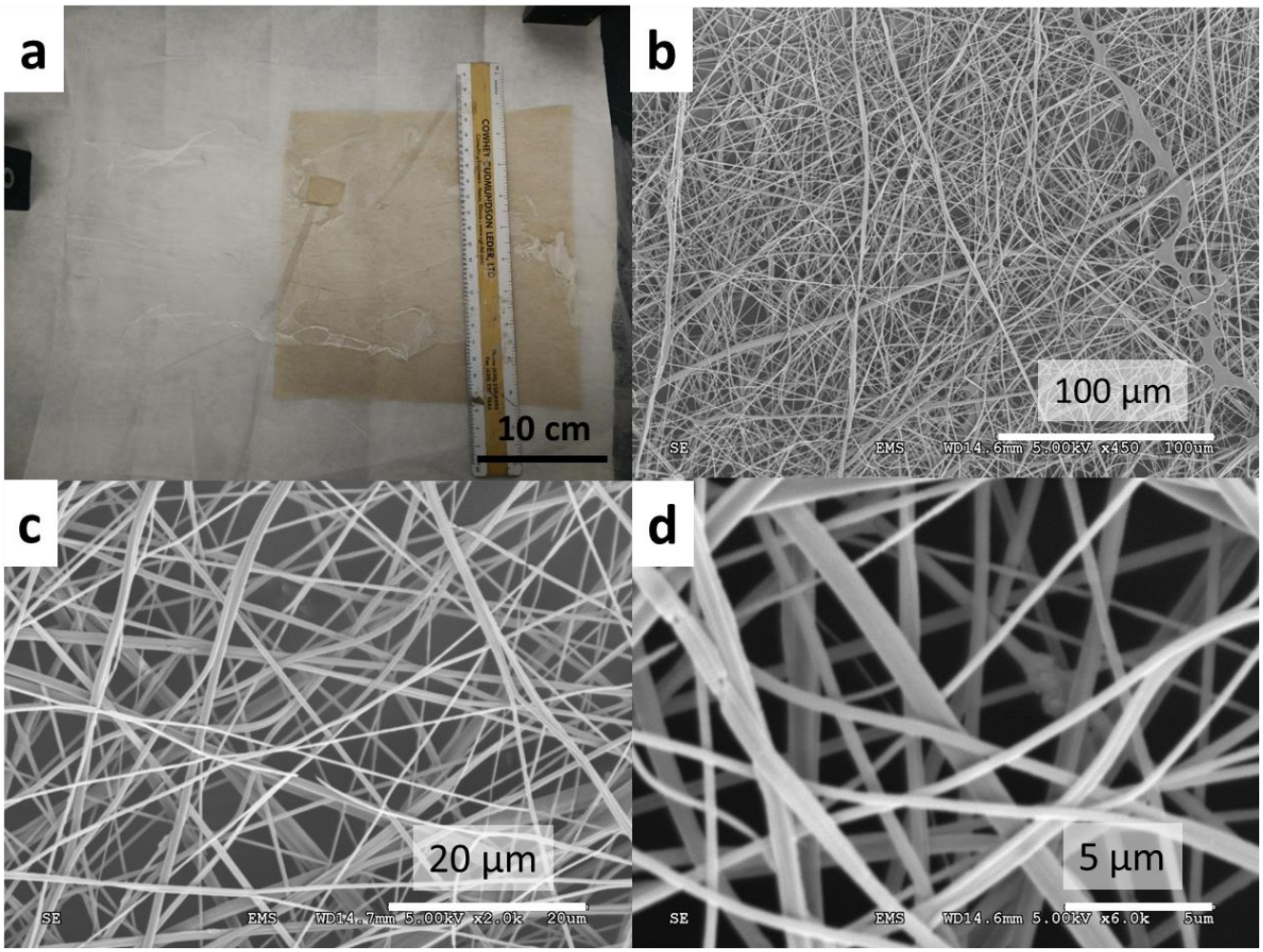

Figure 5.10. Solution blown Soy/PEO protein nanofiber mats. (a) Macroscopic view with the ruler being 30 cm, (b)-(d) SEM images at increasing magnifications.

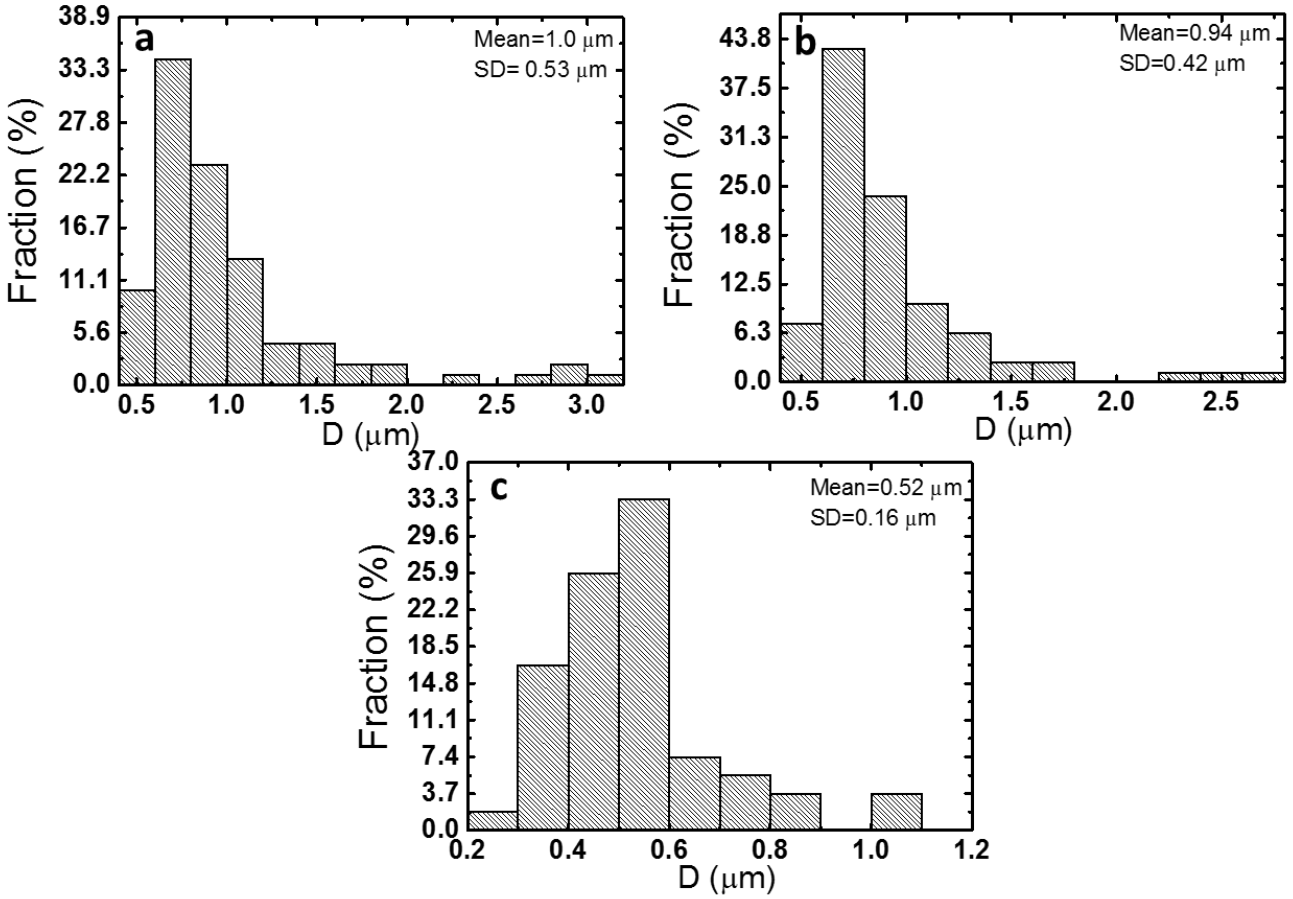

Figure 5.11. Fiber size distributions for solution blown fiber mats (a) PEO fibers blown from the spinneret with a single row of nozzles. (b) PEO fibers blown from the spinneret with two rows of nozzles. (c) PEO/soy protein fibers blown from the spinneret with a single row of nozzles.

5.5 Stabilization of capillary instability by strong stretching in solution blowing

In the case of overheated polymer solution jets, elasticity can be diminished to that extent that viscosity becomes the main rheological factor. Surface tension diminishes with temperature much slower, and thus becomes a significant detrimental factor. To address its effect, it is convenient to consider liquid jets in the framework of the quasi-one-dimensional theory of the dynamics of free liquid jets. The quasi-one-dimensional approximation for straight jets was initially introduced in the theory of capillary jet breakup and then generalized for the cases of the electrically bending jets in electrospinning (Reneker et al. 2000; Reneker et al. 2007) and for aerodynamically bending jets, for example, in solution- and meltblowing in (Sinha-Ray et al. 2010; Sinha-Ray et al. 2015; Yarin et al. 2010). For a straight jet the mass and longitudinal momentum balance under the assumption of practically plug-like velocity and stress profiles in jet cross-sections read (Yarin 1993)

$$\frac{\partial f}{\partial t}+\frac{\partial Vf}{\partial x}=0\ , \qquad f=\pi a^2 \tag{5.1}$$

$$\rho f\left(\frac{\partial V}{\partial t}+V\frac{\partial V}{\partial x}\right)=\frac{\partial \sigma_{xx} f}{\partial x}+\frac{\partial}{\partial x}\left[\frac{2\pi a\sigma}{\sqrt{1+(\partial a/\partial x)^2}}\right] \tag{5.2}$$

In Eqs. (5.1) and (5.2) t is time, x is the longitudinal coordinate reckoned along the jet axis, f the cross-sectional area (a is the cross-sectional radius), V and σ_{xx} are the longitudinal velocity and normal stress in the jet cross-section, ρ is liquid density, and σ is the surface tension coefficient. For viscous practically Newtonian liquids, which would be a reasonable for polymer solutions at elevated temperatures, the stress is given by the following expression

$$\sigma_{xx}=3\mu\frac{\partial V}{\partial x}-\sigma\left\{\frac{1}{a\sqrt{1+(\partial a/\partial x)^2}}-\frac{\partial^2 a/\partial x^2}{\left[1+(\partial a/\partial x)^2\right]^{3/2}}\right\} \tag{5.3}$$

where μ is liquid viscosity.

This expression implies that the jet surface is subjected to tractions negligible compared to the internal viscous stresses, and the deformation of the jet element corresponds in the first approximation to the uniaxial elongation/compression. The viscous term on the right hand side in Eq. (5.3) thus naturally involves the Trouton elongational viscosity 3μ; the second term corresponds to the capillary pressure proportional to the local double mean curvature of the jet surface. Equations (5.1) – (5.3) represent a slightly modified version of the equations used in (Lee 1974; Kase and Matsuo 1965; Matovich and Pearson 1969). The modification introduced in (Yarin 1993) and references therein involves the exact (not the asymptotic) expressions for the capillary force at the jet surface and capillary pressure in the jet cross-section, which allows description of the capillary breakup until formation of drops. A detailed derivation of such equations based on the above-mentioned physical assumptions and the integral mass and momentum balances can be found in the (Yarin 1993). The slower the cross-sectional radius and longitudinal velocity vary along the jet, the more accurate becomes the quasi-one-dimensional description. Therefore, there is nothing astonishing in the fact that the linear theory of the temporal instability of a slightly perturbed infinite cylindrical thread based on Eqs. (5.1) – (5.3) yields the long-wave limit of the expression for the perturbation growth rate found in the classical Rayleigh-Weber theory (Yarin 1993) from the three-dimensional equations of fluid mechanics

$$\frac{\alpha\mu a_0}{\sigma} = -\frac{3}{2}\mathrm{Oh}\chi^2 + \sqrt{\frac{9}{4}\mathrm{Oh}^2\chi^4 + \frac{\mathrm{Oh}\chi^2}{2}(1-\chi^2)} \qquad (5.4)$$

where α is the perturbation growth rate, and the dimensionless perturbation wave number

$\chi = k a_0 = 2\pi a_0 / \lambda$ with k being the wave number, λ the perturbation wavelength, and a_0 the unperturbed jet cross-sectional radius. The fastest growth rate corresponds to $\chi_* = \left[2\left(1+3\sqrt{Oh/2}\right)\right]^{-1/2}$ with the Ohnesorge number $Oh = \mu^2 / (\rho\sigma a_0)$.

Note also, that the effect of solvent evaporation is neglected here in the first approximation.

Consider a cylindrical liquid column as a model of a jet in the frame of reference moving with it. The jet may undergo stretching or not. To accommodate fixed boundary conditions in the case of a jet section stretched with a constant axial velocity U at its ends, it is useful to implement the following variable transformation

$$t_1 = t \tag{5.5}$$

$$\xi = \frac{x}{\ell_0 + 2Ut} \tag{5.6}$$

where the axial coordinate x is referred to the section length which increases from its initial value of ℓ_0 linearly in time t.

Render equations (5.1)-(5.3) dimensionless using the following scales: a_0 for a, the time scale $T=\mu a_0/\sigma$-for t, ℓ_0 / T - for V, and μ/T- for σ_{xx}. Then, after the variable transformation (5.5) and (5.6), the continuity and momentum balance equations (5.1) and (5.2) reduce to the following dimensionless form

$$\frac{\partial a}{\partial t_1} = \frac{1}{1+2\overline{U}t_1}\left(-V\frac{\partial a}{\partial \xi} - \frac{a}{2}\frac{\partial V}{\partial \xi} + 2\xi\overline{U}\frac{\partial a}{\partial \xi}\right) \tag{5.7}$$

$$\frac{\partial V}{\partial t_1} = \frac{1}{1+2\bar{U}t_1}\left[-V\frac{\partial V}{\partial \xi} + 2\xi\bar{U}\frac{\partial V}{\partial \xi} + \frac{1}{Re}\left(\frac{\partial \sigma_{xx}}{\partial \xi} + 2\frac{\partial a/\partial \xi}{a}\sigma_{xx}\right)\right]$$
$$+\frac{2}{We}\frac{1}{a^2}\left[\frac{\Lambda}{\Lambda\left(1+2\bar{U}t_1\right)^2+\left(\partial a/\partial \xi\right)^2}\right]^{1/2} \qquad (5.8)$$
$$\times\left[1-\frac{a\partial^2 a/\partial \xi^2}{\Lambda\left(1+2\bar{U}t_1\right)^2+\left(\partial a/\partial \xi\right)^2}\right]\frac{\partial a}{\partial \xi}$$

The constitutive equation for the longitudinal stress in the jet (5.3) takes the following form

$$\sigma_{xx} = 3k\frac{\partial V}{\partial \xi} - \frac{Re}{We}\left[\frac{\Lambda}{\Lambda + k^2\left(\partial a/\partial \xi\right)^2}\right]^{1/2}\left[\frac{1}{a} - \frac{k^2\partial^2 a/\partial \xi^2}{\Lambda + k^2\left(\partial a/\partial \xi\right)^2}\right] \qquad (5.9)$$

with k being

$$k = \frac{1}{1+2\bar{U}t_1} \qquad (5.10)$$

Equations (5.7) and (5.8) incorporate the following dimensionless groups: the dimensionless stretching velocity,

$$\bar{U} = \frac{UT}{\ell_0} \qquad (5.11)$$

the Reynolds number,

$$Re = \frac{\rho\ell_0^2}{\mu T} \qquad (5.12)$$

the Weber number,

$$We = \frac{\rho\ell_0^2 a_0}{\sigma T^2} \qquad (5.13)$$

and the dimensionless jet section length squared

$$\Lambda = \left(\frac{\ell_0}{a_0} \right)^2 \tag{5.14}$$

It is easy to see that both the Reynolds and Weber numbers Re and We, respectively, are determined by the Ohnesorge number

$$\mathrm{Re} = \mathrm{We} = \frac{\Lambda}{\mathrm{Oh}} \tag{5.15}$$

In the case of a non-stretching jet $\overline{U}=0$, and ℓ_0 is considered as a perturbation wavelength. Then, due to the symmetry considerations, the problem can be solved for one half of the wavelength only, and the boundary conditions for Eqs. (5.7)-(5.9) are imposed at $t \geq 0$ only at ξ=-½, and 0, as

$$\xi = -\frac{1}{2}: \quad \frac{\partial a}{\partial \xi} = 0, \quad V = 0 \tag{5.16}$$

$$\xi = 0: \quad \frac{\partial a}{\partial \xi} = 0, \quad V = 0 \tag{5.17}$$

The initial conditions at t=0 read

$$a = 1 + \varepsilon \cos(2\pi\xi) \tag{5.18}$$

$$V = 0 \tag{5.19}$$

where ε is the initial relative perturbation amplitude which will be taken in the numerical simulations as ε=0.05.

It is emphasized that according to the conditions (5.16)-(5.19) the jet is considered to be periodic over a wavelength, and thus the radius a is an even function relative to the cross-sections ξ=-½, 0 and ½, while the velocity V is an odd function relative to these cross-sections.

In the case of a jet undergoing stretching, the dimensionless group $\overline{U} \neq 0$. Then, we assume that outside of the perturbed jet section $-½ \le \xi \le ½$ the jet is uniform, and thus according to the continuity equation (5.1) its radius a_{end} varies in time as described by the following dimensionless equation

$$a_{end} = \frac{1}{\left(1+2\overline{U}t\right)^{1/2}} \tag{5.20}$$

Then, the boundary condition (5.16) is replaced by the following ones

$$\xi = -\frac{1}{2}: \quad a = a_{end}(t), \quad V = -\overline{U} \tag{5.21}$$

while the boundary condition (5.17) still holds.

Also, in the case of $\overline{U} \neq 0$, the initial condition (5.18) does not change, while instead of (5.19) we pose

$$t = 0, \quad V = 2\xi\overline{U} \tag{5.22}$$

which agrees with the boundary conditions for V at ξ=-½, and ½, in particular, with the boundary condition for V in (5.21). It is emphasized that in the case of $\overline{U} \neq 0$ cross-sections ξ=-½, and ½ correspond to the physical cross-sections of the jet $x = -\ell_0/2 - Ut$ and $x = \ell_0/2 + Ut$, and U is understood as a positive constant. That is, we are dealing with jet

stretching relative to x=0 symmetrically in the positive and negative directions. The corresponding dimensionless rate of stretching $\bar{\dot{\gamma}} = \dot{\gamma} T$ is given by the following expression

$$\bar{\dot{\gamma}} = \frac{2\bar{U}}{1 + 2\bar{U}t} \tag{5.23}$$

which shows that the initial rate of stretching is equal to $2\bar{U}$.

The system of the partial differential equations (5.7) and (5.8) with Eq. (5.9) being used was semi-discretized in the ξ-direction. The resulting system of the ordinary differential equations relative to the values of the radius and velocity $a=a_i$ and $V=V_i$ corresponding to the straight lines $\xi=\xi_i$ was solved in time numerically using the Kutta-Merson method. The results of the numerical solution are discussed below.

The first set of the physical parameters chosen is: μ=0.985 Pa$\cdot$s, σ=39 mN/m and ρ=986 kg/m^3, and the second set of parameters chosen for the simulations is: μ=10 Pa$\cdot$s, σ=25 mN/m and ρ=2500 kg/m^3.

Figures 5.12 and 5.13 show the distribution of the cross-sectional jet radius over one half of the perturbation wavelength for two different values of the dimensionless stretching velocity $\bar{U}$. Figure 5.12 shows the results for the first set of the material properties chosen, whereas Figure 5.13 shows the results obtained with the second set of the material parameters. In both cases the results are given for $\bar{U} = 0$ (no axial stretching) and $\bar{U} = 100$ (a strong axial stretching). For both stretching velocities, capillary instability progresses and results in perturbation growth. It is clearly seen how $\bar{U} = 0$ (no axial stretching) the jet profile acquires the other harmonics in addition to the one introduced by the initial perturbation [cf. Eq. (5.18)] due to the non-linearity, and the droplet connected by relatively uniform threads emerges. On

the other hand, at $\bar{U} = 100$, stretching begins competing with the capillary instability and pulls liquid to the left in Figure 5.12b. As a result, a saddle-like jet profile emerges. A similar behavior pattern is predicted for the higher viscosity case, as is seen in Figure 5.13.

As $\bar{U}$ and thus the rate of stretching increases, the stabilizing effect of stretching increases dramatically and can fully suppress the capillary instability, as is seen in Figures 5.14 and 5.15. The results shown in these figures mean that any factor facilitating jet stretching, i.e. a high relative velocity of the gas and polymer jets, or jet stretching by the collecting screen, can prevent capillary instability, dripping, and fly formation. However, care should be taken in considering the relative velocity that is required to prevent capillary instability. From Figures 5.14 and 5.15 it can be seen that capillary instability can be avoided for $\bar{U}$ ~1000-10000, which translates to relative velocity of the polymer jet >>100 m/s, which in reality is impossible to attain for subsonic solution blowing (Shambaugh 1988; Yarin et al. 2011). It is worthwhile to note that such a high degree of stretching is possible in electricity-assisted supersonic solution blowing process (Sinha-Ray et al. 2013). The results show that to avoid capillary instability, dripping and "fly" formation, either solution viscoelasticity should be increased (as it was effectively done in the experiments in the previous section) or the blowing velocity should be increased to the supersonic regimes, as in (Sinha-Ray et al. 2013).

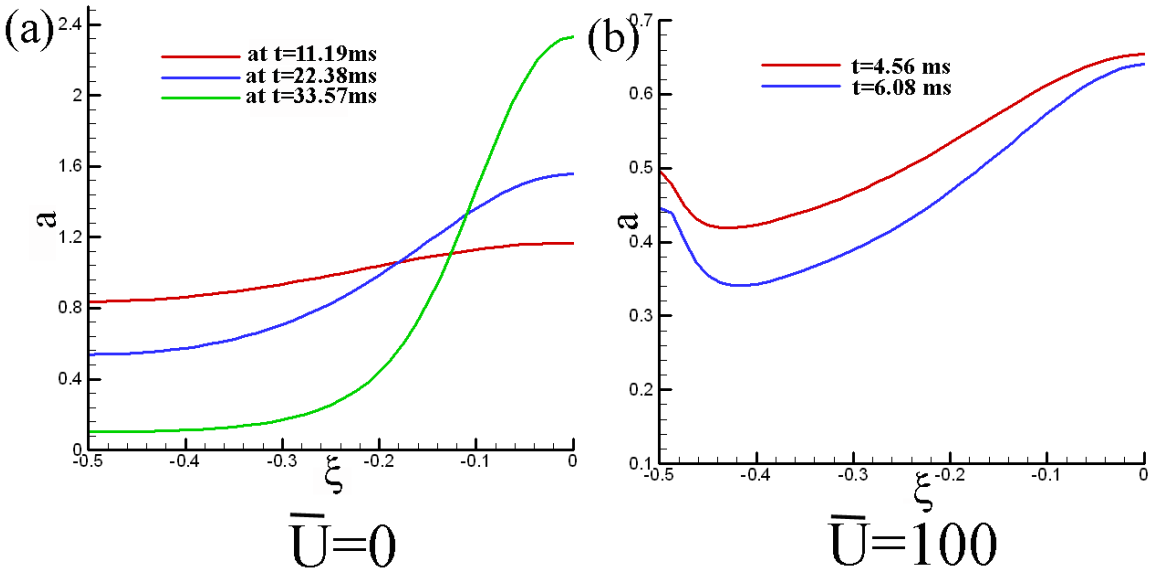

Figure 5.12. Evolution of the jet surface during the capillary breakup; one half of the wavelength of the perturbation is shown. The unperturbed cross-sectional radius a_0=60 μm, the perturbation wavelength ℓ_0=0.345 cm, the time scale T=μa_0/σ=1.52 ms, the Ohnesorge number Oh=433.709. The calculations were done with i=41 straight lines ξ=ξ_i per half-wavelength. The graph is plotted using the dimensionless a and ξ. Panel (a) $\bar{U}$=0, panel (b) $\bar{U}$=100.

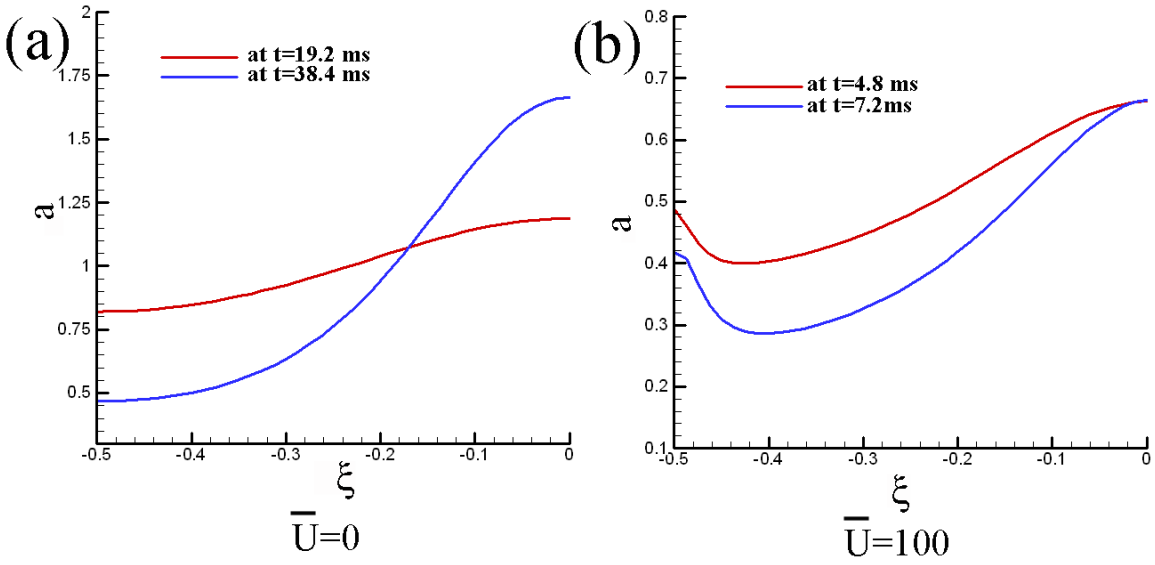

Figure 5.13. Evolution of the jet surface during the capillary breakup; one half of the wavelength of the perturbation is shown. The unperturbed cross-sectional radius a_0=60 μm, the perturbation wavelength ℓ_0=0.345 cm, the time scale T=$\mu a_0/\sigma$=2.4 ms, the Ohnesorge number Oh=2666.67. The calculations were done with i=41 straight lines $\xi=\xi_i$ per half-wavelength. The graph is plotted using the dimensionless a and ξ. Panel (a) $\bar{U}$=0, panel (b) $\bar{U}$=100.

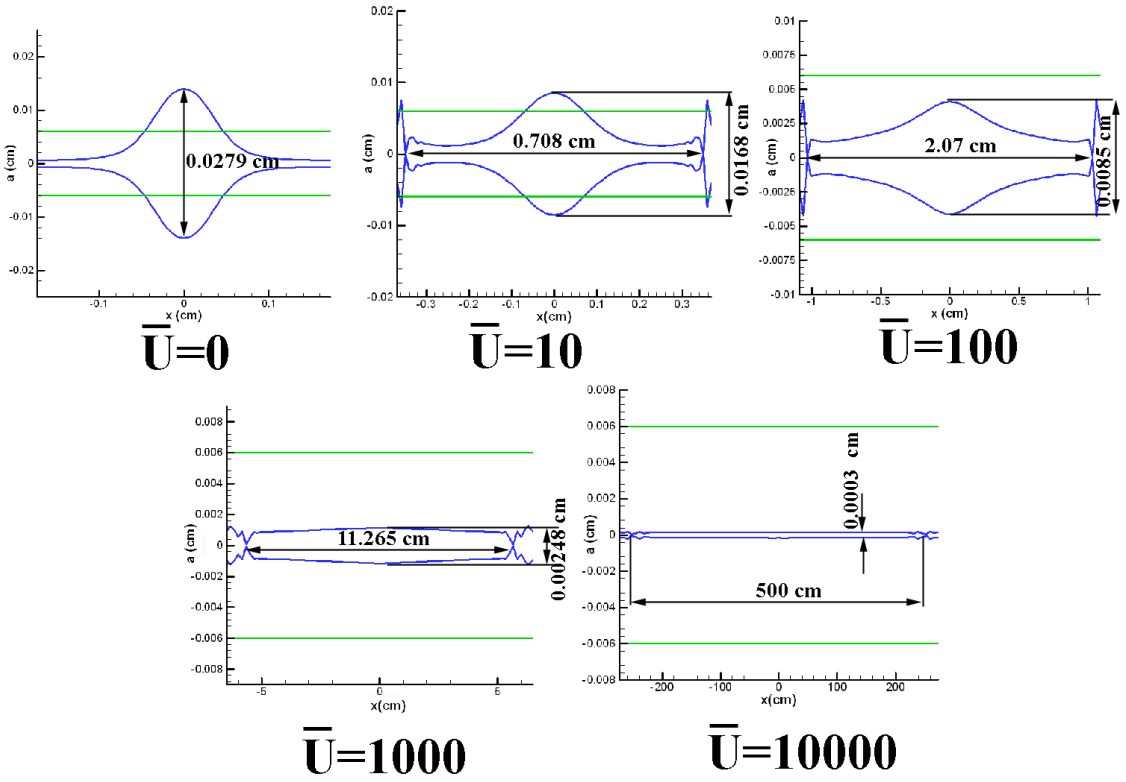

Figure 5.14. Jet shape at the beginning and at the moment of its capillary breakup for different values of $\bar{U}$ in the case of the lower effective viscosity. The green lines show the unperturbed jet, whereas the blue ones-the jet configuration at the moment when the simulation has been stopped. One wavelength of the perturbation is shown. It can be seen that as $\bar{U}$ increases, the tendency for the capillary breakup, and thus for capillary instability, dripping and fly formation, significantly diminishes and can be completely suppressed.

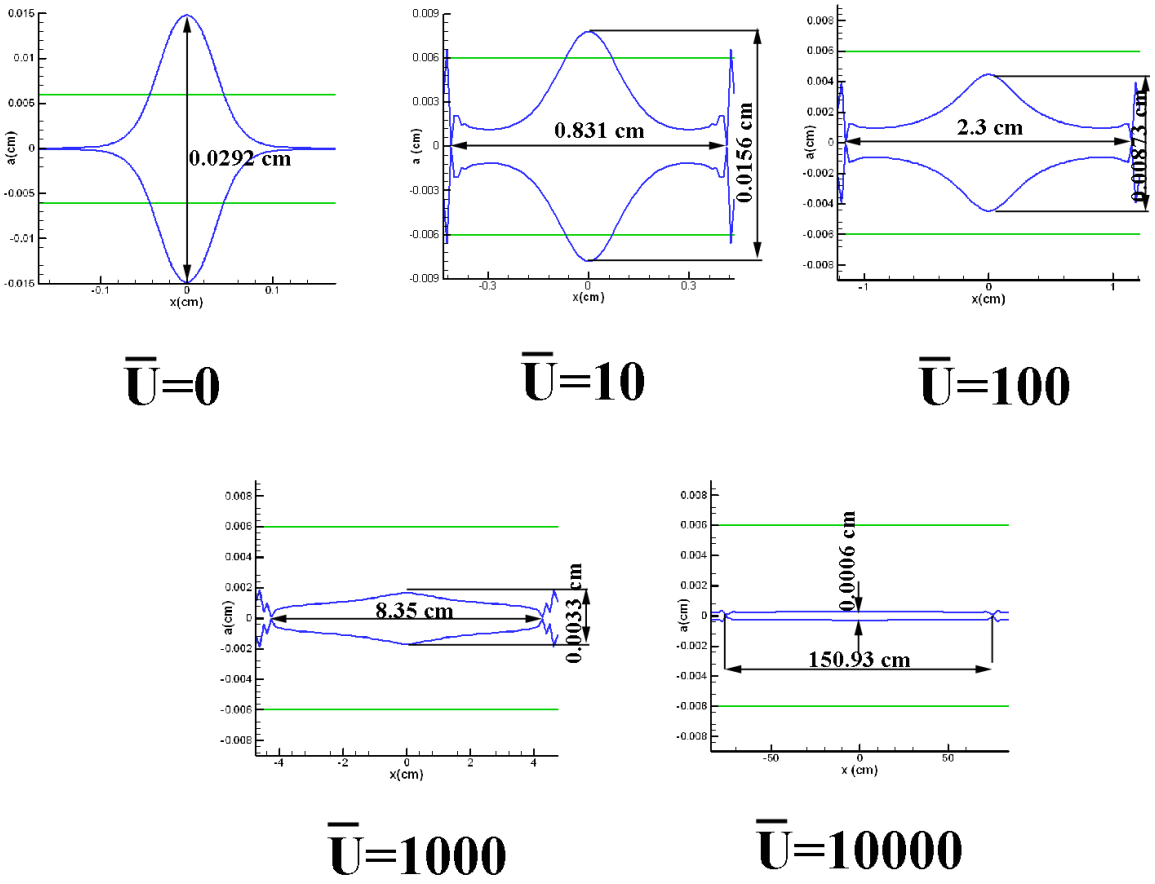

Figure 5.15. Jet shape at the beginning and at the moment of its capillary breakup for different values of $\bar{U}$ in the case of the higher effective viscosity. The green lines show the unperturbed jet, whereas the blue ones-the jet configuration at the moment when the simulation has been stopped. One wavelength of the perturbation is shown. It can be seen that as $\bar{U}$ increases the tendency to the capillary breakup, dripping and thus fly formation, significantly diminishes and can be completely suppressed. It is emphasized that the panels shown in this figure correspond to different time moments compared to those in Figure 5.14.

5.6 Conclusion

Aqueous solutions of blends of biopolymer soy protein isolate Clarisoy 100 with water-soluble petroleum-derived polymers poly(ethylene oxide), PEO, (M_w=200 kDa), poly(ethylene oxide) (M_w=600 kDa), and poly(vinyl alcohol), PVA, (M_w=31-50 kDa, 80% hydrolyzed) were blown on the industrial scale using a spinneret with 8 rows with 41 concentric annular nozzles. The solution jets were issued through the core nozzles into high-temperature high-speed air jets injected form the outer nozzles. PEO/soy protein nanofiber mats were successfully formed using a 1:1 by volume blend of 9 wt% Clarisoy solution with 8 wt% 600 kDa PEO solution. Such PEO/soy protein solutions prevented dripping, nozzle clogging and fly formation, i.e. an appropriate solution composition can overcome these problems. Blends with other polymers listed above did not allow creation of sufficiently viscoelastic spinnable solutions, which prevented formation of long fibers, rather than short and beaded ones, as well as fly. Nanofiber mats were formed from solution blown spinnable solutions on a collection drum. The cross-sectional fiber diameters were close to 500-600 nm. The fibers were relatively uniform in longitudinal direction and their diameter-distributions possessed well-defined peaks. Samples with the sizes of the area about 0.1-1 m^2 were rapidly formed. It is explained theoretically how such detrimental processes as capillary instability, dripping and fly formation in solution blowing could be prevented by higher viscoelasticity and velocity of blowing.

6. SOLUTION BLOWING CERAMIC SOLID-STATE ELECTROLYTES – TOWARDS MASS PRODUCTION

6.1 Introduction

Energy storage is an ever-present engineering problem with multiple directions of ongoing research, such as the size, capacity and safety. At the moment, the most commonly used batteries are Lithium-ion batteries which have been known to catch fire. A promising solution to this problem is the use of solid electrolytes in battery construction. However, the conductivity of such electrolytes is lower than for the liquid ones. It was found that the conductivity of solid-state electrolytes can be increased by introducing conductive nanofibers into the matrix. These nanofibers until now have been produced by electrospinning which has a very low production rate and cannot satisfy the battery production rate. In this work it was shown that a novel and industrially-scalable method of fiber making, solution blowing, can be also used to produce such fibers. The produced LLTO fibers were comparable to electrospun fibers in morphology and electrical performance. The effect of LLTO on spinnability of such polymer solutions was also elucidated.

6.2 Experimental section

6.2.1 Preparation of solution

The solutions used were a mixture of polymer solution and salt precursor solution. The polymer solution was made by dissolving 10 wt% PVP (molecular weight 1,300,000 Sigma Aldrich) in DMF. The salt solution was prepared by dissolving 0.068 g of LiNO3 (99%; Alfa Aesar), 0.8005 g $La(NO_3)_3 \cdot 6H_2O$ (99.9% Alfa Aesar) and 0.96 g Titanium isopropoxide (97% Sigma Aldrich) in DMF. Additionally, 15vol% of acetic acid was added to the salt solution to avoid hydrolysis. The polymer solution and salt solution were then mixed under magnetic stirring for 3h to form transparent and homogeneous spinning solution.

6.2.2 Preparation of composite polymer electrolyte

The composite polymer electrolyte (CPE) was then prepared first by dissolving Poly(vinylidene fluoride-co-hexafluoropropylene) (PVDF-*co*-HFP) and LiTFSI in DMF solution. Subsequently, add different amount of LLTO fibers (5wt%, 10wt% and 15wt%, respectively) into the solution to form a mixture. After stirring the mixtures at 80 ℃ for 5h, the CPE was casted on a glass plate by doctor blade and dried in vacuum at 80℃ overnight.

6.3 Results and discussion

6.3.1 Fiber formation

The LLTO-containing nanofibers for use in the solid electrolyte were fabricated by means of solution blowing, and the schematic of the setup is shown in Figure 1. In short, an 18- gage needle was inserted concentrically into a nozzle placing it in the middle of a high velocity air jet (of the order of 200 m/s). The polymer solution with salt were then fed through the needle by a syringe pump (obtained from New Era Pump System) at a rate of 6 mL/h. The solution jets were vigorously stretched and bent by the surrounding air jet. Finally, as the solvent evaporated, solid fibers were collected on a wire mesh, with suction applied to the bottom of the collector for a proper fiber retention. A small room heater (LASKO company) was used during this process to elevate the ambient air temperature and increase the evaporation rate in the fibers.

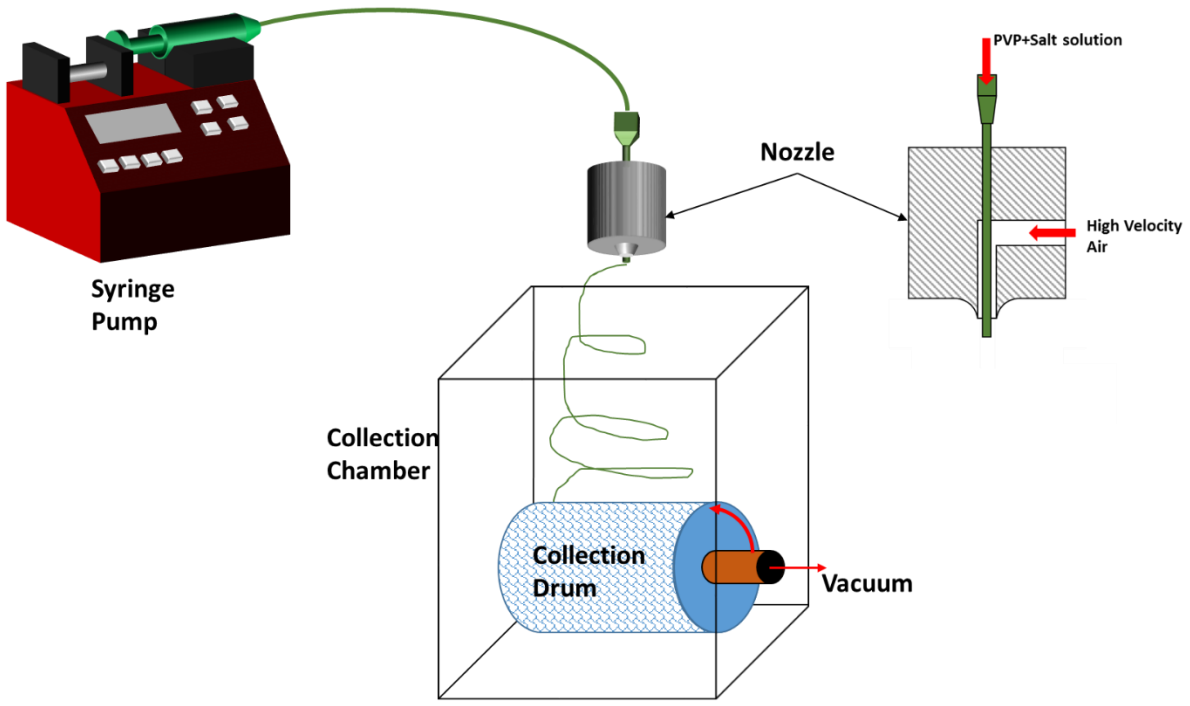

Figure 6.1. Schematic of solution-blowing setup used to form nanofibers.

6.3.2 Effect of salt on fiber viscoelasticity

Viscoelasticity of the polymer solution is the key parameter to make sure the prepared solution has a continuous spinnability. Here this parameter is characterized by the relaxation time. An in-house elongation viscometer (Yarin et al. 2014; Sinha-Ray et al. 2011) was used to measure characteristic relaxation time of the polymer solutions with and without salt. The thinning of the cross-sectional diameter at the center of polymer solution thread driven by surface tension (Figure 2) is used to elucidate the relaxation time.

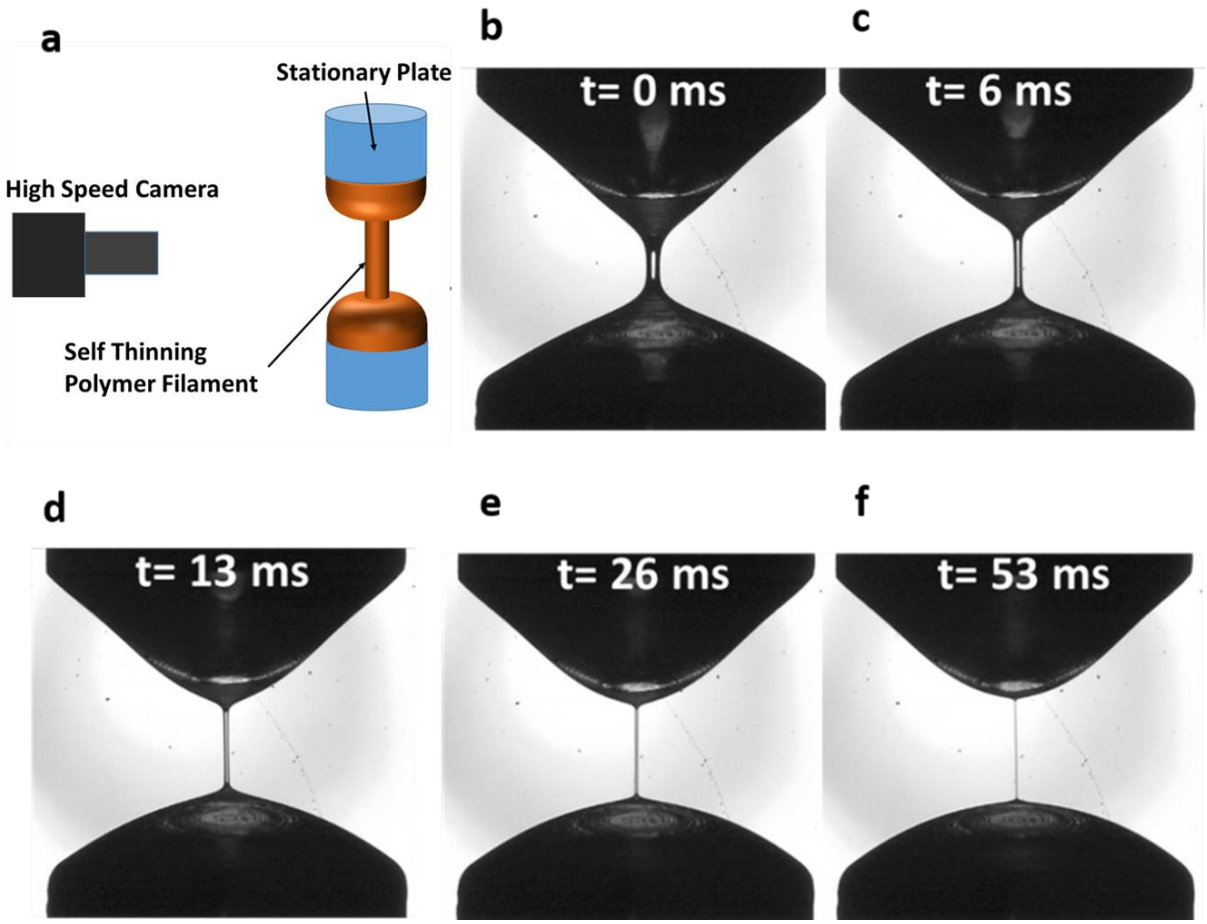

Figure 6.2. Self-thinning thread of polymer solution with salt. (a) Schematic of the elongational viscometer, (b) - (f) a series of snapshots of a self-thinning thread of polymer solution taken by the digital camera.

The relaxation time of a pure 10% PVP solution, as well as of the three different mixtures containing salt, affects the diameter d thinning in time t according to the following equation

$$d = d_0 \exp\left(-\frac{t}{3\theta}\right) \tag{6.1}$$

where d_0 is the initial value at t=0, and θ is the viscoelastic relaxation time.

The results are shown in Figure 6.3. The relaxation times for the pure PVP, 1:1, 2:1 and 4:1 PVP with salt mixtures are 3.56 ms, 3.54 ms, 2.40 ms, and 3.45 ms, respectively. This indicates

that at low concentrations, the salt does not affect the viscoelasticity of PVP solutions and does not diminish their spinnability, which is important for nanofiber forming.

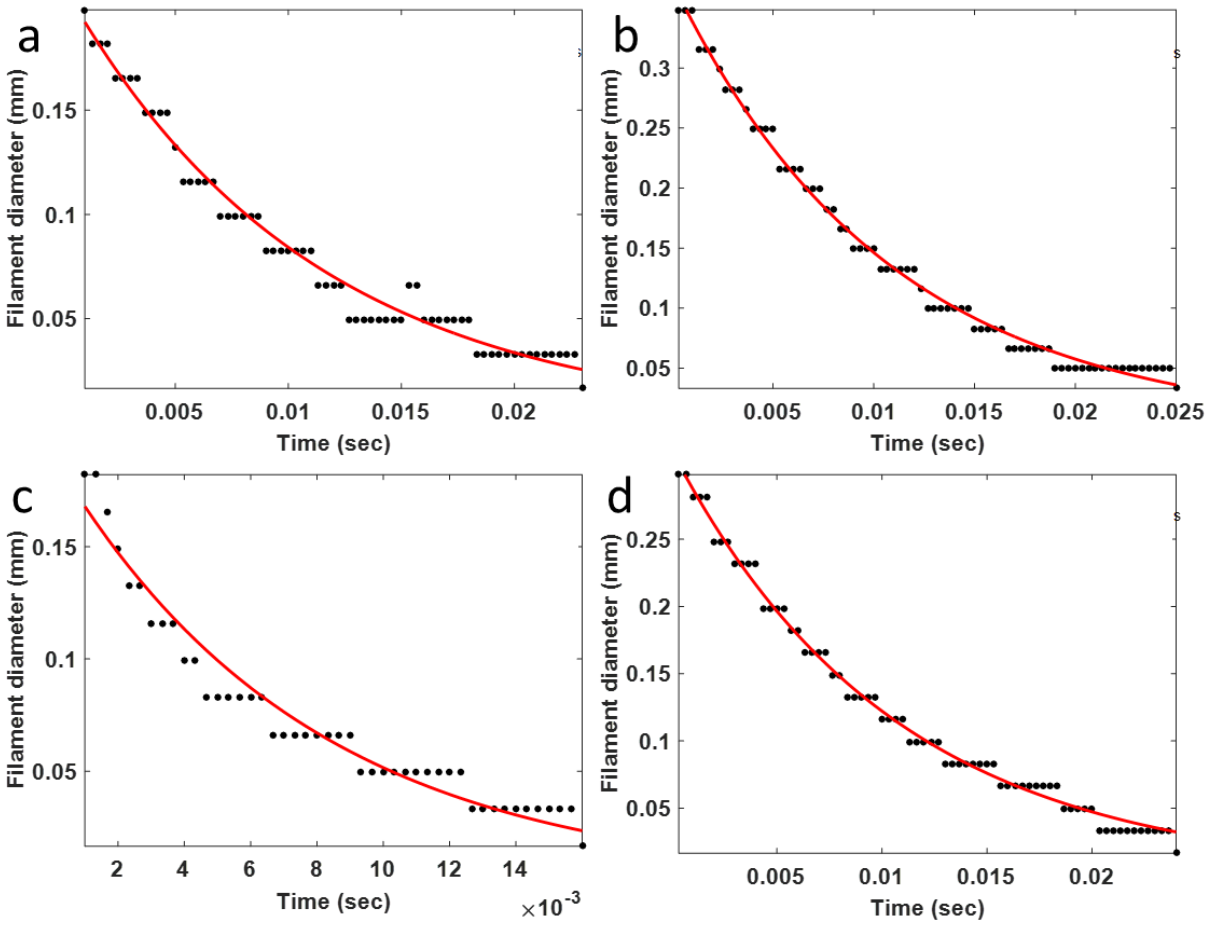

Figure 6.3. Thread diameter as a function of time for (a) 10% PVP without salt; (b) 1:1 PVP with salt; (c) 2:1 PVP with salt; (d) 4:1 PVP with salt. The experimental data is shown by symbols, while Eq. (1) by lines.

Additionally, fibers were also produced by electrospinning (schematically shows in Figure S1) to compare the production rate and quality of the fibers resulting from both methods. Electrospinning was conducted at room temperature. The collector was a rotating drum located at a distance of 15 cm from an 18-gage needle (serving as a spinneret, or a die). A syringe pump was used to supply continuously the 1:1 salt/polymer solution to the spinneret at a flow rate of

0.4 mL/h. The electric field strength between the needle and collector was sustained at 0.67 kV/cm.

The as-spun nanofiber mats with lithium, lanthanum and titanium salts were placed inside an aluminum oxide tray and calcinated using a muffle furnace to oxidize them and achieve a ceramic metal-oxide structure. The calcination temperature was set at 850 °C with the ramp rate of 10 °C /min. Calcination was performed for 2 h. During calcination, polymer degrades and disappears, while only the oxidized LLTO electrolyte in the form of ceramic nanofibers stays. Figure S2 depicts nanofiber mat before calcination and after calcination.

6.3.3 Measurements and characterization

The fiber morphology was studied by Field Emission Scanning Electron Microscopy (FE-SEM) (JEOL JSM-6320F) and ImageJ software. Figures 6.4a and 6.4b depict pure PVP nanofiber without salt added. Figure 4c shows the fiber-size distribution. Figures 6.4d and 6.4e present SEM image of PVP nanofibers with salt. Figure 6.4f shows the corresponding fiber-size distribution. Figures 6.4g and 6.4h show SEM image of these nanofibers after calcination. Figure 6.4i depicts the fiber-size distribution after calcination. It should be emphasized that the mean diameter of the calcinated fibers is essentially the same as the one before calcination. This means that salt crystals have already formed a rigid skeleton of the individual fibers before calcination, while polymer has been squeezed into gaps in-between them. Accordingly, calcination removes polymer from these gaps, which become pores, without affecting the rigid skeleton occupying the entire fiber cross-section.

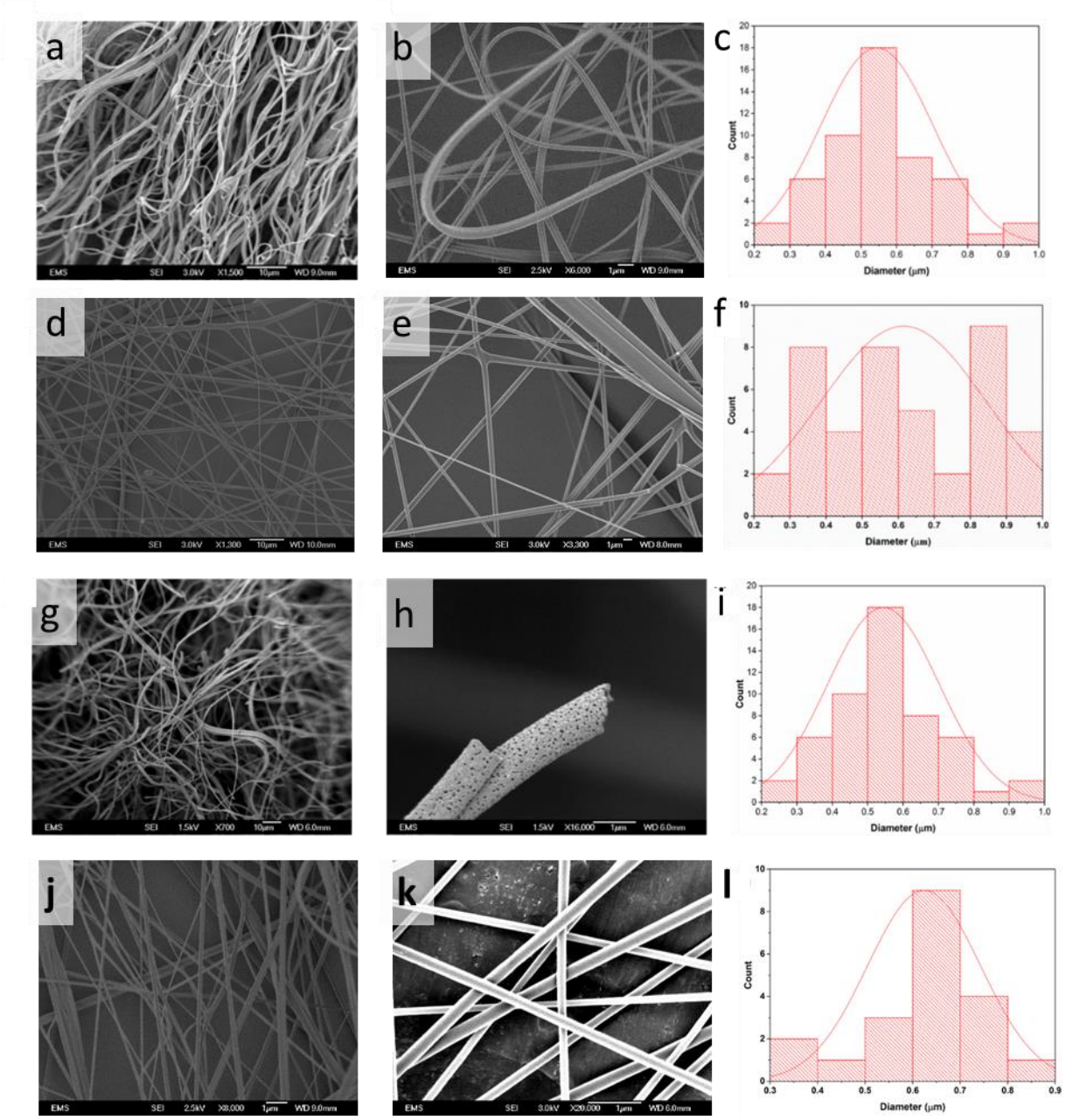

Figure 6.4. SEM image of solution-blown PVP nanofibers. (a) and (b) SEM image of 12.5 wt% PVP nanofibers formed from DMF without salt added. (c) The fiber-size distribution of the fibers from panels (a) and (b), (d) and (e) SEM images of PVP nanofibers with added salt. (f) The fiber-size distribution of the fibers from panels (d) and (e). (g) Calcinated ceramic LLTO nanofibers. (h) Two individual LLTO nanofibers with well-developed porous structure at places where polymer was removed by calcination. (i) The fiber-size distribution of the

calcinated LLTO nanofibers. (j) and (k) SEM images of electrospun PVP nanofibers with added salt. (l) The fiber-size distribution of the fibers from panels (j) and (k).

Table 6.1 lists the fiber mean diameters obtained using either solution blowing or electrospinning. The data for calcinated solution-blown fibers is also included. The mean diameter is in the 500-600 nm range. In solution blowing the flow rate was 6 mL/h, while in electrospinning only the flow rate of 0.4 mL/h f could be used, with both values being for a single needle. Accordingly, solution blowing was 15 (6 mL/h vs. 0.4 mL/h) times faster than electrospinning with the same needle.

Table 6.1. Mean diameters of solution-blown (and calcinated) and electrospun nanofibers.

Method used	**Salt/No salt**	**Mean diameter [nm]**	**Standard deviation [nm]**
Solution blowing	Without salt	544	150
Solution blowing	With salt	614	228
Solution blowing	With salt and after calcination	512	115
Electrospinning	With salt	623	118

6.4 Conclusion

In summary, solid state electrolyte – LLTO nanofibers has been successfully fabricated through solution blowing technique for the first time. This fabrication method is ultrafast and has approximately 15 times productive rate than the traditional electrospinning method at the same condition. The ceramic fibers were thereafter mixed with PVDF-co-HFP polymer to form CPE. Which shows improved thermal stability as well as high ionic conductivity and long cycle life. Those improvements were ascribing to the LLTO fiber skeleton for not only maintain the polymer structure at high temperature but also act as additional Li ion pathways. Our work opens a new direction to mass produce solid state electrolyte and gives new understanding on fiber enhanced CPE.

7. HEAVY METAL ADSORPTION ON SOLUTION-BLOWN BIOPOLYMER NANOFIBER MEMBRANES

(This chapter has been previously published in Kolbasov, A., Sinha-Ray, S., Yarin, A. L., & Pourdeyhimi, B. (2017). Heavy metal adsorption on solution-blown biopolymer nanofiber membranes. Journal of Membrane Science, 530, 250-263.)

7.1. Introduction

Availability of clean water in certain parts of the world has always been a problem and with the onset of global warming this problem will only grow. Additionally, many of essential industries release water contaminated with heavy metals as a by-product of their operation. Heavy metals are very harmful to human health. This is due to the fact that they can attach to biological materials and subsequently interfere with their function on a cellular level. There are multiple ways of removing heavy metals from water, but most have very significant costs associated with them. That is why using bio-waist for this aim is such an attractive idea. Heavy metals can be absorbed by biomaterials in the same way they will be absorbed by a living organism and require no additional processing. In this work multiple biomaterials have been spun as a nanofiber membrane by means of a novel fiber-forming process, solution blowing. The produced fibers were tested for heavy metal adsorption in a specially designed through flow setup. A theoretical estimate of the capacity of such fibers was also proposed.

7.2. Experimental section

7.2.1 Materials

For the metal adsorption experiments, 1000 ppm lead solution in 2% HNO_3 (Atomic Spectroscopy Standards) was used as a reference metal solution. It was obtained from PerkinElmer. Poly(ethylene oxide) (PEO, M_w=600 kDa), Nylon-6 (M_w=65.2 kDa), algenic acid sodium salt, poly(vinyl alcohol) (PVA, M_w=13-23 kDa) 87-89% hydrolyzed, formic acid

>95%, low sulfonate lignin alkali powder (M_w = 10 kDa), and chitosan were obtained from Sigma-Aldrich. Nylon-6 pellets, M_w = 35 kDa, were obtained from Polysciences. Soy protein Pro-Fam 781 (SP 781) was obtained from ADM Specialty Food Ingredients. Commercially available Oats were obtained from general grocery stores. All materials were used as received, without any further purification.

7.2.2. Characterization

Characterization of heavy metal adsorption was performed using an AAnalyst 200 Atomic Absorption Spectrometer (AAS) by PerkinElmer. Air-acetylene mixture was used to create flame needed to vaporize samples of metal-ion-containing solutions prepared prior, during, and at the end of the metal adsorption experiments. Metal concentrations in these samples were measured using AAS when they were subjected to the acetylene flame in the AAnalyst200 device. The device operation is based on the spectra-analytical method and it is capable to quantify the presence and amount of metals of interest. The difference between the current and the initial concentration in the sample was considered as the adsorption of heavy metal on a biopolymer nanofiber membrane used as an adsorbent.

The morphology of solution-blown nanofiber membranes was examined using Scanning Electron Microscopy (SEM), namely Hitachi S-5000 electron microscope. Prior to SEM observations, samples were sputter-coated by platinum. The thickness of the sputter-coated layer was 8 nm. Three images at different locations were always acquired for each sample. Surface porosity of nanofiber mats was measured at each location from the SEM images. After that the average sample porosity was calculated. Fiber-size distributions were also measured using SEM images. At least 100 different nanofibers from all over the three images of each sample were accounted for to find the fiber-size distribution to achieve

statistically sound results. The thickness of the nanofiber membranes was measured using an optical microscope Olympus BX-51.

7.2.3. Solution Preparation

The solution of PVA/PEO/ sodium alginate (SA) was prepared by mixing three separate solutions. The separate solutions were (i) the 7 wt.% aqueous solution of sodium alginate, (ii) the 17 wt.% aqueous solution of PVA, and (iii) the 9 wt% aqueous solution of PEO. All these solutions were prepared at 45 ºC on a stirring hotplate. Finally, these three solutions were mixed in the following proportions: 2 g of the sodium alginate solution, 3 g of the PVA solution, and 1.5 g of the PEO solution. The blend was mixed until it became homogeneous.

The soy protein/nylon-6 solutions were prepared by first mixing 1 g of SP 781 in 8.8 g of formic acid and leaving on the stirring plate overnight. After complete dissolution of soy protein, 1.2 g of nylon-6 was added. The solution was left on the stirring plate for 4 more hours until it became homogeneous.

The lignin/nylon-6 solutions were prepared by first mixing 1.5 g of lignin in 9.5 g of formic acid and leaving the blend on the stirring plate for 4 h. After lignin completely dissolved, 1.5 g of nylon-6 was added. The solution was left on the stirring plate for 6 more hours until it became homogeneous.

The oat/nylon-6 solutions were prepared by first grinding oats with a mortar and pestle into a fine powder. Then, 1 g of such powder had been mixed with 9 g of formic acid and left on the stirring plate overnight. The solution was then filtered through a coarse mash to remove undissolved oat chunks (the insoluble dietary fibers). Then, the filtered solution had been mixed with 1.2 g of nylon-6. The solution was left on the stirring plate for 6 more hours until it became homogeneous.

The chitosan/nylon-6 solutions were prepared by mixing two separate solutions. The first solution was the 14 wt.% nylon-6 solution in formic acid. The second solution was 5 wt.% solution of chitosan in 1:1 formic acid/water. These two solutions were mixed in a 2:1weight ratio and left on the stirring plate for 3 more hours until the blend became homogeneous. Fiber-forming at a higher biopolymer content was intermittent.

7.2.4. Sample Preparation

Nonwoven nanofiber mats containing such biopolymers as lignin, oats, chitosan, sodium alginate and soy protein were formed by using the solution blowing method (Sinha-Ray et al. 2010; Sinha-Ray et al. 2011; Khansari et al. 2012; Sinha-Ray 2012; Khansari et al. 2013, Yarin et al. 2014; Kolbasov et al. 2016). The setup used for this purpose is shown in Figure 7.1a. In brief, a 16G needle was inserted concentrically into an air nozzle, thus forming an annular nozzle for air flow surrounding the core polymer jet. A polymer solution was supplied by a syringe pump through the needle and subjected to a high speed air jet at the needle tip. The aerodynamic forces entrained the low-speed polymer jet, since the air-blowing velocities were of the order of 200 m/s. The polymer solution jet was stretched directly, as well as due to the aerodynamically-induced bending instability, solvent evaporated and nanofibers were deposited on the collector. The rotating drum used for the nanofiber collection was hollow with a wire-mesh surface. The interior drum was vacuumized to facilitate nanofiber adhesion to the wire mesh. Such a collector allowed us to form large and uniform nanofiber mats (cf. Figure 7.1b).

It should be emphasized that the solution-blown SA/PVA/PEO nanofiber mats had to be heat treated in an oven after solution blowing. The SA/PVA/PEO fiber mats were heated at 135 ^{o}C for 1 h. This heat treatment cross-linked PVA rendering nanofiber mats water insoluble.

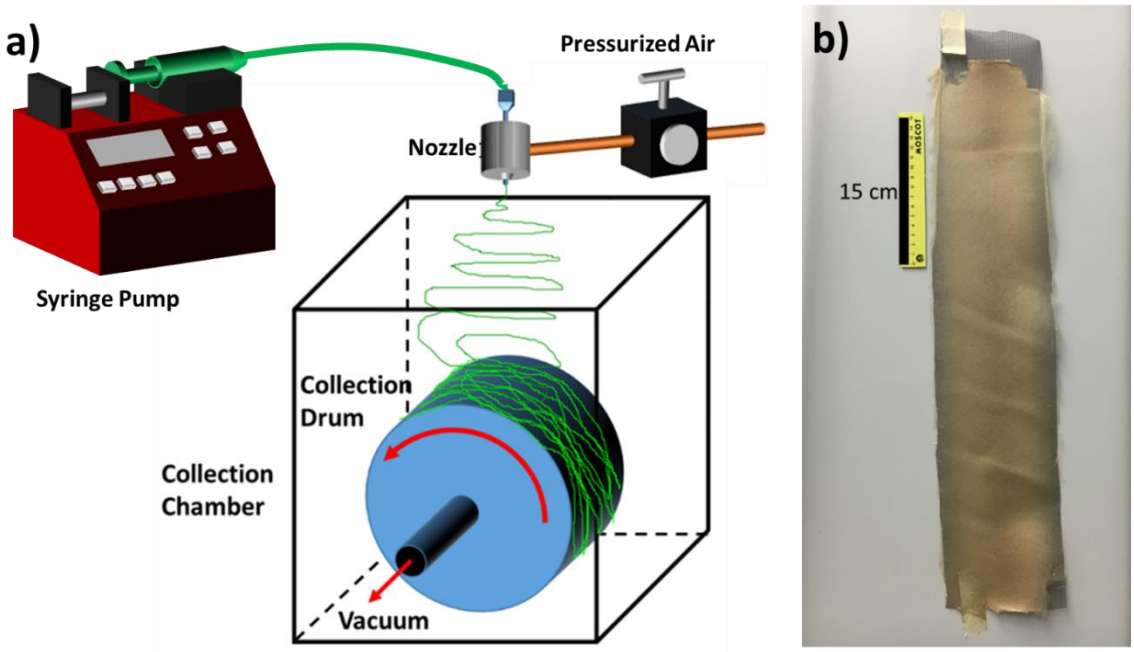

Figure 7.1. (a) Solution blowing setup used to form biopolymer/polymer nanofibers. (b) Macroscopic image of a lignin nanofiber mat sample (brown) on the wire mesh removed from the rotating drum (grey, underneath) collected for 30 min.

7.2.5. Mechanical Properties of Biopolymer-containing Nanofiber Membranes

To elucidate the mechanical properties of the produced nanofiber mats, rectangular samples 20 mm × 80 mm were cut out of the bulk nanofiber mats in both the machine and cross-machine directions. The thickness of the samples was determined optically. The ends of each sample were clamped by pneumatic grips (located 40 mm apart) of a 100 N capacity Instron machine (model 5942). The sample then underwent tensile test at a speed of 1.0 mm/min at room temperature and humidity. The stretching continued until the rupture of the samples. The results are shown in the Supplemental Information. In particular, the stress-strain diagram is shown in Figure S1 and the mechanical properties are listed in Table S1.

7.2.6. Heavy Metal Adsorption. Equilibrium adsorption isotherm

The commonly used method for characterizing the adsorption capacity of biomaterials is based on the equilibrium isotherms. The tested material is immersed in a solution of heavy metal ions of varying concentration and the resulting adsorption is plotted against the corresponding equilibrium concentration. Based on this method, numerous theoretical and empirical models have been proposed to analyze the experimental results, with the theoretically derived Langmuir isotherm being frequently used. The Langmuir isotherm is based on several assumptions: (i) the adsorption occurs only as a single layer, (ii) the adsorption takes place at specific empty active sites, (iii) the occupied sites have no further effect on the adsorption process, (iv) all the sites are equivalent. The equation expressing the Langmuir isotherm reads

$$G_{eq} = \frac{G_{max} K_L c_e}{1 + K_L c_e} \tag{7.1}$$

where c_e is the equilibrium ion concentration (mg/L), K_L is the isotherm constant (L/mg), G_{eq} is the amount of metal adsorbed at equilibrium per unit weight of the adsorbent (mg/g), and G_{max} being the monolayer adsorption capacity. Measuring G_{eq} and fitting the experimental data to eq 1 allows one to determine the value of G_{max}.

The equilibrium adsorption experiments with lignin/nylon-6 and oats/nylon-6 nanofiber mats were conducted as follows. A sample was carefully weighed. Then it was placed in a vial with 100 mL of 1, 3, 5, 7 or 9 ppm lead solution at room temperature. The sample was lightly agitated using a shaker table for 2 h, after which samples of the solution were removed and tested using AAS to determine c_e. The adsorption at equilibrium was calculated using the following equation

$$G_{eq} = \frac{V(c_0 - c_e)}{m} \tag{7.2}$$

where V is the solution volume, c_0 is the initial ion concentration, and m is the mass of the adsorbent.

The batch adsorption kinetics was addressed next. The equilibrium isotherms do not provide all the information needed for the design of a water purifier, namely the adsorption variation with time. A set of the batch adsorption experiments where the adsorbent was immersed in the solution and agitated was conducted to characterize the time dependence under such conditions. The procedure for lead adsorption on nanofiber mats containing sodium alginate or soy protein was the following. A sample of a nanofiber mat was carefully weighed, and then placed in a vial with 100 mL of 5 ppm aqueous lead solution at room temperature. The sample was lightly agitated using a magnetic stirring plate. Periodically 5 mL samples of the solution were removed at specific time intervals and tested using AAS. For sodium alginate the pH of the aqueous solution of lead was adjusted to 6.5 with NaOH. This was done because sodium alginate revealed no adsorption at low pH. For soy protein the pH of the aqueous solution of lead was adjusted to 4.5 with NaOH. Na^+ ions are not competing to get adsorbed on nanofiber materials because of the following. The adsorption of lead ions on nanofiber membranes occurs owing to such functional groups as sulfhydryl, amine, hydroxyl, carboxylic and phenolic groups. These groups do not chemically bond to sodium under the experimental conditions employed in the present work. In fact, these functional groups and Na^+ ions are ubiquitous in biological system. If Na^+ would be adsorbed on these functional groups, whole biological systems would have collapsed, and the very existence of the animal and human life would be precluded. It is a well-known fact that the existence of Na^+ ion solutions influences "salting in" (increasing solubility) or "salting out" (precipitating) amino acids' solutions containing all these functional moieties by affecting the isoelectric point (Hassan 2005), albeit Na^+ do not compete with lead adsorption on biopolymer-containing nanofiber materials. The adsorption of a nano-textured membrane subjected to the through flow of heavy metal solution was studied next. For this purpose the experimental setup shown in Figure 7.2a was used. A sample of a circular nanofiber membrane was sandwiched between two meltblown circular

polypropylene mats cut out using the same punch (Figure 7.2b). The polypropylene mats do not have any active materials and do not contribute to the adsorption possess. They, however, provide a mechanical support to the sandwiched nanofiber sample allowing it to withstand the drag imposed by the flowing solution and avoid tearing. The supported nano-textured nonwoven sample was then placed inside a filter holder and flushed with DI water for 2 min. This was done to wash off any loose chemicals from the surface of the nanofiber mat. Finally, a 5 ppm aqueous solution of lead was pumped through the membrane at the flow rate of 20 mL/min at room temperature. The pH of the lead ion solution was adjusted with NaOH. The metal-adsorption trials were conducted for 5 min with 5 mL of the aqueous solution of lead being collected downstream of the filter holder at the start of every 30 s mark point. At a specified flow rate, a 5 mL sample was collected in 15 s. Following the completion of a trial, the lead concentration of in the collected filtered samples was measured using the AAS.

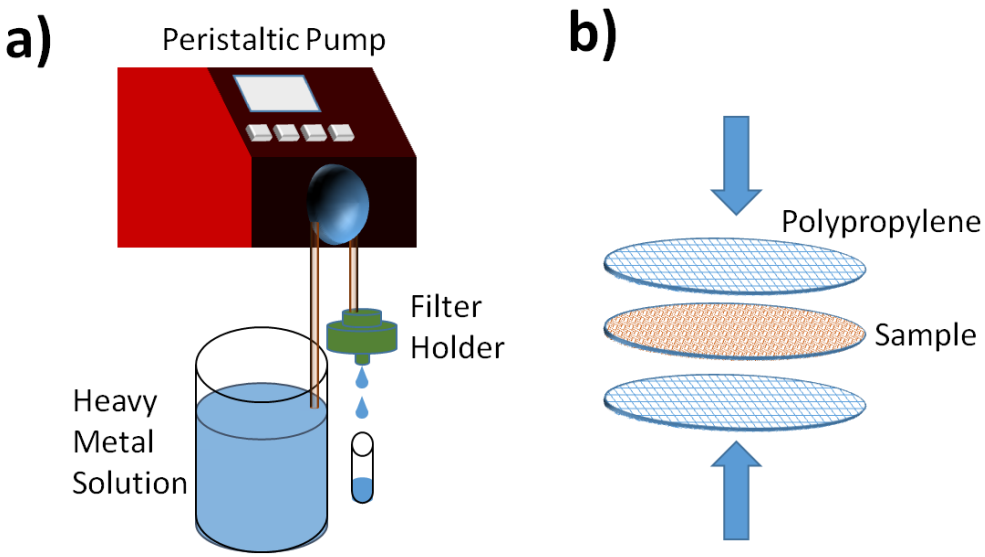

Figure 7.2. (a) Experimental setup for heavy metal adsorption experiments in throughflow. (b) Nano-textured biopolymer-containing sample inside the filter holder.

The metal adsorption per unit mass of the adsorbent as a function of time was determined as

$$G(t) = \frac{M_0}{A_0 T} \int_0^t \left[1 - \frac{c(t)}{c_0} \right] dt \qquad (7.3)$$

where M_0 is the initial mass of lead in the vial of stock solution, c(t) is the measured concentration of lead behind the filter as a function of time, A_0 is the mass of the adsorbent in the nanofiber membrane at the end of the experiment, and T is the time during which the aqueous sample was collected.

7.3. Results and discussion

The macroscopic and microscopic images of all nanofiber mats solution-blown with biomaterials are shown in Figure 7.3.

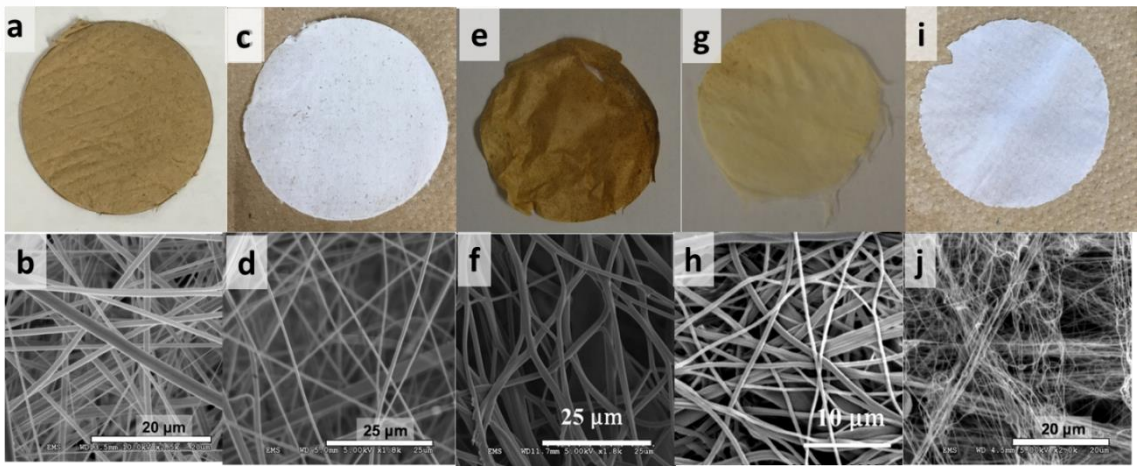

Figure 7.3. Macroscopic and microscopic images of: (a,b) lignin/nylon-6 membrane; (c,d) oats/nylon-6 membrane; (e,f) sodium alginate/PVA membrane; (g,h) soy protein/nylon-6 membrane; and (i,j) chitosan/nylon-6 membrane.

7.3.1. Mechanism of Heavy Metal Adsorption

Heavy metal adsorption is strongly dependent on the functional groups of a specific adsorbent (Vadahanambi et al. 2013; Du and He 2011; Lin and Chen; 2014; Rostamian et al. 2011; Skorika et al. 2010), in particular, on sulfhydryl, amine, hydroxyl, carboxylic and phenolic groups. In this present work all the chosen biopolymers are 'ripe' with these functional moieties. Soy proteins contain almost all the amino acids, which contain all the functional groups. Standard oatmeal contains β-glucan, which is an efficient metal adsorbent (Skorika et al. 2010) owing to its plentiful hydroxyl group. Lignin contains phenol groups, which also lend themselves as the efficient adsorbents. On the other hand, sodium alginate and chitosan are polysaccharides containing such functional groups as hydroxyl etc., rendering them to be efficient adsorbents. It can be seen that different biomaterials have different number and types of functional moieties. Accordingly, the adsorption capacities of different biomaterials are very different.

7.3.2. Stability of Nanofiber Mats in Water

Prior to the investigating the adsorption capacity of biopolymer-containing nanofibers, the effect of pure nylon-6 nanofibers was studied. The above-mentioned procedure was applied to a pure nylon-6 solution-blown nanofiber mat at pH 2.6. The measured lead concentration did not change with time. A similar experiment conducted at pH 6.1 showed a sharp drop in pH after the addition of nylon-6 nanofiber mat. This was attributed to a residual formic acid encapsulated in the nanofibers. To eliminate that factor, the nanofiber mat was left at room conditions for 2 days. The testing of the nylon-6 nanofiber mat after such waiting period revealed no change in the pH or lead concentration in the solution with time indicating that nylon-6 does not contribute to metal adsorption. Accordingly, for all the experiments nanofiber

mats were left in open air for 1-2 days to eliminate any residual solvent encapsulated in the solution-blown nanofibers.

The raw lignin powder used to form nanofiber mats is fully soluble in water and, accordingly, it was observed that some lignin is lost during the adsorption experiment. To quantify this lignin loss, the mass of the nanofiber mats containing lignin was measured before and after submerging in the aqueous solution of lead for different time intervals. The results are shown in Figure S2. It was seen that about 50% of the mass of the nanofiber mat was lost and that only the lignin remaining on the nanofiber mat surface plays a role in the adsorption kinetics.

7.3.3. Batch Adsorption Kinetics

It is important to evaluate the mass of lead adsorbed by, for example, the lignin-containing nanofibers per unit adsorbent mass in time. Let 1 g of the adsorbent adsorbs G g of lead. Then, L_0 g of the exposed adsorbent in the sample adsorb x gram of lead, and

$$\frac{1}{L_0} = \frac{G}{x} \tag{7.4}$$

Note that $x = M_{\ell 0} - M_{\ell}$ where $M_{\ell 0}$ is the initial mass of lead in water in a vial and M_{ℓ} is the current mass of lead in water in the vial. Then, from eq 7.4 one can find that

$$G(t) = \frac{M_{\ell 0}}{L_0}\left[1 - \frac{M_{\ell}(t)}{M_{\ell 0}}\right] \tag{7.5}$$

which ascertains the dependence on time t. In the experiments $M_{\ell}(t)$ is measured, thus G(t) is found from eq 7.5.

In the batch adsorption experiments lead concentration in a vial was measured by AAS as a function of time using small samples withdrawn from the vial (cf. Figure 7.4a). Since the

overall volume of water in the vial is known, this measurement reveals the values of $M_\ell(t)$. These values were recast in the values of G(t) presented in Figure 7.4b.

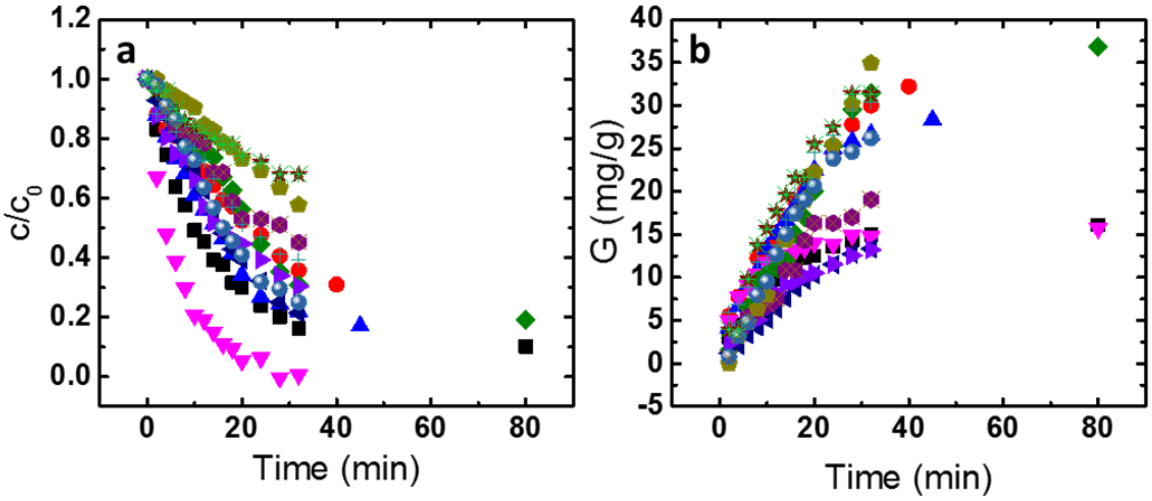

Figure 7.4. (a) Lead concentration c as a function of time. (b) The adsorption per unit weight of the adsorbent (lignin in the lignin-containing nanofibers) as a function of time. Different symbols correspond to 14 different nanofiber mat samples. Porosity of these samples was unknown. Here and hereinafter the results corresponding to different samples are shown by different colors.

Figure 4b reveals an interesting fact that lead adsorption per unit mass of lignin in the 14 different samples can be characterized by a wide range of the values of G. At equilibrium the variation of c/c_0 can be as large as 0.7. The difference was first attributed to nanofiber mat porosity or fiber sizes which determine accessibility of lignin in the sample to the surrounding water, thus determining the lignin contact with lead ions in water and the adsorption rate. It should be emphasized that lignin leaches from the nanofiber mat as shown in S2, and in the calculation of the ratio c/c_0 and of the specific adsorbance, the mass loss of lignin was accounted for.

Figure 7.5 shows the results on the batch adsorption of lead on four different solid cast lignin-containing films (with their weights being shown in the panels). The results for the

adsorption on solid films (Figure 7.6) are contrasted to those on the nanofiber mats (Figure 7.4). The films also show a split of the results for G(t) into a wide band (cf. Figures 7.4b and 7.5b). However, the equilibrium lead concentrations for these four (film) samples are much closer to each other (Figure 7.5a) than those for the nanofiber mats (Figure 7.4a). This would indicate that the total mass of lead adsorbed on the films in all the trials is comparable. As a result, presumably the heavier films adsorb less lead per unit mass of lignin since they possess the same surface area as the lighter films**.** The former expose less percentage of their lignin, which is buried in the bulk in comparison with the latter.

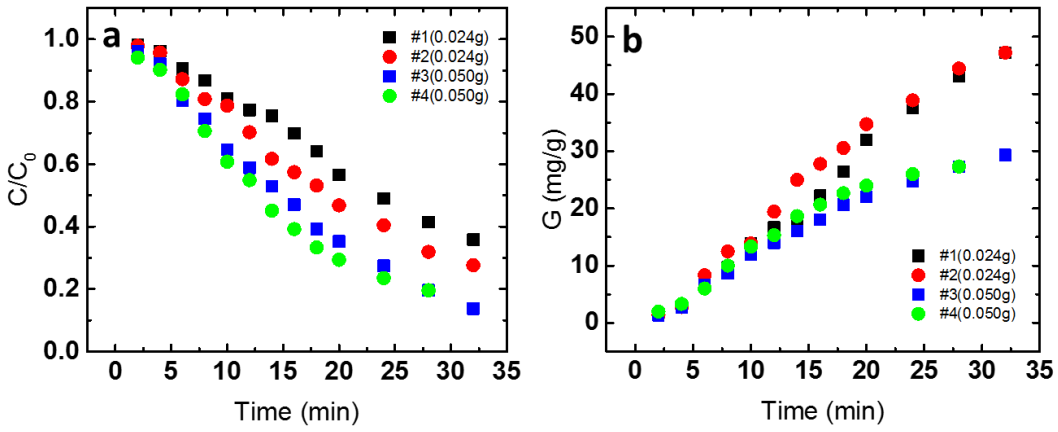

Figure 7.5. Lead adsorption on solid lignin films. (a) Lead concentration as a function of time. (b) The adsorption per unit weight of the adsorbent as a function of time. Different symbols correspond to 4 different films with the initial mass of each film being shown in the panels.

Since the results shown in Figure 7.4b pointed out at a potential effect of permeability and porosity of nanofiber membrane sample on the metal adsorption, measurements of porosity were carried out. To measure porosity of nanofiber mats two different methods were used. First, air filtration was used to measure sample permeability employing Darcy's law $Q = -\left[\left(KA\right)/\mu\right](\Delta p)/\ell$, where Q is the flow rate, A is the projected sample face area, Δp is the air pressures drop across the sample, μ is the air viscosity at room temperature, ℓ is the

sample thickness across the flow, and K is the sample permeability. The filtration setup used in these experiments is shown in Figure A3 in Appendix A. In that setup air was passed through the filter holder containing the membrane and a flowmeter at 9 liter/min. The pressure gauge was used to measure the pressure drop across the filter. The empty filter holder practically did not contribute to the pressure drop. The resulting permeability of the membranes was found to be 3×10^{-11} m^2. The corresponding pore diameter is on the order of 6 μm which is consistent the SEM images in Figure 7.3.

Note also that sample porosity was based on the analysis of SEM images of nanofiber mats as described in Figure A5 in Appendix A. The resulting average porosity value was P=0.54.

The results for the lead absorption on the nanofiber mats with known porosity per unit mass of the adsorbent (lignin) are shown in Figure 7.6. The fiber-size distributions for these nanofiber mats were also measured using SEM samples. The diameters of the individual fibers were measured in pixels using Photoshop and later rescaled using the scale bars on the images. These fiber-size distributions are shown in Figure 7.7.

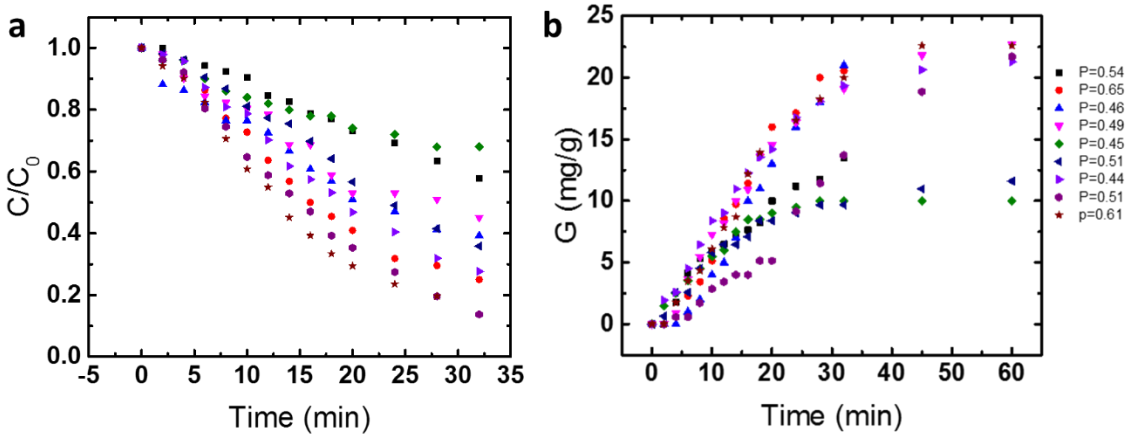

Figure 7.6. Lead adsorption on the lignin-containing nanofiber mats with measured porosity. The results corresponding to different samples are shown by different colors. The sample porosity is denoted as P and listed on the right-hand side for all the samples. (a) Lead concentration c as a function of time. (b) The adsorption per unit weight of the adsorbent.

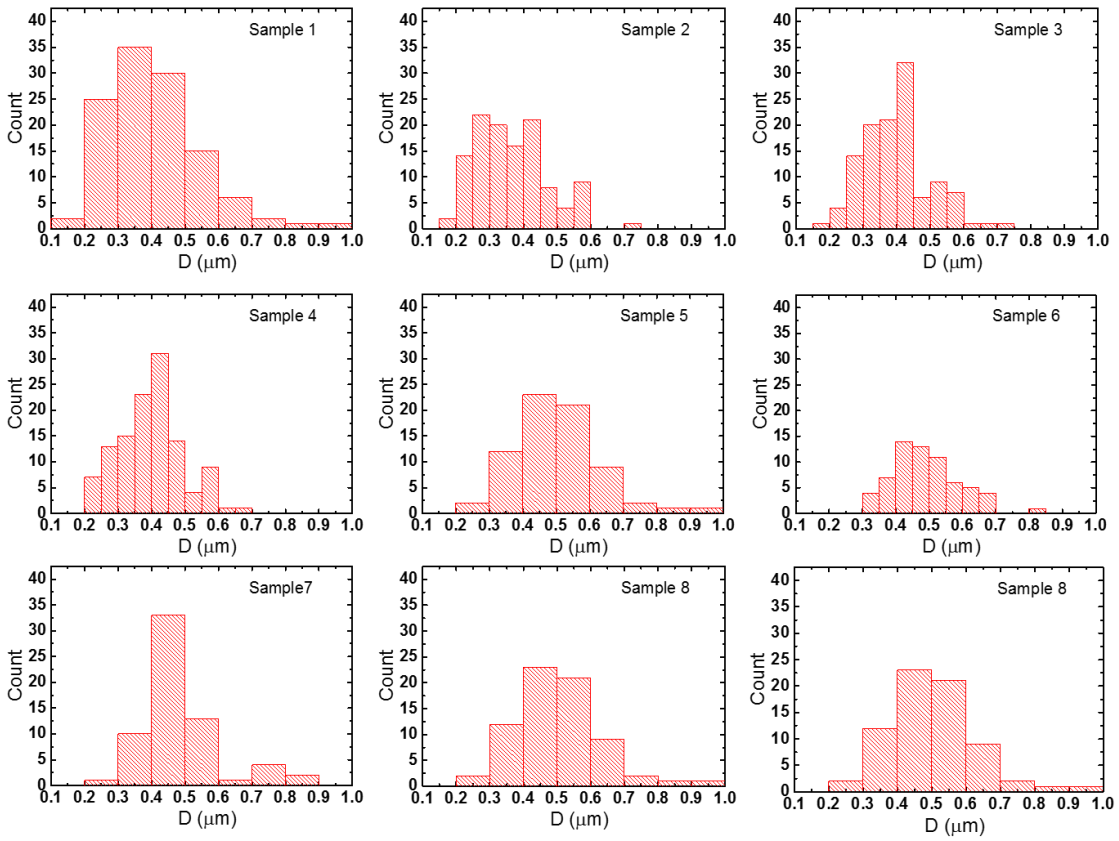

Figure 7.7. Fiber-size distributions in the lignin-containing nanofiber samples.

Figure 7.8 summarizes the effect of the sample porosity and the mean fiber diameter on the maximum adsorption value. It reveals that no clear correlation between either P or D_{mean} to G_{max} is visible.

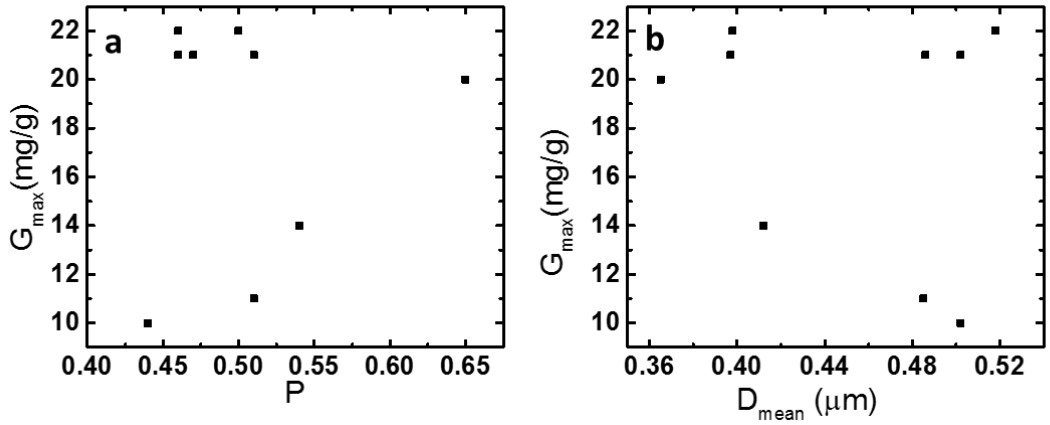

Figure 7.8. (a) Maximum lead adsorption versus sample porosity. (b) Maximum lead adsorption versus the mean fiber diameter in the sample.

7.3.4. Equilibrium Adsorption Isotherm

To elucidate the effect of different biomaterials on G_{max}, the equilibrium adsorption isotherm was measured for lignin- and oat-based nanofibers. The adsorption from lead solution by the lignin- and oat-containing nanofibers at rest is shown in Figure 7.9. The corresponding experimental results can be fitted by eq 7.1. This equation, describing the Langmuir isotherm, can be rearranged as

$$\frac{c_e}{G_{eq}} = \frac{1}{G_{max}} c_e + \frac{1}{K_L G_{max}} \qquad (7.6)$$

Eq 4 can be fitted to the experimental data (cf. Figure 9). Accordingly, the value of G_{max} was found to be 37 mg/g for the lignin-containing nanofiber membranes and 11 mg/g for the oats-containing ones. It can be seen from experimental results that they are not closely fitted by the linear dependence of eq 7.6. It can be attributed to the entrapped air inside nanofiber mat, tortuosity of nanofibers, the insufficient exposure of the active sites to metal solution at different time during the experiment, etc. in the batch experiments. As a result, the throughflow experiments described below are much more appropriate to elucidate the physical kinetics.

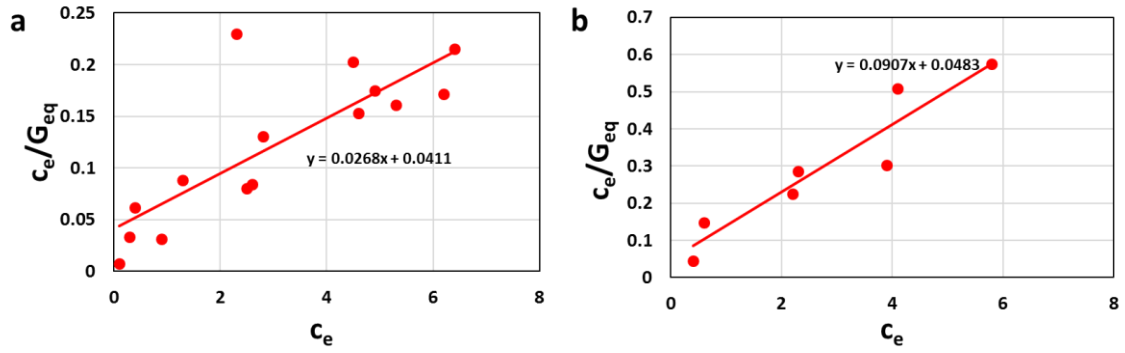

Figure 7.9. Langmuir isotherms for: (a) lignin-containing nanofibers, and (b) oats-containing nanofibers in the aqueous solution of lead in the batch experiment (at rest).

7.3.5. Adsorption on Nanofiber Membranes in Throughflow

All different biopolymer-containing nanofiber mats were tested in a range of pH variation, and thus, the optimized (from the adsorption point of view) pH values were established. Different optimized values of pH for different biopolymers listed below correspond to different content and type of functional moieties in them. The results of adsorption of lead on all the nanofiber membranes are shown in Figure 7.10 and 7.11, with the former showing the change in concentration and the latter - the corresponding mass of heavy metal adsorbed. Different panels in the figure illustrate the process of lead absorption by the lignin nanofibers at pH 2.8, by the alginate nanofibers at pH 4.5, by the oat nanofibers at pH 4.5, by the chitosan nanofibers at pH 4.5, by the soy nanofibers at pH 4.5 and pH 3.5. It can be clearly seen that depending on the biopolymer used, the specific adsorbance varies in the 2-45 mg/g range. This differential capacity of biopolymers provides one with the unique opportunity to tailor need-specific uses in practical applications. It should be emphasized that it was found

that performance of different biopolymers can be optimized at different levels of pH. Figures 7.10e-7.10f show that soy nanofibers adsorb the highest amount of lead at about pH 4.5, which can be attributed to the fact that pH 4.5 corresponds to the isoelectric point of soy nanofibers (Sinha-Ray et al. 2011). For the sake of brevity, the adsorption by other nanofibers at different pH values is not shown here.

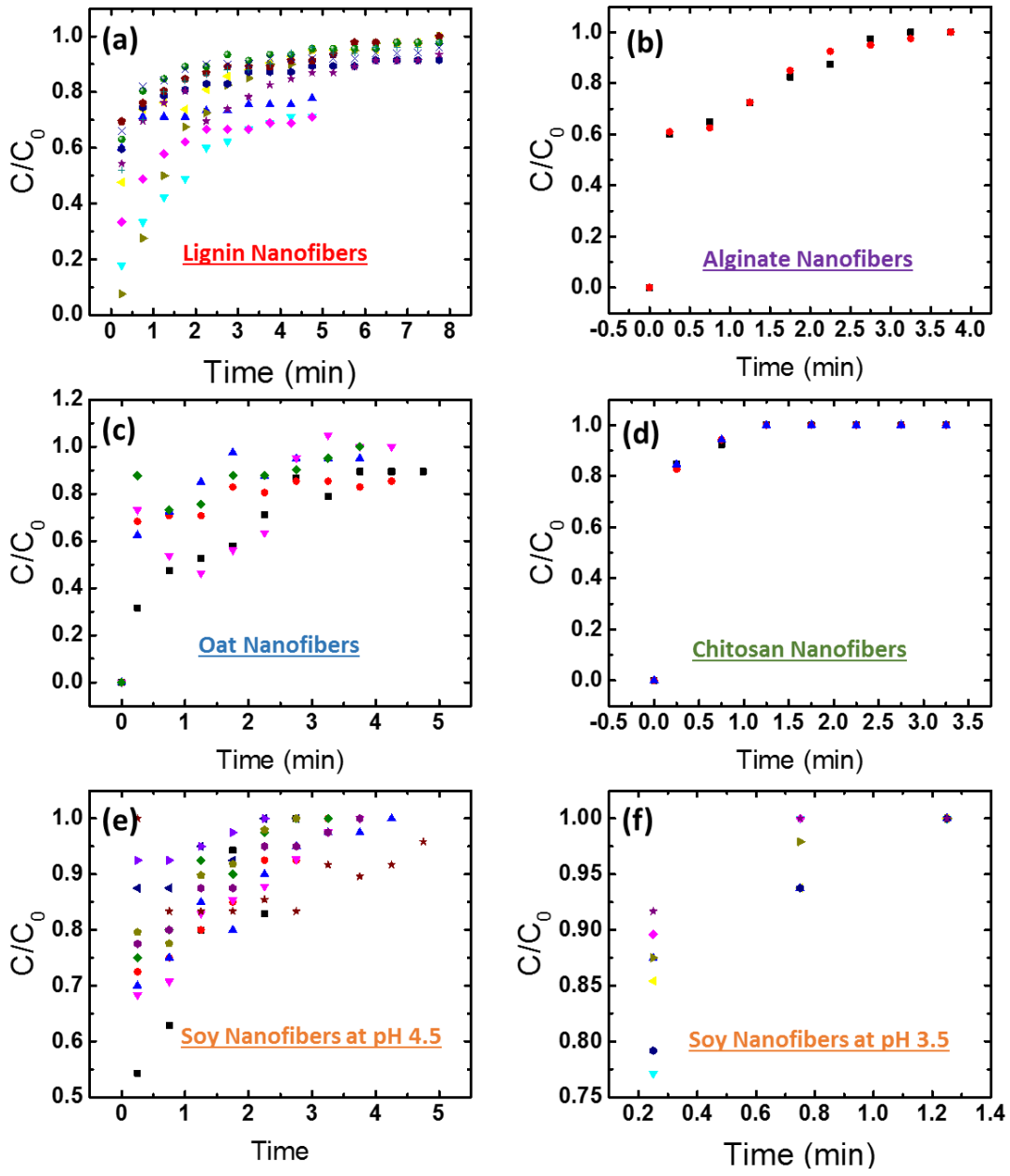

Figure 7.10. Lead adsorption at different nanofibers. (a) Lignin nanofibers (pH 2.8), (b) alginate nanofibers (pH 4.5), (c) oat nanofibers (pH 4.5), (d) chitosan nanofibers (pH 4.5), (e)

soy nanofibers (pH 4.5) and (f) soy nanofibers (pH 3.5). Different symbols correspond to different samples.

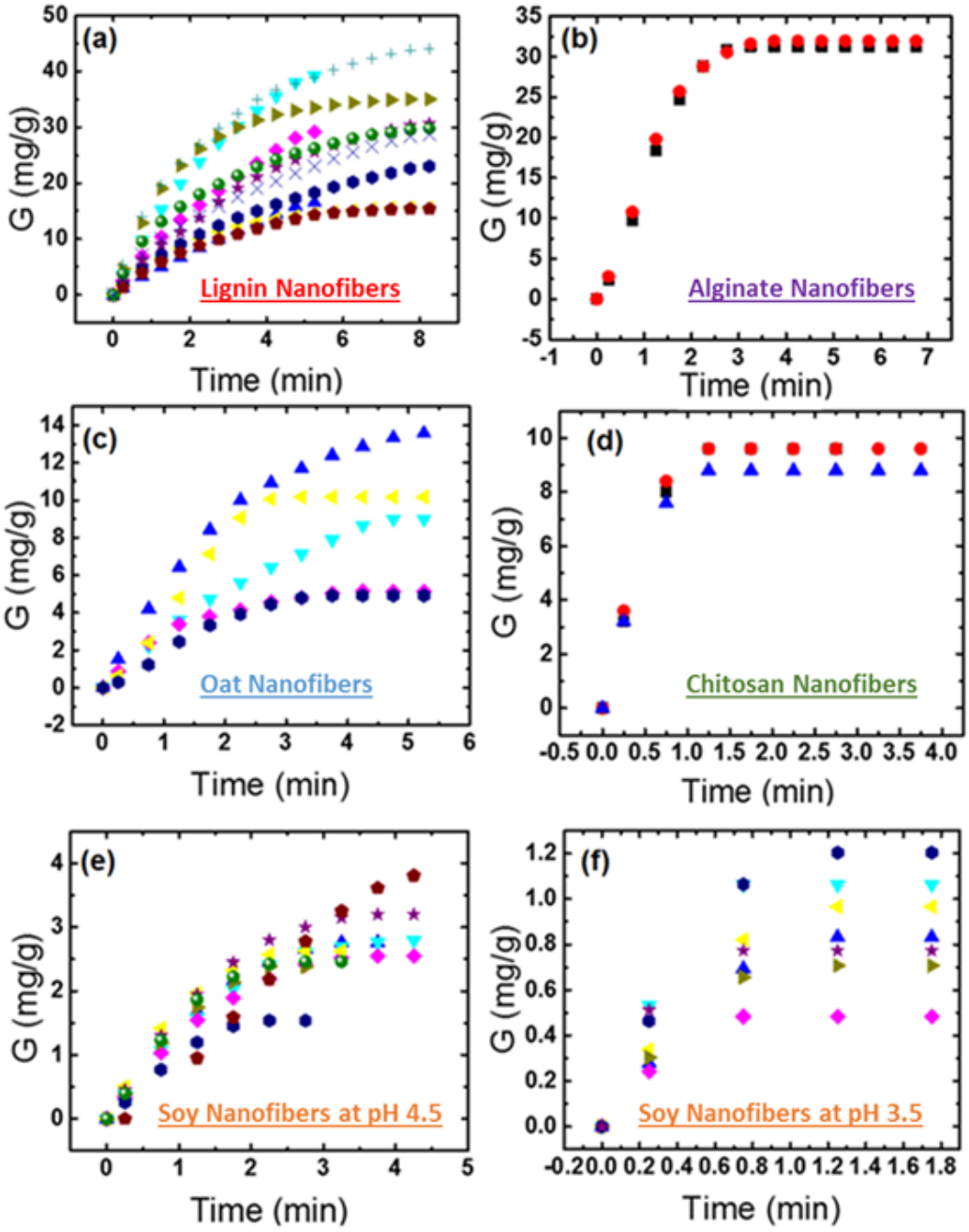

Figure 7.11. Lead adsorption at different nanofibers. (a) Lignin nanofibers (pH 2.8), (b) alginate nanofibers (pH 4.5), (c) oat nanofibers (pH 4.5), (d) chitosan nanofibers (pH 4.5), (e) soy nanofibers (pH 4.5) and (f) soy nanofibers (pH 3.5). Different symbols correspond to different samples. The symbols correspond to the same samples as in Figure 7.10.

Figures 7.11a, 7.11e and 7.11f reveal that the maximum adsorption of lead on lignin- and soy-containing nanofiber membranes is comparable to the results found in the batch adsorption experiments. Nevertheless, there exists a wide data spread within each material, even though the size of all samples was identical and the weight of the samples is accounted for calculating G, which is a specific adsorbance. In the batch adsorption experiments we attempted to correlate this wide data spread with the porosity and the mean nanofiber diameter of the samples. The correlations produced were, however, inconclusive (cf. Figure 7.8). Accordingly, it was logical to study the effect of the membrane thickness on the adsorption curve. Figure 7.12a shows a representative set of the adsorption data for a single-layer soy-containing sample and Figure 7.12b shows the adsorption data for a similar bilayer soy-containing sample. It is seen that doubling the sample thickness almost doubles the value corresponding to the maximum adsorption plateau.

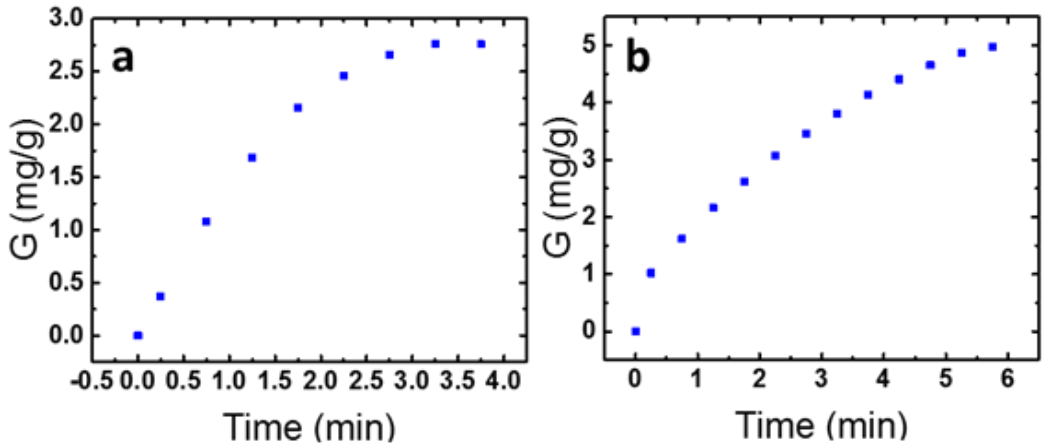

Figure 7.12. Lead adsorption at 4.5 pH on soy-containing nano-textured membrane. (a) A single-layer membrane. (b) A bilayer membrane.

To elucidate the effect of the mat thickness, further experiments were conducted on the lignin- and oats-containing nanofiber membranes. The thickness of the samples was controlled by using either one or two layers of the same nanofiber mat. The results on lead adsorption are shown in Figure 7.13. These results for a single-layer nanofiber mat can be compared with the

equilibrium values found from the Langmuir isotherm for the batch experiments using the lignin- and oat-containing nanofibers found from Figure 7.9 as 37 and 11 mg/g respectively. However, for the bilayer samples, the equilibrium values are significantly higher. It can be concluded that the equilibrium adsorption values are unable to account for the variation in the sample thickness and should be used only as a coarse preliminary estimates. It should be emphasized that in Figure 7.13 the results obtained in the throughflow experiments with the single-layer membranes (shown by circles) significantly differ from those for the bilayer membranes (shown by squares).

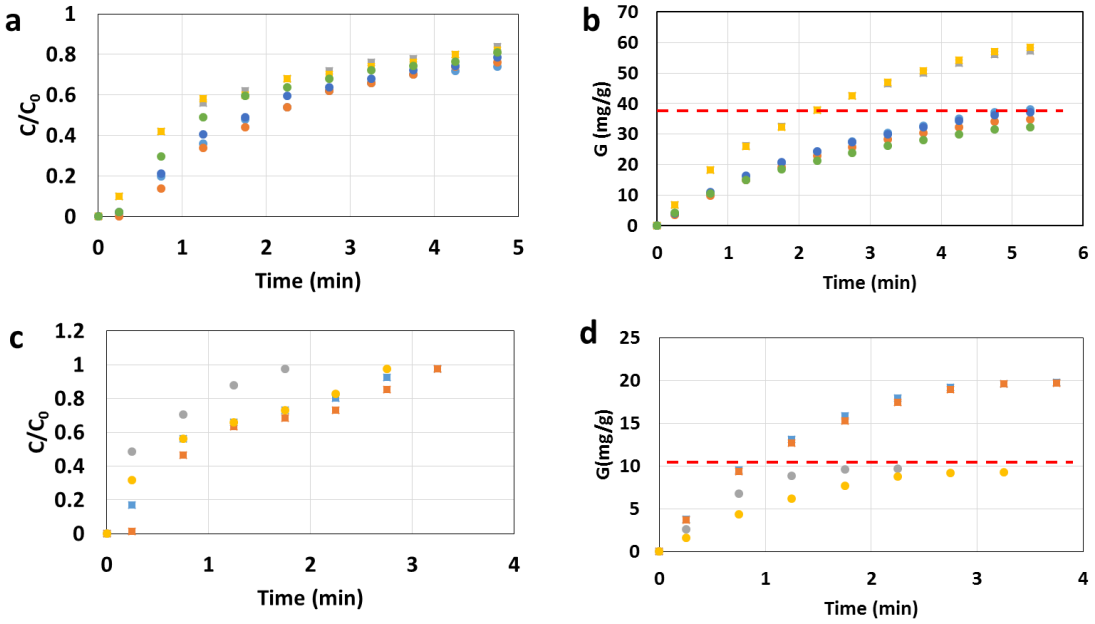

Figure 7.13. The adsorption kinetics on: (a,b) lignin-containing nanofibers, and (c,d) oats-containing nanofibers measured in the throughflow experiments (shown by symbols). The results for single-layer membranes are shown by circles; the results for the bilayer membranes are shown by squares. The dashed lines correspond to the equilibrium values obtained from the Langmuir isotherm for both materials.

7.3.6. Adsorption Kinetics Model and Comparison with the Data from the Throughflow Experiments

The existing literature contains some works aiming at the adsorption kinetics of heavy metal ions on biomaterials (Zümriye 2005; Jain et al. 2016). However, these works do not employ any fundamental theory to rationalize the experimental results. Simple kinetic models such as the following pseudo-first order equation

$$\frac{dq_t}{dt} = k_1(q_e - q_t) \tag{7.7}$$

are used, where q_e and q_t are the amounts of metal adsorbed at equilibrium and at a given time t, respectively, and k_1 is the first order rate constant.

The second commonly used model is the pseudo-second order model which reads

$$\frac{dq_t}{dt} = k_1(q_e - q_t)^2 \tag{7.8}$$

where k_2 is the second order rate constant.

The solutions of eqs 7.7 and 7.8 can be expressed in the following linear forms. Namely, the pseudo-first order kinetics equation reveals

$$\ln(q_e - q_t) = \ln(q_e) - k_1 t \tag{7.9}$$

while the pseudo-second order kinetics equation yields

$$\frac{t}{q_t} = \frac{1}{k_2 q_e^2} + \frac{t}{q_e} \tag{7.10}$$

In both cases the rate constants can be determined from the intercepts of the resultant lines fitted to the experimental data. In the present work both eqs 7.9 and 7.10 were fitted to the data for the lignin-containing nanofibers in throughflow and the results are shown in Figure 7.14. The empirically fitted time rate constants, thus obtained, are listed in Table 7.1. As can be seen, both models can fit the experimental data. However, they result in different values of the kinetic

constants for the samples of different thicknesses produced from the same material. This drawback reveals the unphysical behavior of the fully empirical models given by eqs 7.9-7.12. A new theoretical framework would be required to explain all the experimental observations on the physical grounds. This framework is developed and compared with the experimental data in the present section.

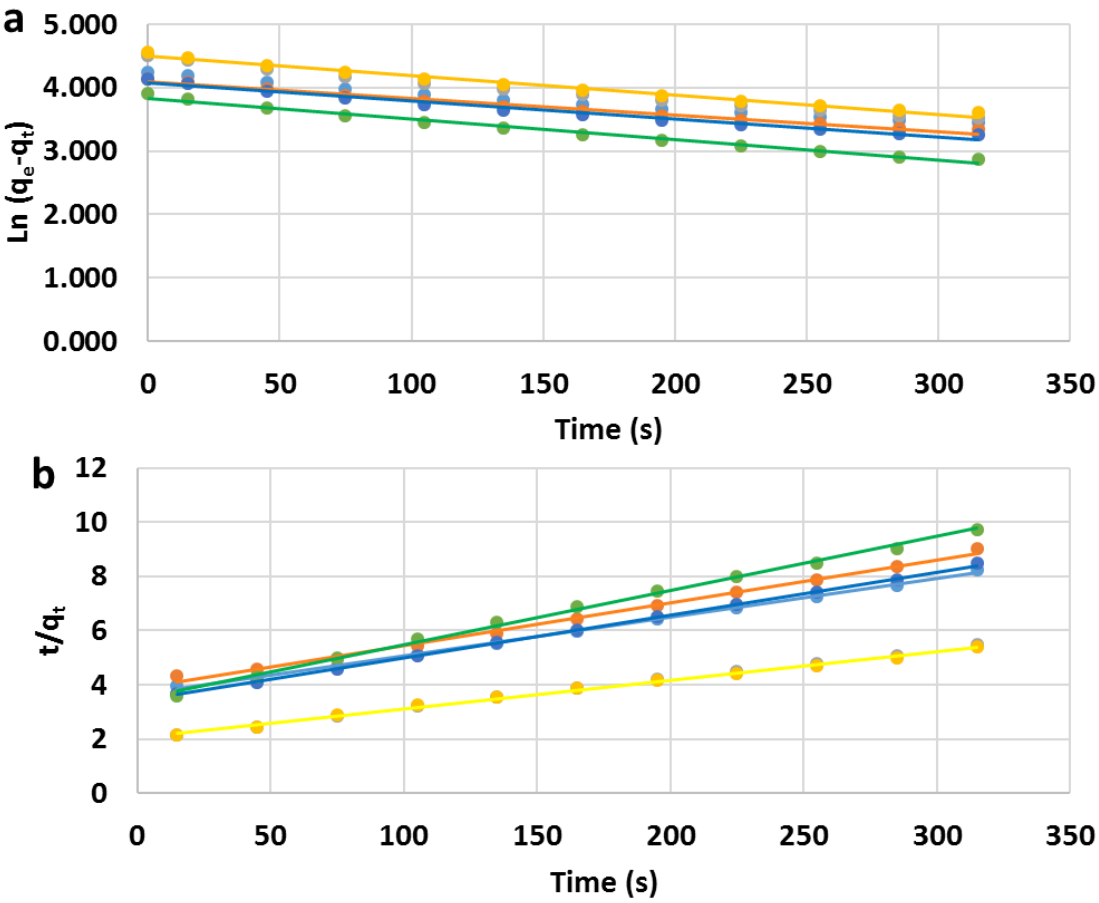

Figure 7.14. (a) Pseudo-first and (b) pseudo-second order kinetic models fitted to the data for the lead adsorption on nano-textured lignin membranes in the throughflow experiments. The experimental data are shown by symbols with different colors representing different samples. The empirical fitting results are shown by the corresponding curves.

Table 7.1. Mass of the adsorbent (lignin), the corresponding adsorption capacity, and the resultant kinetics time constants for the results shown in Figure 15. The constants are found from the fitting of the empirical pseudo-first and pseudo-second order models.

Experiment	**1**	**2**	**3**	**4**	**5**	**6**
Mass of the adsorbent (g)	0.0065	0.0073	0.0033	0.0033	0.0060	0.0063
G (mg/g)	38.15	34.90	57.23	58.46	37.08	32.34
Sample thickness ℓ (cm)	0.011	0.012	0.009	0.009	0.011	0.01
k_1 (1/s)	-0.15	-0.16	-0.19	-0.18	-0.17	-0.20
$k_2 \times 10^5$ (g/mg s)	5.69	6.50	5.89	5.32	7.44	1.15

The new model theoretical framework proposed here to describe and explain the adsorption of metal ions on biopolymer-containing nanofiber membranes in the throughflow experiments is based on the following valid approximation that the pore size, which is on the scale of 4 μm, is much smaller than the membrane thickness, which is of the order of 300 μm. The characteristic time of metal ion diffusion across a single pore is estimated as

$$\tau_{pore} \approx \frac{d^2}{D} \tag{7.11}$$

where d is the pore diameter and D is the ion diffusion coefficient. The characteristic time of metal diffusion across the membrane is

$$\tau_{filter} \approx \frac{\ell^2}{D} \tag{7.12}$$

where ℓ is the nanofiber membrane thickness.

The characteristic flow time is estimated as

$$\tau_{flow} \approx \frac{\ell}{v} \tag{7.13}$$

where v is the velocity of the filtration flow.

The diffusion coefficient of lead can be estimated by Einstein's equation as

$$D = \frac{k_B T}{6\pi\mu r} \tag{7.14}$$

where k_B is Boltzmann's constant, T is the absolute temperature, μ is the water viscosity, and r is the ion radius. The filtration flow through a nano-textured membrane is similar to a flow through a porous medium. In both cases, the diffusion coefficient should be adjusted to account for the effect of the porosity on the diffusion coefficient, which differs from the one in an unconfined surroundings. This is accounted for in the following expression (Davison and Trumbore 1995)

$$\frac{D_m}{D_0} = P^{4/3} \tag{7.15}$$

with D_0 being the diffusion coefficient in an unconfined water, and D_m being the diffusion in the membrane of porosity P.

According to the experimental data discussed above, the average porosity of solution blown membranes can be taken for the estimate as P= 0.5. Lead in water at room temperature has the diffusion coefficient of $D_0=4.8\times10^{-6}$ cm^2/s. The membrane thickness is of the order of $\ell = 3\times10^{-2}$ cm. Given the volumetric flow rate and the filter diameter, which are 20 mL/min and 4.1 cm, respectively, the filtration flow velocity v is about 4×10^{-2} cm/s. Accordingly, $\tau_{pore}=10^{-2}$ s and $\tau_{filter}=10^3$ s. The characteristic flow time τ_{flow} is of the order of 1 s. Therefore, one can assume a uniform ion concentration across the pores, even though a concentration gradient across the membrane should be accounted for.

In the present model, the ion adsorption reaction is assumed to be of the second order, with the second component being the fraction of the free sites (in the Langmuirian sense) at the adsorbent surface. Then, the convection-diffusion equation for the metal ion concentration accounting for the adsorption takes the form

$$\frac{\partial \bar{c}}{\partial t} + v\frac{\partial \bar{c}}{\partial x} = D\frac{\partial^2 \bar{c}}{\partial x^2} - k\bar{c}\theta \tag{7.16}$$

where $\bar{c}$ is the dimensionless free metal ion concentration, θ is the fraction of the free sites at the adsorbent surface, and k is the adsorption rate; t is time and x is the coordinate across the membrane normal to its surface.

The fraction of the free sites changes accordingly, as

$$\frac{\partial\theta}{\partial t} = -k\bar{c}\theta \tag{7.17}$$

Rendering eqs 7.16 and 7.17 dimensionless using τ_{filter} as the time scale and ℓ as the length scale, the following dimensionless equations are obtained

$$\frac{\partial\bar{c}}{\partial\bar{t}} + Pe\frac{\partial\bar{c}}{\partial\bar{x}} = \frac{\partial^2\bar{c}}{\partial\bar{x}^2} - Da\times\bar{c}\theta \tag{7.18}$$

$$\frac{\partial\theta}{\partial\bar{t}} = -Da\times\bar{c}\theta \tag{7.19}$$

where Pe and Da are the dimensionless Peclet and Damkohler numbers, respectively. They are defined according to the following expressions

$$Pe = \frac{v\ell}{D} \tag{7.20}$$

$$Da = \frac{k\ell^2}{D} \tag{7.21}$$

The boundary conditions at t>0 are imposed as following

$$\bar{x} = 0, \bar{c} = 1; \quad \bar{x} = 1, \frac{\partial\bar{c}}{\partial\bar{x}} = 0 \tag{7.22}$$

The initial conditions at t=0 are imposed as

$$\bar{c} = 1, \quad \theta = 1 \tag{7.23}$$

Integrating eq 7.18 over $\bar{x}$, one obtains

$$\frac{d}{d\bar{t}}\int_0^1 \bar{c}d\bar{x} + Pe\bar{c}\,|_0^1 = \frac{\partial\bar{c}}{\partial\bar{x}}\,|_0^1 - Da\int_0^1 \bar{c}\theta\bar{x} \tag{7.24}$$

Then, the integral in time yields

$$\left(\int_0^1 \bar{c}d\bar{x} - 1\right) + Pe\int_0^{\bar{t}} (1-\bar{c}_1)d\bar{t} + \int_0^{\bar{t}} \frac{\partial \bar{c}}{\partial \bar{x}}|_{\bar{x}=0}\, d\bar{t} = -Da\int_0^{\bar{t}}\int_0^1 \bar{c}\theta d\bar{x}d\bar{t} \qquad (7.25)$$

where subscript 1 denotes the concentration at $\bar{x} = 1$.

The specific absorbance measured in the experiments is

$$G(t) = \int_0^t (c_0 - c_0\bar{c}_1)vSdt = c_0\ell APe\int_0^{\bar{t}} (1-\bar{c}_1)d\bar{t} \qquad (7.26)$$

where A is the projected face area of the membrane, and c_0 is the initial dimensional concentration of metal ions in water.

Rearranging eq 7.25, one obtains

$$Pe\int_0^{\bar{t}} (1-\bar{c}_1)d\bar{t} = -Da\int_0^{\bar{t}}\int_0^1 \bar{c}\theta d\bar{x}d\bar{t} - \left(\int_0^1 \bar{c}d\bar{x} - 1\right) - \int_0^{\bar{t}} \frac{\partial \bar{c}}{\partial \bar{x}}|_{\bar{x}=0}\, d\bar{t} \qquad (7.27)$$

where the term $-Da\int_0^{\bar{t}}\int_0^1 \bar{c}\theta d\bar{x}d\bar{t}$ indicates the mass of metal ions adsorbed by the membrane.

Accordingly,

$$G = c_0\ell ADa\int_0^{\bar{t}}\int_0^1 \bar{c}\theta d\bar{x}d\bar{t} \qquad (7.28)$$

The numerical results show that as $\bar{t} \to \infty$, the factor $Da\int_0^{\bar{t}}\int_0^1 \bar{c}\theta d\bar{x}d\bar{t} = 1$ for any values of Pe and Da, since over a long time all metal ions are inevitably adsorbed on the membrane. Therefore, for $\bar{t} \to \infty$, G=constant$\times\ \ell$, which is fully corroborated by the experimental data shown in Figures 7.15b and 7.15d. In this figures the experimental data is normalized according to the theoretical predictions, and the results collapsed onto a single theoretical curved predicted by the theory. Namely, for the comparison of experimental results with the theory, the data was rendered dimensionless by ℓ^2/D and G_{max}. Therefore, using the experimentally measured values of G_{max} as a scale, one accounts for the real value of the average pore length ℓ (accounting for its tortuosity). The data was then fitted to the theoretical predictions by

adjusting the value of the Damkohler number, i.e. the adsorption rate term which is unique for every material.

It should be emphasized that the initial comparisons between the experimental data and the theory as shown in Figures 7.15a and 7.15c revealed discrepancies an incomplete data collapse to the theoretical curve. The origin of these discrepancies was due to an inaccurate measurement of the nanofiber membrane thicknesses. It was found that some small air bubbles which remained inside the filters could potentially block the flow through parts of the membrane, thus reducing the adsorption rate. The issue of accurate membrane thickness measurement was resolved. The thickness of the nanofiber membrane was measured by placing the membrane between two thin glass slides and then measuring the gap by focusing an optical microscope on the adjacent surfaces of the slides. The thickness was measured for both dry (before the filtration) and wet (after the filtration) membranes. It was found that the wet thickness of the membrane can be measured more accurately. Then, the data was rendered dimensionless, and the results were found to fully collapse on the theoretical curve, as is seen in Figures 7.15b and 7.15d with only minor deviations still visible at the dimensionless times $\bar{t} > 2.5$ and $\bar{t} > 1.5$, respectively. It should be emphasized that in spite of these deviations from the theoretical curve the dimensionless data for different membranes stayed collapsed, which ascertains the validity and applicability of the basic principles involved in the present theoretical model. Still, the minor deviations of the collapsed experimental data from the theoretical predictions in Figures 7.15b and 7.15d at the dimensionless times $\bar{t} > 2.5$ and $\bar{t} > 1.5$ deserve an additional comment. They seemingly stem from delayed discharge of ions adsorbing on non-conducting biopolymer-containing membranes. As a result, there should exist a long-lasting Coulombic repulsion between the already adsorbed but still not discharged ions, and the approaching ions. Such a repulsion makes some still empty adsorbing sites on the membrane surface inaccessible, and thus, the fraction of the occupied sites 1-θ stays below the

maximum value of one. Accordingly, the experimentally measured collapsed data for the dimensionless specific adsorbance G in Figures 7.15b and 7.15d saturate below the predicted master curves. The incorporation of the Coulombic repulsion effect in the governing equations (18) and (19) extends beyond the scope of the present work and will be attempted in future.

Accordingly, the lead adsorption rates on lignin and oats are found to be k=0.016 1/s and k=0.010 1/s, respectively. It is seen that unlike the empirical pseudo-first and pseudo-second order kinetics fitting mentioned above, the collapse of the experimental data onto a single curve in the dimensionless form for different samples substantiates the present theoretical model. This also means that the resulting lead adsorption kinetic parameters (for lignin and oats, k=0.016 1/s and k=0.010 1/s, respectively) would not change from one experiment to another, as in the case of the empirical pseudo-first and pseudo-second order kinetics fittings (on the latter, cf. Table 7.1). Accordingly, the present model and experiments allow one to establish the real physical parameters of a given metal adsorption process on a given nano-textured membrane.

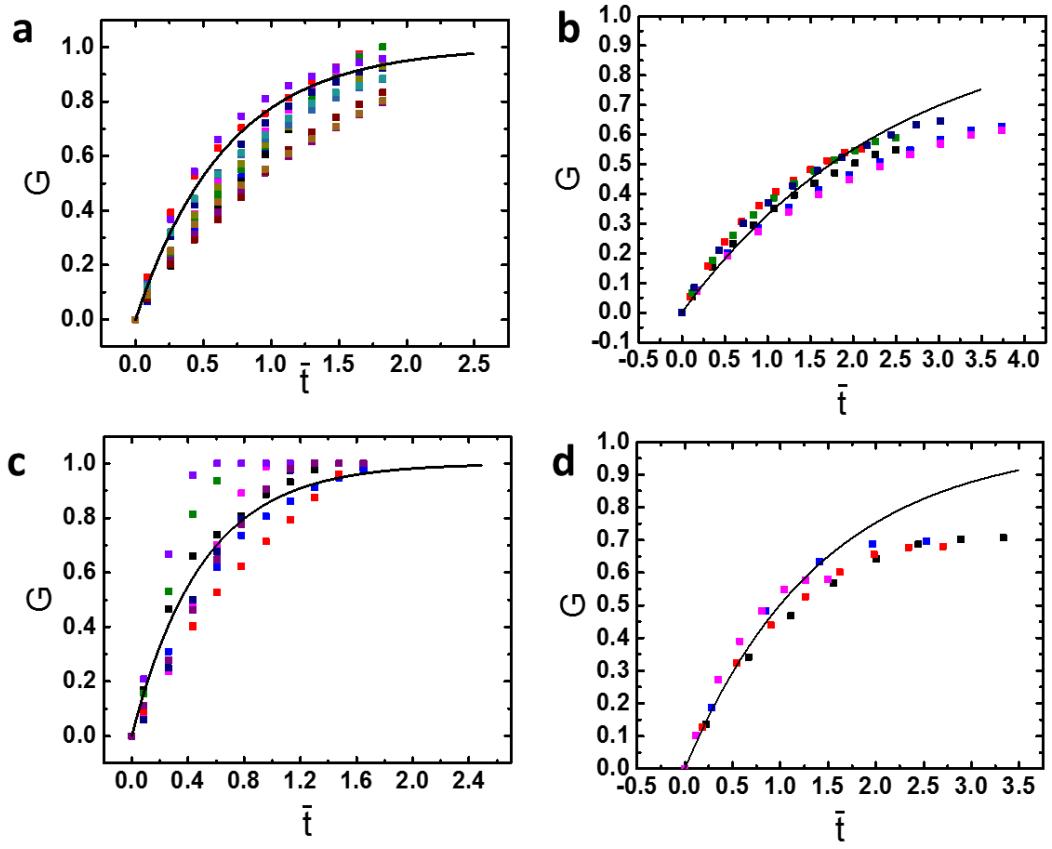

Figure 7.15. Dimensionless specific adsorbance on (a,b) lignin- and (c,d) oats-containing nano-textured membranes. Here the specific adsorbance G is the rendered dimensionless by G_{max} and $\bar{t}$ is the dimensionless time rendered dimensionless by ℓ^2 / D. The experimental data are shown by symbols with different colors corresponding to the results of different samples. The theoretical results are shown by curves.

Commercial alternatives exist for the industrial adsorption of heavy metals. However, the comparison of Table 7.2 with Figure 7.9 show that the maximum adsorption capacity of most alternative materials is on the same scale as that of the biopolymer adsorbents, with the latter being at least 50% less expensive (according to an online market place alibaba.com). Additionally, the conventional adsorbent materials exist in the powder form. Powder should be normally fixed to be used, which results in a lower available surface area and slower adsorption

kinetics. This makes biopolymer-containing nonwovens an attractive alternative due to their comparable adsorption capacity and kinetics with a lower material cost.

Table 7.2. Adsorption capacity and price of the alternative conventional adsorbents (according to an online market place alibaba.com) in comparison with the lignin- and oat-containing nanofibers.

Adsorbent	Pb (mg/g)	Price ($/Metric Ton)
TiO_2	81.3	1000-3000
Modified AlO_3	100	
ZnO	6.7	2000-2500
CeO_2	9.2	
Activated carbon	26.5	1000-2000
Lignin-containing nanofibers	37	
Oat-containing nanofibers	11	

7.4. Conclusion

The study of the adsorption properties of biopolymer-containing nanofibers was conducted. Nanofiber mats containing such biopolymers as lignin, oats, soy protein, sodium alginate and chitosan were successfully formed using solution blowing. The heavy metal adsorption on these nanofiber mats was studied under the equilibrium, batch and throughflow conditions. It was shown that the equilibrium adsorption results provide an adsorption capacity value of the same order of magnitude as the one measured in the throughflow experiments, albeit the former could serve only as a coarse estimate. It should be emphasized that the equilibrium adsorption is unable to account for the variation in the sample thickness and many other significant physico-chemical parameters of nano-textured biopolymer-containing membranes. The adsorption results obtained in the throughflow experiments were compared with conventional empirical pseudo-first and pseudo-second order kinetics expressions. These expressions can fit the individual adsorption trials accurately. However, when different trials with samples from the same material but different thicknesses, etc. are fitted by them in totality, these purely empirical expressions produce a grossly unphysical result. Namely, different values of kinetic parameters appear for different membranes made of the same material and used for the adsorption of the same metal ions. Accordingly, a novel physically-sound model of the heavy metal adsorption on nano-textured membranes in throughflow has been proposed in the present work. This model accounts for the important convection, diffusion and adsorption mechanisms on the physical grounds. It has been successfully validated by the comparison with the experimental data for multiple experiments with different membranes, the results of which could be collapsed in agreement with the theoretical prediction onto a single curve. This allowed us to measure the lead adsorption kinetic rates for lignin- and oats-containing nanofiber membranes as $k=0.016$ 1/s and $k=0.010$ 1/s, respectively.

Note also that some minor deviations of the collapsed data from the predicted theoretical master curve at long times, can be attributed to the Coulombic repulsion of the adsorbed, but still undischarged, ions. This phenomenon deserves to be tackled in the future work.

Lead is a typical heavy metal pollutant, which was chosen as a primary object in the present research. The subsequent catastrophic lead poisoning recently exposed in Flint, Michigan, unfortunately ascertained this choice. Currently, we also conduct similar experiments with copper and zinc, and the preliminary findings confirm that the results found with lead, and their theoretical interpretation, are generic for the other metal-ion pollutants. In principle, experiments with mercury and arsenic would be also possible using the method we employed, albeit they were not attempted in the present work due to the safety concerns.

8. THEORETICAL AND EXPERIMENTAL STUDY OF PUNCHED LAMINATE COMPOSITES PROTECTED BY OUTER PAPER LAYER

(This chapter has been previously published in Kolbasov, A., Sinha-Ray, S., & Yarin, A. L. (2019). Theoretical and experimental study of punched laminate composites protected by outer paper layer. Journal of the Mechanics and Physics of Solids, 128, 117-136)

8.1. Introduction

Such fibrous materials as paper are significantly larger in the x- and y- (in-plane) directions compared to the z- (out-of-plane) direction. Additionally, the fiber orientation is primarily in the x-y plane. As a consequence, the mechanical properties in the z- direction are significantly different from the properties in the x-y plane. It is difficult to measure properties in the z-direction reliably. This is the goal of the present chapter. In this work a theoretical framework is developed to predict the stress distribution in the core of a two-layer (core/skin) system corresponding to different mechanical properties of the skin (with the latter being paper in the laminated wallboard manufactured by the construction-materials industry). This framework was then used to indirectly measure the mechanical properties of fibrous materials (paper) in the z-direction.

8.2. Theoretical

Planar problems allow significant progress via application of powerful and straightforward methods of the complex Goursat functions without sacrificing and sufficiently closely resembling the general physical content of the corresponding axisymmetric situations (Muskhelishvili 1975, England 1971, Galin 2008). In the rare cases when both planar and axisymmetric solutions are available, the comparison shows that planar solutions capture qualitatively the underlying physics and provide quantitative results which can be inaccurate

up to 30% (Yarin et al. 2017). The approach which employs the complex Goursat functions is adopted here for the theory of punched laminated materials. Two separate problems are considered: (i) the structure punched from both sides, and (ii) the structure resting on rigid foundation and punched only from one side via the skin. The elastic behavior prior to failure is studied to reveal a failure criterion.

8.2.1. Structure punched from both sides

Consider planar problem on squeezing of a two layer system depicted in Fig. 8.1. Material 1, the core, and 2, the skin, have Young's moduli E_1 and E_2, as well as Poisson's ratios ν_1 and ν_2, respectively. The thickness of the upper layer is used as a length scale, therefore the upper boundary of layer 1 is located at y=1 in Fig. 8.1. The interface between the bonded layers is at y=0, and the lower boundary of layer 2 is at y=-H, where H>0 and is dimensionless (the thickness of the layer 2 rendered dimensionless by the thickness of layer 1). In statics, the two-layer system is loaded (punched) in the opposite directions by two forces of the same magnitude, as is schematically shown in Fig. 8.1. The following situations can be considered: equal thicknesses of the two layers (Fig. 8.1a), and thinner lower layer (Fig. 8.1b). The latter situation can be turned around, with the thinner layer 2 being on top, as a skin (Fig. 8.1c).

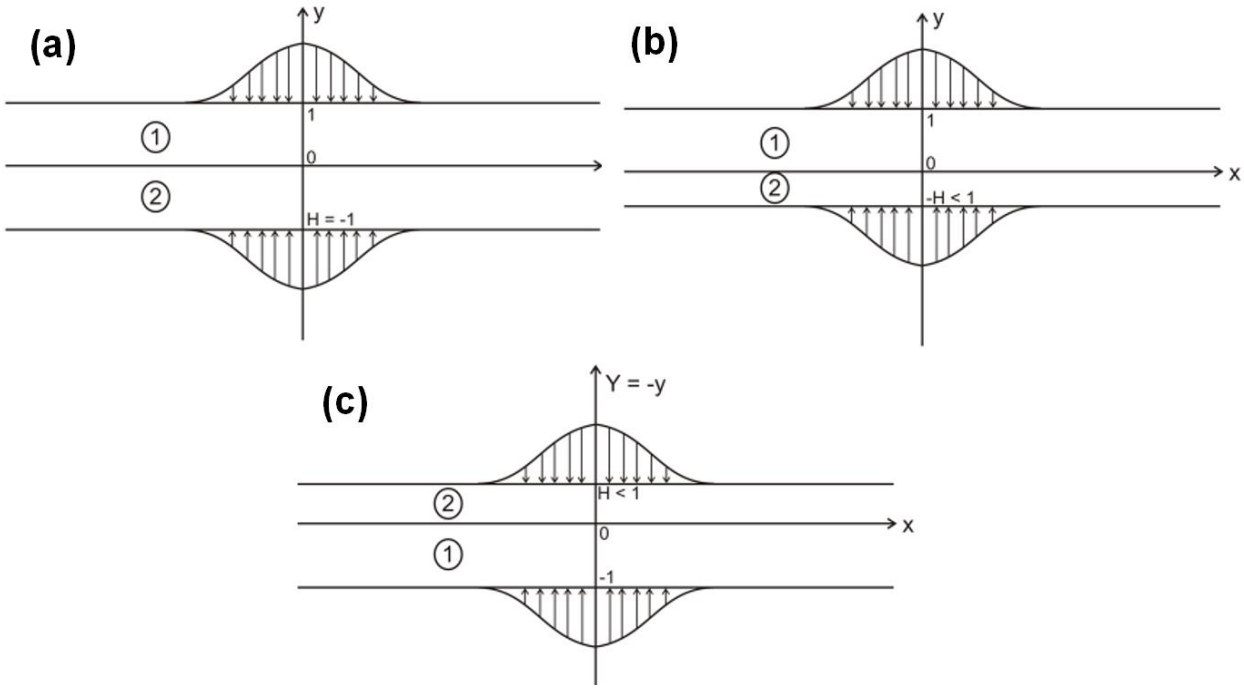

Fig. 8.1. Punching of a double-layer. (a) Symmetric case (both materials can be the same); (2) Asymmetric case; (3) Asymmetric case turned around where material 1 can be considered as a core, and 2 – as a skin).

Such planar problems of the theory of elasticity can be reduced to finding the Airy function U_i which satisfies the biharmonic equation (Muskhelishvili 1975, England 1971, Galin 2008)

$$\frac{\partial^4 U_i}{\partial x^4} + 2\frac{\partial^4 U_i}{\partial x^2 \partial y^2} + \frac{\partial^4 U_i}{\partial y^4} = 0 \tag{8.1}$$

with i=1 or 2 for the layers 1 or 2 in Fig. 8.1. It should be emphasized that the elastic problems are solved piecewise in the separate layers and their solutions will be matched by the appropriate boundary conditions at the interface.

All three components of the stress tensor can be found from the Airy function as

$$\sigma_{xxi} = \frac{\partial^2 U_i}{\partial y^2}\ , \quad \sigma_{xyi} = -\frac{\partial^2 U_i}{\partial x \partial y}, \quad \sigma_{yyi} = \frac{\partial^2 U_i}{\partial x^2} \tag{8.2}$$

The boundary conditions for the stresses at the outer surfaces read

$$y=-H:\quad \sigma_{xy2}=0,\quad \sigma_{yy2}=-P\exp\left(-\alpha^2x^2\right) \tag{8.3}$$

$$y=1:\quad \sigma_{xy1}=0,\quad \sigma_{yy1}=-P\exp\left(-\alpha^2x^2\right) \tag{8.4}$$

where the stress magnitude P>0, and the normal stress distribution corresponding to a punch is chosen for convenience, since it allows a straightforward representation in the form of the following Fourier integral

$$\exp\left(-\alpha^2x^2\right)=\frac{1}{\alpha\sqrt{\pi}}\int_0^{\infty}\exp\left[-k^2/\left(4\alpha^2\right)\right]\cos kx\,dk \tag{8.5}$$

The spectral wavenumbers are denoted as k, and the punch width is varied by changing the value of the dimensionless parameter $\alpha>0$. It should be emphasized that the magnitude of the total compressive force F applied to each outer surface of the two-layer system in Fig. 8.1 corresponding to Eqs. (8.3) and (8.4) is equal to $F=P\left(h\times 1\right)\sqrt{\pi}/\alpha$, where h is the dimensional thickness of layer 1.

The following two boundary conditions at the interface are posed for a complete bonding case, where

$$y=0:\quad \sigma_{xy1}=\sigma_{xy2},\quad \sigma_{yy1}=\sigma_{yy2} \tag{8.6}$$

Two additional boundary conditions are required at the interface, namely the equality of the displacement components on both sides

$$y=0:\quad u_{x1}=u_{x2},\quad u_{y1}=u_{y2} \tag{8.7}$$

where u_x and u_y are the x- and y-components of the displacement vector **u**.

8.2.2. Solution for the Airy function

The solutions of the biharmonic equation (8.1) in the form of the Fourier integral dictated by Eqs. (8.3)-(8.5) read

$$U_j = \int_0^\infty \left(\cosh ky + A_{kj} \sinh ky + C_{kj} y \sinh ky + D_{kj} y \cosh ky\right) E_{kj} \cos kx dk \tag{8.8}$$

where the 8 constants of integration A_{kj}, C_{kj}, D_{kj}, and E_{kj}, with j=1 or 2, are to be found using the boundary conditions (8.3)-(8.7).

Accordingly, the stresses are found from Eqs. (8.2) and (8.8) as the following Fourier integrals

$$\begin{aligned}\sigma_{xxj} = \int_0^\infty (&k^2 \cosh ky + A_{kj} k^2 \sinh ky + 2C_{kj} k \cosh ky + C_{kj} k^2 y \sinh ky \\ &+ 2D_{kj} k \sinh ky + D_{kj} k^2 y \cosh ky) E_{kj} \cos kx dk\end{aligned} \tag{8.9}$$

$$\begin{aligned}\sigma_{xyj} = \int_0^\infty (&k \sinh ky + A_{kj} k \cosh ky + C_{kj} \sinh ky + C_{kj} ky \cosh ky \\ &+ D_{kj} \cosh ky + D_{kj} ky \sinh ky) k E_{kj} \sin kx dk\end{aligned} \tag{8.10}$$

$$\sigma_{yyj} = -\int_0^\infty (\cosh ky + A_{kj} \sinh ky + C_{kj} y \sinh ky + D_{kj} y \cosh ky) k^2 E_{kj} \cos kx dk \tag{8.11}$$

8.2.3. Calculation of displacements

Since the boundary conditions (8.7) at the interface involve the displacements, one needs to find their expressions in addition to those of the stresses given by Eqs. (8.9)-(8.11). The most natural way of doing that, is to employ the solutions of the biharmonic equation (8.1) in the form of the complex Goursat functions $\Pi(z)$ and $\Omega(z)$ of the complex variable $z=x+iy$, where i is the imaginary unit (Muskhelishvili 1975, England 1971, Galin 2008).

Then, the entire general solution of the planar elastic problem for stresses and displacements in any domain (1 or 2) can be present in the following form (with subscript j omitted for brevity)

$$\sigma_{xx} + i\sigma_{xy} = \Pi(z) + \overline{\Pi(z)} - \overline{\Omega(z)} - (z - \bar{z})\overline{\Pi'(z)} \tag{8.12}$$

$$\sigma_{yy} - i\sigma_{xy} = \Pi(z) + \overline{\Pi(z)} + \overline{\Omega(z)} + (z - \bar{z})\overline{\Pi'(z)} \tag{8.13}$$

$$2\mu(u_x + iu_y) = \kappa\int \Pi(z)dz - \overline{\int [\Pi(z) + \Omega(z)]dz} - (z - \bar{z})\overline{\Pi(z)} \tag{8.14}$$

where, as usual, overbar denotes complex conjugate, and prime denotes differentiation by z. Also, μ is the first Lame's coefficient; κ=3-4ν for the plane strain case and $\kappa = (3-\nu)/(1+\nu)$ for the plane stress case (Cherepanov1979), with ν being Poisson's ratio. Note that the Goursat functions Π(z) and Ω(z) are more convenient for the contact problems considered here. They are related to the standard ones, φ(z) and χ(z), as $\Pi(z) = \varphi'(z)$ and $\Omega(z) = z\varphi''(z) + \chi''(z)$.

Applying Eq. (8.12) at the interface y=0, one finds that

$$\sigma_{xx}\big|_{y=0} = 2\,\mathrm{Re}\,\Pi\big|_{y=0} - \mathrm{Re}\,\Omega\big|_{y=0} \tag{8.15}$$

where Re denotes the real part.

Similarly, from Eq. (8.13) one obtains

$$\sigma_{yy}\big|_{y=0} = 2\,\mathrm{Re}\,\Pi\big|_{y=0} + \mathrm{Re}\,\Omega\big|_{y=0} \tag{8.16}$$

From Eqs. (8.15) and (8.16) one can express the real parts of the Goursat functions Π(z) and Ω(z) at the interface y=0 through the values of the normal stresses there as

$$\mathrm{Re}\,\Pi\big|_{y=0} = \frac{1}{4}\left(\sigma_{xx}\big|_{y=0} + \sigma_{yy}\big|_{y=0}\right) \tag{8.17}$$

$$\mathrm{Re}\,\Omega\big|_{y=0} = \frac{1}{2}\left(\sigma_{yy}\big|_{y=0} - \sigma_{xx}\big|_{y=0}\right) \tag{8.18}$$

In addition, both Eq. (8.12) and Eq. (8.13) show that at the interface y=0,

$$\sigma_{xy}\big|_{y=0} = \mathrm{Im}\,\Omega\big|_{y=0} \tag{8.19}$$

where Im denotes the imaginary part.

Applying Eq. (8.14) at the interface y=0, it is easy to find that

$$2\mu u_x\big|_{y=0} = (\kappa - 1)\int \mathrm{Re}\,\Pi\big|_{y=0}dx - \int \mathrm{Re}\,\Omega\big|_{y=0}dx \tag{8.20}$$

$$2\mu u_y\big|_{y=0} = (\kappa+1)\int \mathrm{Im}\,\Pi\big|_{y=0}\mathrm{d}x + \int \mathrm{Im}\,\Omega\big|_{y=0}\mathrm{d}x \tag{8.21}$$

Substituting Eqs. (8.17)-(8.19) into Eqs. (8.20) and (8.21), one finds that

$$2\mu_j u_{xj}\big|_{y=0} = \int_0^x \left[(1-\nu_j)\sigma_{xxj}\big|_{y=0} - \nu_j\,\sigma_{yyj}\big|_{y=0} \right]\mathrm{d}x \tag{8.22}$$

$$2\mu_j u_{yj}\big|_{y=0} = \int_0^x \left[4(1-\nu_j)\,\mathrm{Im}\,\Pi_j\big|_{y=0} + \sigma_{xyj}\big|_{y=0} \right]\mathrm{d}x + \mathrm{const} \tag{8.23}$$

for example, in the plane strain case.

Here subscripts j are introduced once again; they attribute the functions and parameters to different domains, and also accounted for the fact that $u_{xj}=0$ at x=0 due to the symmetry relative to the y-axis, whereas u_{yj} can take at x=0 a certain value denoted as a constant which is not necessarily zero.

Equation (8.22) fully expresses the displacement u_{xj} through the stresses alone, whereas Eq. (8.23) still involves the imaginary part of the Goursat function Π(z) at y=0, which is not expressed through the stresses. To find ImΠ(z) in the entire domain including the interface, note that Eqs. (8.12) and (8.13) lead to the following expressing for ReΠ(z) in the entire domain

$$\mathrm{Re}\,\Pi = \frac{1}{4}(\sigma_{xx}+\sigma_{yy}) \tag{8.24}$$

which extends Eq. (8.17) to the entire domain.

Then, according to the Cauchy-Riemann conditions (Angot 1965, Henrici 1974) the real and imaginary parts of the Goursat function Π(z) in the entire domain are related as

$$\frac{\partial\,\mathrm{Re}\,\Pi}{\partial x} = \frac{\partial\,\mathrm{Im}\,\Pi}{\partial y} \tag{8.25}$$

$$\frac{\partial\,\mathrm{Re}\,\Pi}{\partial y} = -\frac{\partial\,\mathrm{Im}\,\Pi}{\partial x} \tag{8.26}$$

Then, from Eqs. (8.24)-(8.26) one finds

$$\frac{\partial \operatorname{Im}\Pi\big|_{y=0}}{\partial x} = -\frac{1}{4}\left[\frac{\partial}{\partial y}\left(\sigma_{xx}+\sigma_{yy}\right)\right]\Bigg|_{y=0} \tag{8.27}$$

Substituting here Eqs. (8.9) and (8.11), after elementary transformations, one finds

$$\operatorname{Im}\Pi_j\big|_{y=0} = -\frac{1}{2}\int_0^\infty D_{kj} k E_j \sin kx\,dk \tag{8.28}$$

Using Eq. (8.28) in Eq. (8.23), as well as substituting Eqs. (8.9) and (8.11) into Eqs. (8.22) and (8.23), and evaluating all the integrals in x, one finds the displacements at the interface, for example, in the plane strain case in the following form

$$2\mu_j u_{xj}\big|_{y=0} = \int_0^x \left[\left(1-\nu_j\right)\left(k+2C_{kj}+\nu_j k\right)\right] E_{kj} \sin kx\,dk \tag{8.29}$$

$$2\mu_j u_{yj}\big|_{y=0} = \int_0^x \left[2\left(1-\nu_j\right)D_{kj} - A_{kj}k - D_{kj}\right] E_{kj} \cos kx\,dk + \text{const} \tag{8.30}$$

Now Eqs. (8..9)-(11) and (8.29)-(8.30) have an appropriate form to implement all 8 boundary conditions (8.3), (8.4), (8.6) and (8.7) at the interface y=0 and determine all the 8 constants of integration A_{kj}, C_{kj}, D_{kj}, and E_{kj}, with j=1 or 2, and thus the entire solution.

8.2.4. Implementation of the boundary conditions

The boundary conditions (8.3), (8.4), (8.6) and (8.7) at the interface y=0, with Eqs. (8.9)-(8.11) and (8.29)-(8.30) being substituted and accounting for the fact that $\mu_i = E_i(1+\nu_i)$ with E_i being Young's moduli, read

$$\begin{aligned}\int_0^\infty &(-k\sinh kH + A_{k2}k\cosh kH - C_{k2}\sinh kH - C_{k2}kH\cosh kH \\ &+ D_{k2}\cosh kH + D_{k2}kH\sinh kH)kE_{k2}\sin kx\,dk = 0\end{aligned} \tag{8.31}$$

$$\begin{aligned}\int_0^\infty &(\cosh kH - A_{k2}\sinh kH + C_{k2}H\sinh kH - D_{k2}H\cosh kH)(-k^2)E_{k2}\cos kx\,dk \\ &= -\frac{P}{\alpha\sqrt{\pi}}\int_0^\infty \exp\left[-k^2/\left(4\alpha^2\right)\right]\cos kx\,dk\end{aligned} \tag{8.32}$$

$$\int_0^\infty (k\sinh k + A_{k1}k\cosh k + C_{k1}\sinh k + C_{k1}k\cosh k + D_{k1}\cosh k + D_{k1}k\sinh k)kE_{k1}\sin kxdk = 0 \tag{8.33}$$

$$\int_0^\infty (\cosh k + A_{k1}\sinh k + C_{k1}\sinh k + D_{k1}\cosh k)(-k^2)E_{k1}\cos kxdk = -\frac{P}{\alpha\sqrt{\pi}}\int_0^\infty \exp\left[-k^2/\left(4\alpha^2\right)\right]\cos kxdk \tag{8.34}$$

$$\int_0^\infty (A_{k2}k + D_{k2})kE_{k2}\sin kxdk = \int_0^\infty (A_{k1}k + D_{k1})kE_{k1}\sin kxdk \tag{8.35}$$

$$\int_0^\infty k^2E_{k2}\cos kxdk = \int_0^\infty k^2E_{k1}\cos kxdk \tag{8.36}$$

$$\int_0^\infty \frac{E_1(1+\nu_2)}{E_2(1+\nu_1)}\left[(1-\nu_2)(k+2C_{k2}) + \nu_2 k\right]E_{k2}\sin kxdk = \int_0^\infty \left[(1-\nu_1)(k+2C_{k1}) + \nu_1 k\right]E_{k1}\sin kxdk \tag{8.37}$$

$$\int_0^\infty \frac{E_1(1+\nu_2)}{E_2(1+\nu_1)}\left[2(1-\nu_2)D_{k2} - A_{k2}k - D_{k2}\right]E_{k2}\cos kxdk = \int_0^\infty \left[2(1-\nu_1)D_{k1} - A_{k1}k - D_{k1}\right]E_{k1}\cos kxdk \tag{8.38}$$

From Eq. (8.36) one finds that

$$E_{k2} = E_{k1} \tag{8.39}$$

while from Eq. (8.35)

$$A_{k2}k + D_{k2} = A_{k1}k + D_{k1} \tag{8.40}$$

Using Eqs. (8.39) and (8.40), one reduces Eqs. (8.31)-(8.34) and (8.37)-(8.38) to the following system of the algebraic equations for the unknown constants of integration

$$-k\sinh kH + (A_{k1}k + D_{k1})\cosh kH - C_{k2}(\sinh kH + kH\cosh kH) + D_{k2}kH\sinh kH = 0 \tag{8.41}$$

$$\left[\cosh kH-\left(A_{k1}+\frac{D_{k1}-D_{k2}}{k}\right)\sinh kH+C_{k2}H\sinh kH-D_{k2}H\cosh kH\right]k^2E_{k1} = \frac{P}{\alpha\sqrt{\pi}}\exp\left[-k^2/\left(4\alpha^2\right)\right] \tag{8.42}$$

$$k\sinh k+A_{k1}k\cosh k+C_{k1}\left(\sinh k+k\cosh k\right)+D_{k1}\left(\cosh k+k\sinh k\right)=0 \tag{8.43}$$

$$\left(\cosh k+A_{k1}\sinh k+C_{k1}\sinh k+D_{k1}\cosh k\right)k^2E_{k1}=\frac{P}{\alpha\sqrt{\pi}}\exp\left[-k^2/\left(4\alpha^2\right)\right] \tag{8.44}$$

$$\frac{E_1(1+\nu_2)}{E_2(1+\nu_1)}\left[(1-\nu_2)(k+2C_{k2})+\nu_2k\right]=\left[(1-\nu_1)(k+2C_{k1})+\nu_1k\right] \tag{8.45}$$

$$\frac{E_1(1+\nu_2)}{E_2(1+\nu_1)}\left[2(1-\nu_2)D_{k2}-A_{k1}k-D_{k1}\right]=\left[2(1-\nu_1)D_{k1}-A_{k1}k-D_{k1}\right] \tag{8.46}$$

Then, from Eq. (8.45) one obtains the relation

$$C_{k2}=m_1C_{k1}+m_2 \tag{8.47}$$

where the coefficients m_1 and m_2 are known as

$$m_1=\frac{E_2\left(1-\nu_1^2\right)}{E_1\left(1-\nu_2^2\right)},\quad m_2=\left[\frac{E_2\left(1+\nu_1\right)}{E_1\left(1+\nu_2\right)}-1\right]\frac{k}{2\left(1-\nu_2\right)} \tag{8.48}$$

Also, from Eq. (8.46) one obtains the following relation

$$D_{k2}=m_3D_{k1}-m_2A_{k1} \tag{8.49}$$

where

$$m_3=\left[\frac{E_2\left(1+\nu_1\right)\left(1-2\nu_1\right)}{E_1\left(1+\nu_2\right)}+1\right]\frac{1}{2\left(1-\nu_2\right)} \tag{8.50}$$

Substituting the relations (8.47) and (8.49) into Eqs. (8.41), (8.42) and (8.44), one reduces them to the following two equations

$$a_{11}A_{k1}+a_{12}C_{k1}+a_{13}D_{k1}=b_1 \tag{8.51}$$

$$a_{21}A_{k1}+a_{22}C_{k1}+a_{23}D_{k1}=b_2 \tag{8.52}$$

where the coefficients are known as

$$\begin{aligned} a_{11} &= k\cosh kH - m_2 kh\sinh kH, \quad a_{12} = -m_1\left(\sinh kH + kH\cosh kH\right) \\ a_{13} &= \cosh kH + m_3 kH\sinh kH, \quad b_1 = k\sinh kH + m_2\left(\sinh kH + kH\cosh kH\right) \end{aligned} \tag{8.53}$$

$$\begin{aligned} a_{21} &= -\left(\sinh kH + \sinh k\right) - m_2\left(\frac{\sinh kH}{k} - H\cosh kH\right), \quad a_{22} = -\sinh k + m_1 H\sinh kH \\ a_{23} &= -\left(\cosh k + \frac{\sinh kH}{k}\right) + m_3\left(\frac{\sinh kH}{k} - H\cosh kH\right), \quad b_2 = -m_2 H\sinh kH + \cosh k - \cosh kH \end{aligned} \tag{8.54}$$

Also, Eq. (43) can be re-written as

$$a_{31}A_{k1} + a_{32}C_{k1} + a_{33}D_{k1} = b_3 \tag{8.55}$$

where

$$a_{31} = k\cosh k, \quad a_{32} = \sinh k + k\cosh k, \quad a_{33} = \cosh k + k\sinh k, \quad b_3 = -k\sinh k \tag{8.56}$$

Equations (8.51), (8.52) and (8.55) form a system of three algebraic equations for the three unknowns A_{k1}, C_{k1} and D_{k1}. Its solution reads

$$A_{k1} = \left(b_1 a_{22} a_{33} + a_{12} a_{23} b_3 + a_{13} b_2 a_{32} - b_3 a_{22} a_{13} - a_{32} a_{23} b_1 - a_{33} b_2 a_{12}\right)/m_4 \tag{8.57}$$

$$C_{k1} = \left(a_{11} b_2 a_{33} + b_1 a_{23} a_{31} + a_{13} a_{21} b_3 - a_{31} b_2 a_{13} - b_3 a_{23} a_{11} - a_{33} a_{21} b_1\right)/m_4 \tag{8.58}$$

$$D_{k1} = \left(a_{11} a_{22} b_3 + a_{12} b_2 a_{31} + b_1 a_{21} a_{32} - a_{31} a_{22} b_1 - a_{32} b_2 a_{11} - b_3 a_{21} a_{12}\right)/m_4 \tag{8.59}$$

where the denominator m_4 is given by

$$m_4 = a_{11} a_{22} a_{33} + a_{12} a_{23} a_{31} + a_{13} a_{21} a_{32} - a_{31} a_{22} a_{13} - a_{32} a_{23} a_{11} - a_{33} a_{21} a_{12} \tag{8.60}$$

After the constants of integration A_{k1}, C_{k1} and D_{k1} are found using the expressions (8.57)-(8.60), the constant of integration E_{k1} is found from Eq. (8.44) as

$$E_{k1} = \frac{P}{\alpha\sqrt{\pi}}\exp\left[-k^2/\left(4\alpha^2\right)\right]\frac{1}{k^2\left(\cosh k + A_{k1}\sinh k + C_{k1}\sinh k + D_{k1}\cosh k\right)} \tag{8.61}$$

Then, E_{k2} is found from Eq. (8.39), C_{k2} is found from Eq. (8.47), and D_{k2} is found from Eq. (8.49). Then, finally A_{k2} is found from Eq. (8.40) as

$$A_{k2} = A_{k1} + \frac{D_{k1} - D_{k2}}{k} \tag{8.62}$$

After all eight constants of integration are found as described above, the stress fields in both domains are calculated from Eqs. (8.9)-(8.11), and the displacements of material elements located at the interface are calculated in the plane strain case from Eqs. (8.29) and (8.30).

In the experiment, the difference of the principal stresses σ_1-σ_2, the sum of the principal stresses σ_1+σ_2, and the angle θ between the principal axes and the Cartesian coordinate system x,y can be measured. In parallel, they are predicted using the theoretical results revealed above, as

$$\left(\sigma_1-\sigma_2\right)_j=\sqrt{\left(\sigma_{xxj}-\sigma_{yyj}\right)^2+4\sigma_{xyj}^2} \tag{8.63}$$

$$\left(\sigma_1+\sigma_2\right)_j=\left(\sigma_{xxj}+\sigma_{yyj}\right) \tag{8.64}$$

$$\tan 2\theta_j=\frac{2\sigma_{xyj}^2}{\sigma_{xxj}-\sigma_{yyj}} \tag{8.65}$$

8.2.5. Laminate material on a rigid foundation punched through the skin

Based on the theoretical framework described in sections 8.2.1-8.2.4, the most realistic and practical scenario of a laminate material on a rigid foundation is considered. In this case, the pressure is applied at the skin through a punch. In the coordinate system adopted in Fig. 8.1, rigid foundation is located at y=1, and punch is applied at y=-H (cf. Fig. 8.2).

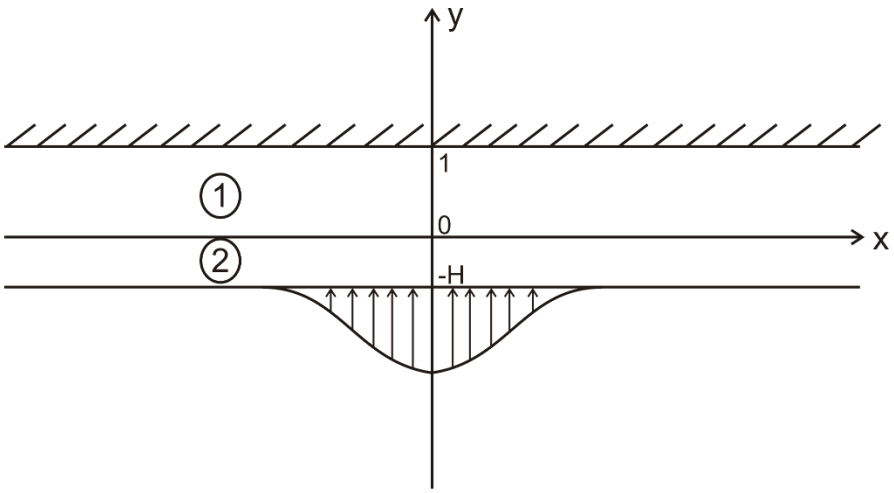

Fig. 8.2. Punching a two-layer system on a rigid foundation; material 1 is the core, material 2 is the skin. Note that this configuration can be flipped over, as in Fig. 8.1c, to have the punch and the skin on the top, which will be used in the presentation of the results in Figs. 8.3 and on for convenience.

In the present case the boundary conditions (8.4) are replaced by the following ones

$$y=1: \quad u_{x1}=0, \quad u_{y1}=0 \tag{8.66}$$

expressing the fact that layer 1 is boned to a rigid foundation. All the other boundary conditions stay unchanged.

Applying the boundary conditions (8.68) and using Eq. (8.14), in terms of the Goursat functions one finds that

$$(\kappa_1-1)\int \mathrm{Re}\,\Pi_1\big|_{y=1}dx-\int \mathrm{Re}\,\Omega_1\big|_{y=1}dx-2\,\mathrm{Im}\,\Pi_1\big|_{y=1}=0 \tag{8.67}$$

$$(\kappa_1+1)\int \mathrm{Im}\,\Pi_1\big|_{y=1}dx+\int \mathrm{Im}\,\Omega_1\big|_{y=1}dx-2\,\mathrm{Re}\,\Pi_1\big|_{y=1}=0 \tag{8.68}$$

where κ_1 corresponds to material 1 (the core).

Equations (8.12) and (8.13) yield

$$\mathrm{Re}\,\Pi=\frac{1}{4}(\sigma_{xx}+\sigma_{yy}) \tag{8.69}$$

$$\sigma_{yy}-\sigma_{xx}-2i\sigma_{xy}=2\overline{\Omega(z)}+2\left(z-\bar{z}\right)\overline{\Pi'(z)} \tag{8.70}$$

Therefore, from Eqs. (8.71) and (8.72) one finds

$$\mathrm{Re}\,\Pi_1\big|_{y=1}=\frac{1}{4}\left(\sigma_{xx1}\big|_{y=1}+\sigma_{yy1}\big|_{y=1}\right) \tag{8.71}$$

$$\mathrm{Re}\,\Omega_1\big|_{y=1}=\frac{1}{2}\left(\sigma_{yy1}-\sigma_{xx1}\right)\Big|_{y=1}-2\,\Pi_1'\big|_{y=1} \tag{8.72}$$

$$\mathrm{Im}\,\Omega\big|_{y=1}=\sigma_{xy1}\big|_{y=1}+2\,\mathrm{Re}\,\Pi_1'\big|_{y=1} \tag{8.75}$$

To find $\mathrm{Im}\,\Pi_1\big|_{y=1}$ in addition to the expressions (8.73)-(8.75), the Cauchy-Riemann condition (8.26) is employed, which takes the following form, accounting for Eq. (8.73)

$$\frac{\partial\,\mathrm{Im}\,\Pi_1\big|_{y=1}}{\partial x}=-\frac{\partial\,\mathrm{Re}\,\Pi_1}{\partial y}\bigg|_{y=1}=-\frac{1}{4}\left[\frac{\partial}{\partial y}\left(\sigma_{xx1}+\sigma_{yy1}\right)\right]\Big|_{y=1} \tag{8.76}$$

Substituting in the latter the expressions for the stresses from Eqs. (8.9) and (8.11) and integrating by x, one finds

$$\mathrm{Im}\,\Pi_1\big|_{y=1}=-\frac{1}{2}\int_0^\infty\left(C_{k1}k\sinh k+D_{k1}k\cosh k\right)E_{k1}\sin kx\,dk \tag{8.77}$$

Then, using the expressions for the stresses from Eqs. (8.9)-(8.11) in (8.73)-(8.75), the substitution of the resulting equations together with Eq. (8.77) into the boundary conditions (8.69) and (8.70) reduces them to the following form

$$\begin{aligned}&k\cosh k+A_{k1}k\sinh k+2C_{k1}\cosh k+C_{k1}k\sinh k+2D_{k1}\sinh k+D_{k1}k\cosh k\\&\quad-2\nu_1\left(C_{k1}\cosh k+D_{k1}\sinh k\right)=0\end{aligned} \tag{8.78}$$

$$\begin{aligned}&C_{k1}\sinh k+D_{k1}\cosh k-k\sinh k-A_{k1}k\cosh k-C_{k1}k\cosh k-D_{k1}k\sinh k\\&\quad-2\nu_1\left(C_{k1}\sinh k+D_{k1}\cosh k\right)=0\end{aligned} \tag{8.79}$$

The latter two equations replace Eqs. (8.43) and (8.44), respectively, while Eqs. (8.39)-(8.42) and (8.45)-(8.46) hold. Then, all the coefficients are found as before, i.e. Eqs. (8.47)-(8.53) hold, Eqs. (8.54) are replaced by

$$a_{21} = k\sinh k, \quad a_{22} = 2\cosh k + k\sinh k - 2\nu_1 \cosh k$$
$$a_{23} = 2\sinh k + k\cosh k - 2\nu_1 \sinh k, \quad b_2 = -k\cosh k \tag{8.80}$$

Equation (8.55) holds, while Eqs. (8.56) are replaced by

$$a_{31} = -k\cosh k, \quad a_{32} = \sinh k - k\cosh k - 2\nu_1 \sinh k$$
$$a_{33} = \cosh k - k\sinh k - 2\nu_1 \cosh k \tag{8.81}$$

Also, Eqs. (8.57)-(8.60) hold, while Eq. (8.61) is replaced by

$$E_{k1} = \frac{P}{\alpha\sqrt{\pi}} \exp\left[-k^2/\left(4\alpha^2\right)\right] \frac{1}{\left(m_5 A_{k1} + m_6 C_{k1} + m_7 D_{k1} + m_8\right)} \tag{8.82}$$

with

$$m_5 = -\left(k^2 + m_2 k\right)\sinh kH + k^2 m_2 H\cosh kH, \quad m_6 = k^2 m_1 H\sinh kH,$$
$$m_7 = -\left(1 - m_3\right)k\sinh kH - k^2 m_3 H\cosh kH, \quad m_8 = k^2\cosh kH + k^2 m_2 H\sinh kH \tag{8.83}$$

Equation (8.62) holds. Thus, all eight constants of integration are found, and the stress fields in both domains, as before, are calculated from Eqs. (8.9)-(8.11). Also, the displacements of material elements located at the interface between the skin and the core in the plane strain case are calculated from Eqs. (8.29) and (8.30).

The results of the solution of the punch problem for the punched laminate material located on a rigid foundation are depicted in Fig. 8.3. For convenience the coordinate Y=-y is introduced in plotting all the results in Fig. 8.3 and the following results, which means that in these figures the skin is located above the core and pressed from above. Accordingly, the shear stress σ_{xY}= -σ_{xy}, whereas σ_{YY}=σ_{yy}. In addition, u_Y=-u_y. Note also, that all stresses are rendered dimensionless by P.

Fig. 8.3a shows that the material is squeezed along the x-axis from under the punch, and compressed horizontally, since σ_{xx}<0. Fig. 8.3b shows the location of a significant shear stress σ_{xy}. Fig. 8.3c shows that the zone of the compressive stress in the normal direction under the punch becomes wider closer to the rigid foundation. Fig. 8.3d shows the field of the principal stress difference σ_1-σ_2 including the paper domain, where it is the largest. Because of the

smaller thickness of the skin in comparison to the core, the principal stress difference σ_1-σ_2 in the skin domain is difficult to visualize. Moreover, the interest is in determining the effect of the skin on the core. Therefore, for convenience, in Fig. 8.3e the values of σ_1-σ_2 in the skin domain are replaced by zero, and the distribution in the core is clearly visible. The horizontal displacement along the interface between core and skin is depicted in Fig. 8.3f.

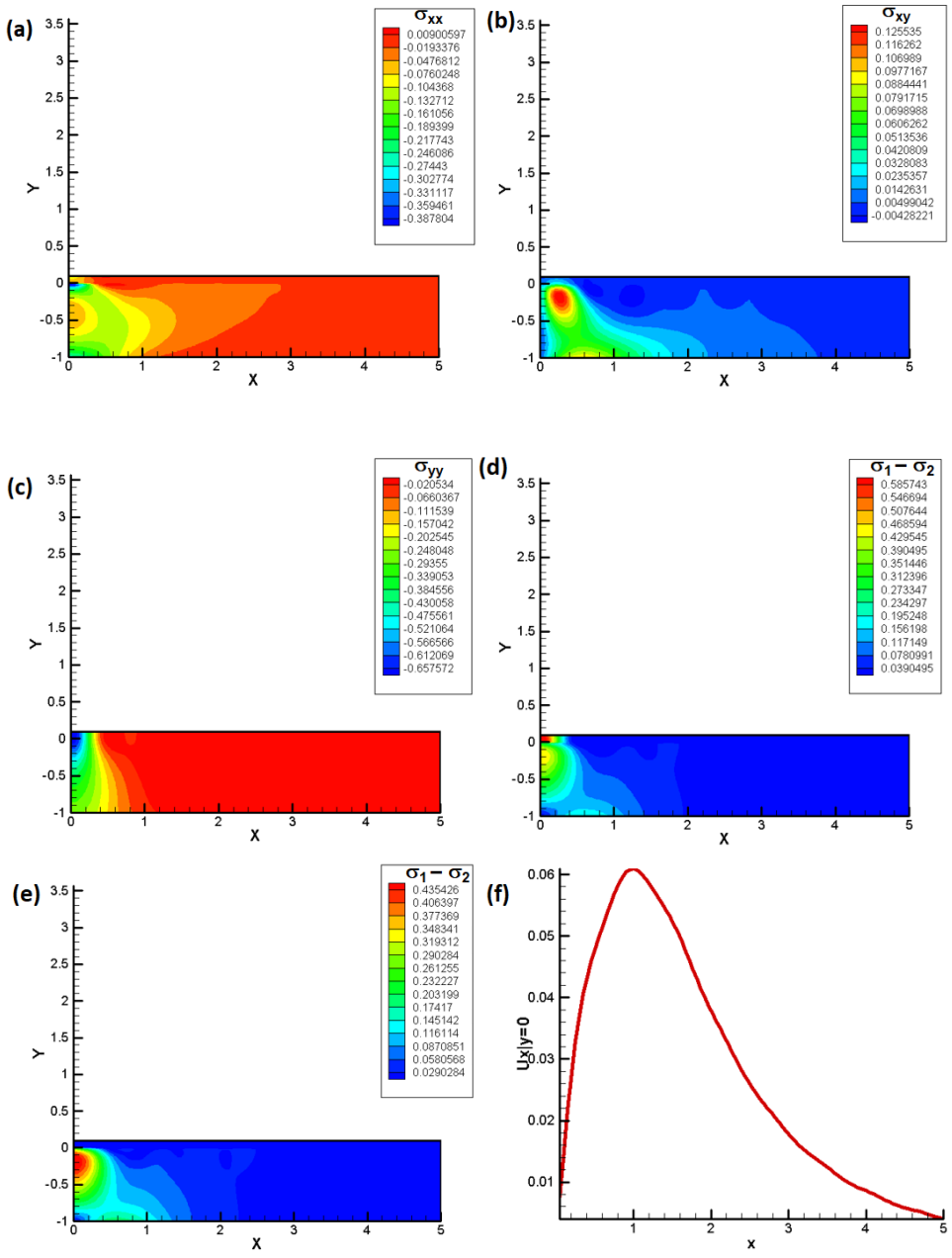

Fig. 8.3. A skin layer on top of a core, which is located on a rigid foundation (in the images the rigid foundation is at Y=-1). E_1=1, E_2=0.001, ν_1=0.5, ν_2=0.1, H=0.1 and P=1 (the plane strain case). (a) The field of σ_{xx}. (b) The field of σ_{xY}. (c) The field of σ_{YY}. (d) The field of the principal stresses difference σ_1- σ_2 in the skin and core of the laminate composite. (e) The field of the principal stresses difference σ_1- σ_2 in the core alone. (f) The horizontal component of the displacement (u_x) along the interface. In all these simulation, the value of α was chosen to be equal to 5.

The detailed solution given above corresponded to the plane strain case where the strain $\varepsilon_{zz}=0$. The plain stress case where the stress $\sigma_{zz}=0$ is also of interest, especially in relation to the experiments considered in the section 8.3. It should be emphasized that the distinction between the two cases stems from Eq. (8.14) where $\kappa = 3-4\nu_{\text{plane strain}}$ for the plane strain case and $\kappa = \left(3-\nu_{\text{plane stress}}\right)/\left(1+\nu_{\text{plane stress}}\right)$ for the plane stress case. Equations (8.22)-(8.83) were written for the plane strain case, and Poisson's ratio standing there is understood as $\nu_{\text{plane strain}}$. On the other hand, in the plane stress case the same formulae are applicable, however, $\nu_{\text{plane strain}}$ should be substituted by $\nu_{\text{plane stress}}/\left(1+\nu_{\text{plane stress}}\right)$. Then, in the plane stress case ν in Eqs. (8.22)-(8.83) can vary in the range $0 \le \nu \le 1/3$ when $0 \le \nu_{\text{plane stress}} \le 1/2$.

Above a certain threshold, the punched laminate composite fails in spite of the protection provided by the upper skin layer. Different failure criteria have been proposed in the past (Yarin et al. 2019), albeit majority of them would not be appropriate in the case of simultaneous multiple cracks arising in a certain domain in the core under the punch. Therefore, it is extremely useful to introduce a failure criterion based on the elastic energy stored per unit volume of the core $U_{\text{elastic,core}}$ (see, for example, Qu et al. 2016). In general the elastic energy per unit volume $U_{\text{elastic}} = \boldsymbol{\sigma}:\boldsymbol{\varepsilon}/2$ (Landau & Lifshitz 1970), with $\boldsymbol{\sigma}$ being the stress tensor and $\boldsymbol{\varepsilon}$ being the strain tensor. Accordingly, in the plane stress case ($\sigma_{zz}=\sigma_{zx}=\sigma_{zy}=0$)

$$U_{\text{elastic core}} = \frac{1}{2E_1}\left[\sigma_{xx}^2+\sigma_{yy}^2-2\nu_1\sigma_{xx}\sigma_{yy}+2\sigma_{xy}^2\left(1+\nu_1\right)\right] \tag{8.84}$$

where Poisson's ratio ν_1 is understood as $\nu_{\text{plane stress},1}$.

In that regard, it is extremely instructive to elucidate the effect of the skin elastic modulus and Poisson's ratio on the elastic energy density in the core. To elucidate that, two separate cases were considered. First, elastic modulus of both the core and the skin was kept constant;

also the Poisson's ratio of the core was kept constant, and only Poisson's ratio of the skin was varied. The corresponding results are shown in Fig. 8.4, where $E_1 = E_2 = 1$ (these dimensionless values should be understood as being normalized by the core Young's modulus) and $\nu_{\text{plane stress},1} = 0.35$, whereas different values of $\nu_{\text{plane stress},2} =$ 0.1, 0.2, 0.3 and 1/2 were used (cf. Fig 8.4a-d, respectively). In the second case, Poisson's ratio of both the core and the skin were kept constant; also the elastic modulus of the core was kept constant, whereas the elastic modulus of the skin was varied. The corresponding results are shown in Fig. 8.5, where $\nu_{\text{plane stress},1} = 0.35$, $\nu_{\text{plane stress},2} = 0.1$; E_1=1 and different values of E_2 = 0.01, 0.1, 1 and 2 (these dimensionless values should be understood as being normalized by the core Young's modulus) were used (cf. Fig 4a-d, respectively). In Figs. 8.4 and 8.5 the distribution of the dimensionless elastic energy is shown. In all the cases, the cutoff value for high elastic energy was chosen as 0.2, and the dimensionless areas in the core corresponding to $U_{\text{elastic core}} > 0.2$, i.e. to the core failure, are encompassed by black lines. Also, all the panels in Figs. 8.4 and 8.5, show the magnitudes of the compressive stress $\sigma_{YY,}$ i.e., $\left|\sigma_{YY}\right|_{x=0,\, Y=-0.4}\Big|$, at the point x=0 and Y=-0.4, where the measurements discussed in section 8.3 were done.

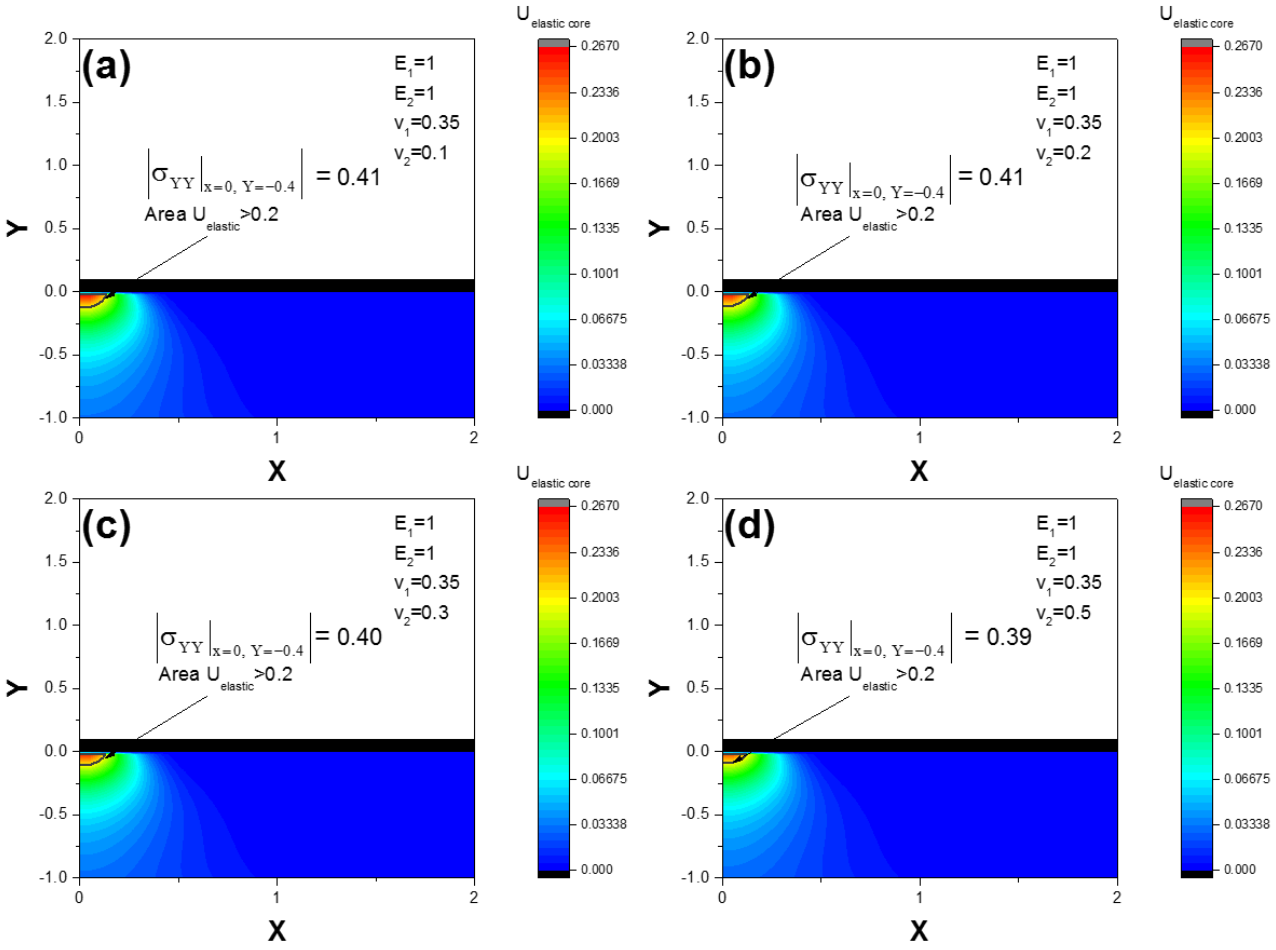

Fig. 8.4. Elastic energy per unit density in the core for varying Poisson's ratio of the skin. Here $E_1 = E_2 = 1$ and $\nu_{\text{plane stress},1} = 0.35$, and (a) $\nu_{\text{plane stress},2} = 0.1$, the area where $U_{elastic}$ is greater than 0.2 is equal to 1; (b) $\nu_{\text{plane stress},2} = 0.2$, the area where $U_{elastic}$ is greater than 0.2 is equal to 0.81; (c) $\nu_{\text{plane stress},2} = 0.3$, the area where $U_{elastic}$ is greater than 0.2 is equal to 0.81; and (d) $\nu_{\text{plane stress},2} = 1/2$, the area where $U_{elastic}$ is greater than 0.2 is equal to 0.63. The elastic energy was rendered dimensionless by the applied stress magnitude P^2/E_1 (with $P = E_1 = 1$).

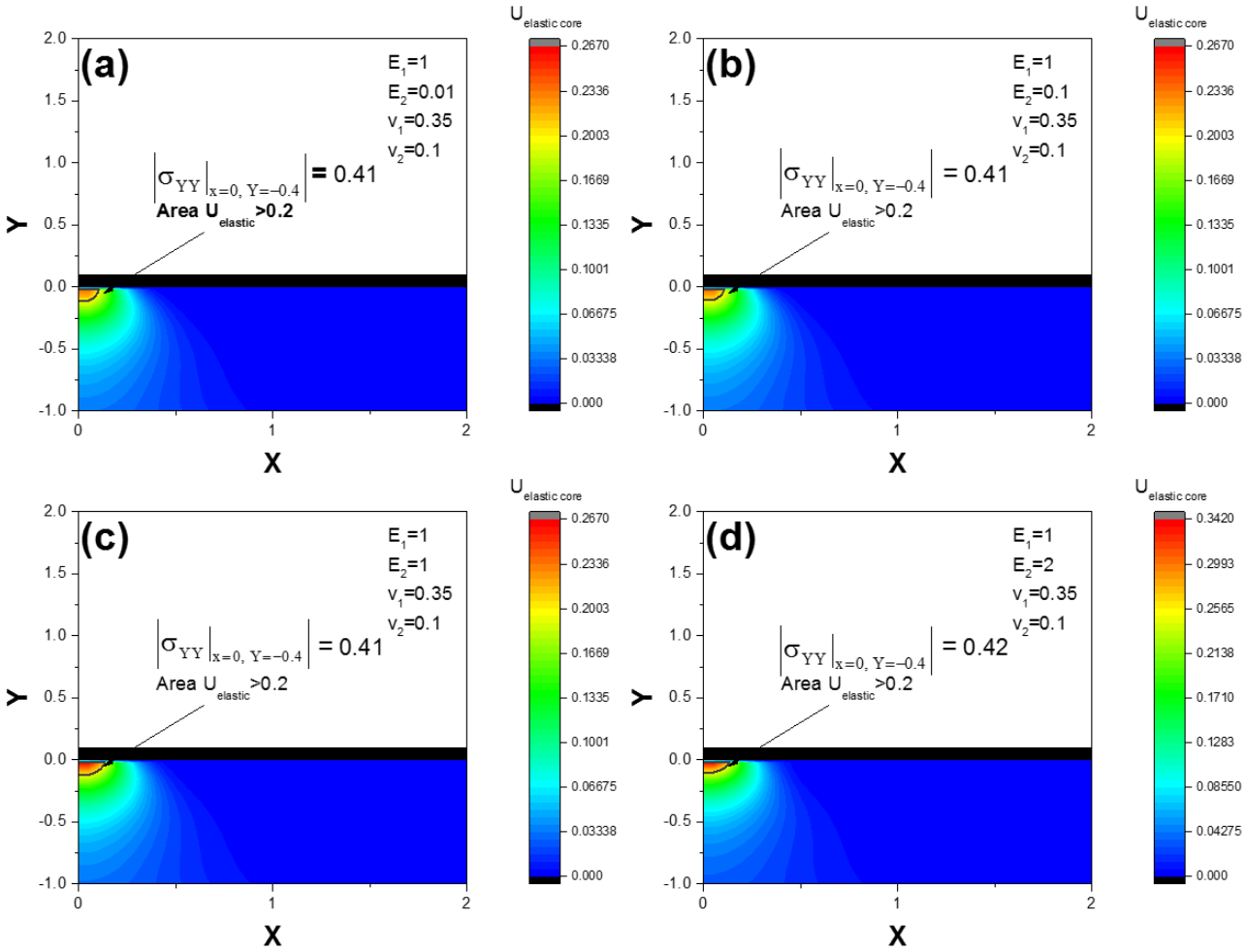

Fig. 8.5. Elastic energy per unit density in the core for varying Young's modulus of the skin. Here $\nu_{\text{plane stress},1} = 0.35$, $\nu_{\text{plane stress},2} = 0.1$, E_1= 1 and and (a) E_2= 0.01, the area where $U_{elastic}$ is greater than 0.2 is equal to 1; (b) E_2= 0.1, the area where $U_{elastic}$ is greater than 0.2 is equal to 1; (c) E_2= 1 the area where $U_{elastic}$ is greater than 0.2 is equal to 1.45; and (d) E_2= 2, the area where $U_{elastic}$ is greater than 0.2 is equal to 2.5. The elastic energy was rendered dimensionless by the applied stress magnitude P^2/E_1 (with P= E_1=1).

Fig. 8.4 shows that as the value of Poisson's ratio ν_2 increases from 0.1 to 1/2, the failure zone in the core decreases. Fig. 8.5 shows that reduction of elastic modulus of the skin results reduces the failure zone in the core. However, from Fig. 8.5a-c it is seen that the failure zone reduction saturates at the lower values of E_2. Moreover, reduction of the skin Young's modulus

would hardly be practically possible, whereas modification of the skin Poisson's ratio are practical.

Another parameter of high interest is the value of stress the compressive stress along the central line x=0 in the core at the vertical location Y= -0.4. This location was used to measure the compressive stress in the experimental section 8.3. It should be emphasized that at x=0 due to Eq. (8.10) σ_{xy}=0. Then, Eqs. (8.63) and (8.64) yield

$$\sigma_{yy}\Big|_{x=0} = \frac{(\sigma_1 - \sigma_2)\Big|_{x=0} + (\sigma_1 + \sigma_2)\Big|_{x=0}}{2} \tag{8.85}$$

8.3. Experimental

In order to elucidate the effects predicted by the theory, two non-destructive and non-intrusive experimental setups are developed to measure stresses occuring inside the core owing to different skin materials. Two different set ups were used with the respective setup schematics shown in Figs. 8.6 and 8.8a. In both setups paper samples were used as skin (paper) materials which possess different thicknesses, basis weights and number of plies. In every experiment a sample of paper was bonded to a polycarbonate substrate using spirit gum, with polycarbonate being used as the core material. The thickness of the polycarbonate substrate is 9.5 mm**,** whereas the thickness of the papers used were ~ 0.26-0.45 mm, i.e., the paper thickness was two orders of magnitude smaller than the thickness of the core, which closely mimics laminated sandwich structures. The paper attached to the polycarbonate was preloaded by the punch to 5 N. This was considered to be the reference point of starting the test. It was done to avoid ambiguity of the touch point. Then, the punch was pressing on the paper toward the substrate (polycarbonate supported on a rigid foundation) at the rate of 0.0068 cm/s. The rate was controlled by a microcontroller governing the punch movement (see Fig. 8.6). As a result, at

time t (measured in seconds), after the reference point had been passed, the total displacement of the punch could be accurately found as 0.0068t (in cm).

The load was applied through a force gauge uniformly over the central 3 mm - wide section of the paper. The punch has rectangular cross-section of 3 mm $\times$ 12 mm. The load was transmitted through the paper specimen to the polycarbonate substrate, in which the corresponding stress field was generated. The substrate reacted elastically under the conditions of the planar stress loading at the polycarbonate sides, i.e. $\sigma_{zz}=0$.

A Mark-10 series 3 gauge with a 1000 N load limit was used in the experiments. The internal strain gauge has an equivalent spring constant (K) of 3.937×10^4 N/cm. The force gauge has linear response to applied force up to 1000 N. During the experiment, both the load on the force gauge and the displacement were measured. From the reading of the force gauge F(t), the deformation of the strain gauge can be found. It should be emphasized that the displacement provided by the motor and the deformation of the strain gauge are different. Accordingly, the deformation of paper at time t from the reference point is $\Delta H(t) = 0.0068t - F(t)/K$. The polycarbonate deformation can be neglected because it is much stiffer than the spring and paper. Then, the strain of paper is found as $\Delta H(t)/ H$, where H is the original paper thickness. It should be emphasized that in the experiments the strains of 1 and above could be reached when paper was ultimately poked by the punch. Therefore, in the experimental results discussed below the data sets are truncated when strain reaches the values in the 0.55-0.7 range.

It should be emphasized that polycarbonate is only a tool in the present study, and does not affect the results pertaining to paper. Nevertheless, polycarbonate possesses the elastic modulus of 2.3 GPa, which is of the same order of magnitude as that of a standard core material. Specifically, gypsum wallboard which is a standard laminate material, has the core elastic modulus of ~0.4- 2 GPa (Cramera et al. 2003, Rahmanian 2011). On the other hand, the

polycarbonate substrate used in the present work was rather ductile, whereas the cores in typical laminates can range from ductile to brittle.

Note also that spirit gum was used for the following three reasons. (i) A spirit gum layer once dried has a very small thickness and ductility. This results in perfect contact between the paper and the polycarbonate substrate and minimizes losses at the interface. (ii) Once the experiment is finished, it is easy to remove spirit gum using ethanol without leaving any residue. This facilitated reuse of the specimens. (iii) Because of the low viscosity, it is easier to apply the glue layer with repeatable thickness from experiment to experiment. In addition to spirit gum, other glues were also used (e.g., acrylic glue, polyvinyl acetate, etc.). However, almost all the other glues either resulted in non-repeatable layers, and/or possessed higher ductility, and/or were difficult to remove from the substrate without leaving any residue.

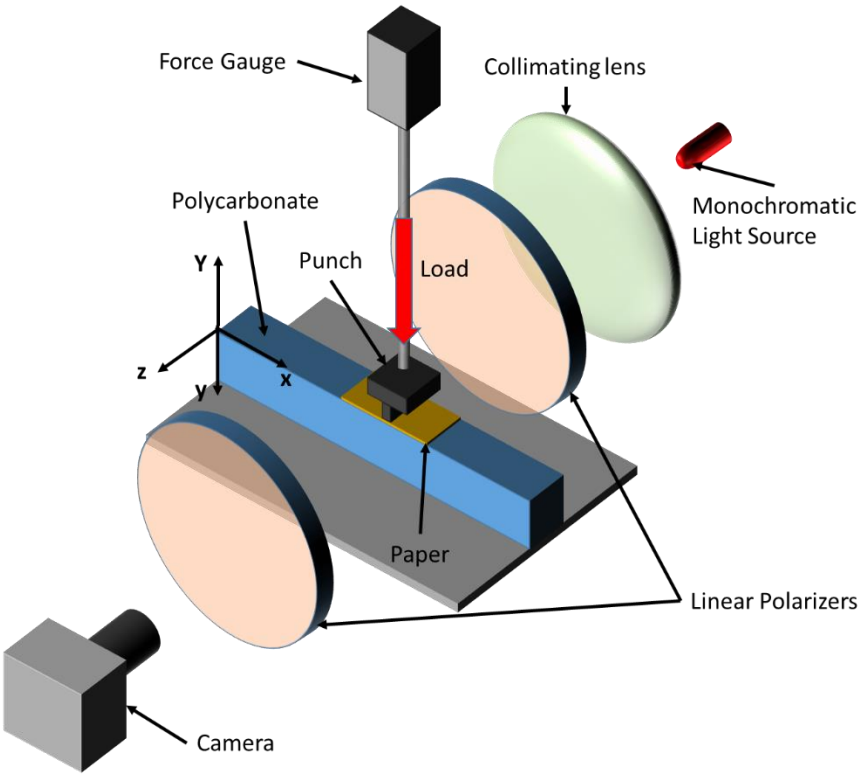

Fig 8.6. Experimental setup for measuring the principal stress difference.

In the first setup, the technique used to measure the principal stress difference is based on birefringence. This is based on the fact that polycarbonate is capable to split under load an incident light ray into two orthogonal components with different refraction indexes propagating in the directions of the principal stresses in the material. It should be emphasized that that is the main reason of using polycarbonate as a convenient substrate material in the present work, which has paper effect on the stress field in the substrate in focus. The field of birefringence shown in the image in Fig. 8.7a is used in setup 1 to directly observe the lines of constant principal stress difference (the black lines in the image). The stress-optic law reads

$$\sigma_1 - \sigma_2 = \frac{N\lambda}{c_\sigma H} \tag{8.86}$$

where N=0, 1, 2,… correspond to different black lines of constant principal stress difference, λ is the wavelength of light, c_σ is the photoelastic constant of the material (polycarbonate), and H is the specimen thickness (which is the same for polycarbonate and paper mounted on top of it). The sensitivity of this method is sufficient to differentiate between the effect of different paper specimens, and the experimental results can be used for comparison of the overall structure of the predicted and measured fields of the principal stress difference (Figs. 8.7a and 8.7b, respectively).

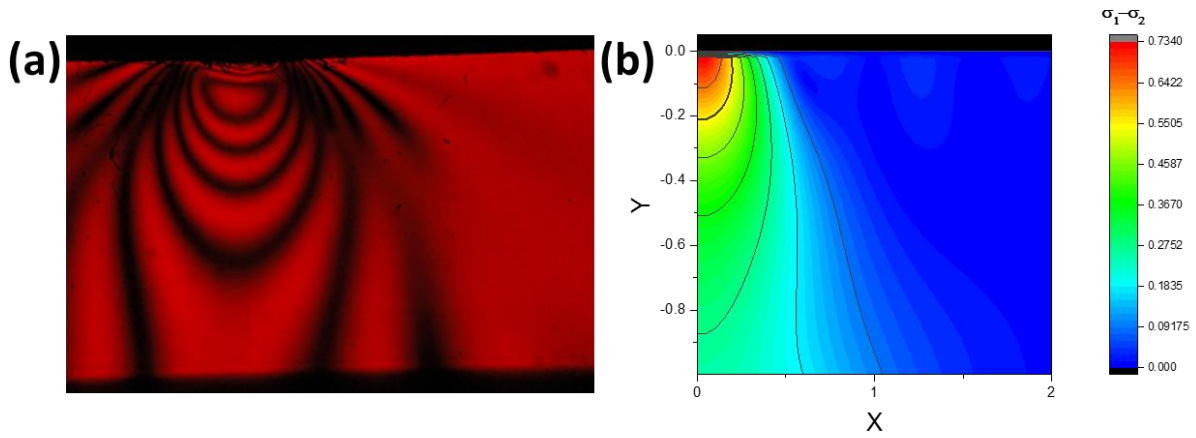

Fig. 8.7. Principal stress difference in the core material (polycarbonate). (a) Experimental observation with red light (λ=650 nm). (b) Theoretical prediction of the right-hand side half of the field (due to the symmetry) using Eq. (8.63).

In the second experimental setup (cf. Fig. 8.8), the elastic bulging of the polycarbonate substrate (in the z-direction in the plane stress case with $\sigma_{zz} = 0$) under load was used to measure the principal stress sum. Because of the applied load the polycarbonate substrate bulges sideway, and the out-of-plane strain ε_{zz} for the plane stress case is related to the sum of the principal stresses $\left(\sigma_{xx} + \sigma_{yy}\right)$ as

$$\varepsilon_{zz} = \frac{-\nu_{pol}}{E_{pol}}\left(\sigma_{xx} + \sigma_{yy}\right) \tag{8.87}$$

where E_{pol} and ν_{pol} are the Young's modulus and Poisson's ratio of polycarbonate [E_{pol} =2.3 GPa and ν_{pol} =0.37 as provided by the manufacturer; (http://www.goodfellow.com/E/Polycarbonate.html)]. It should be emphasized that the Young's moduli and Poisson's ratios of paper specimens are denoted below by E and ν.

The second setup depicted in Fig. 8.8a is capable of measuring the out-of-plane strain ε_{zz}, and thus the principal stresses $\left(\sigma_{xx} + \sigma_{yy}\right)$ via Eq. (8.87). The bulging out-of-plain strain is

measured by means of an optical flat (cf. Fig. 8.8a). An ¼ λ optical flat (i.e., the flatness of this plate is within ¼ of the wavelength of light) was carefully placed at the polycarbonate side so that the bulging resulting from pre-loading is clearly visible as the fringe pattern recorded in Fig. 8.8b (λ=650 nm is the wavelength of red light used which was isolated during data processing). The fringe pattern at the polycarbonate side was recorded by a Phantom "Miro 311" high-speed video camera at 60 fps. The fringe pattern was then used to extract the principal stress sum $\left(\sigma_{xx}+\sigma_{yy}\right)$ acting in the polycarbonate loaded through the paper sample attached at its surface using an in-house Matlab code. Additional details on the stress measurement are provided in the Supplementary Information.

The principal stress was measured at the positions 4 mm below the polycarbonate surface (cf. Fig. 8.8b). This is equivalent to Y= -0.4 in the dimensionless form in Figs. 8.4 and 8.5. At the continuation of the punch axis σ_{xx} =0 due to the symmetry, which allows one to determine $\sigma_{yy}\big|_{x=0}$ inside the polycarbonate substrate using Eq. (8.87). Simultaneously, the load applied to the paper specimen is measured by the force gauge (cf. Fig. 8.8a) as a function of time and used to determine the stress σ_{yy} acting at the paper surface. A preliminary test revealed that paper possesses a long-term creep under load which is shown in Fig. B2 in Appendix B . This observation implies that a loaded paper continuously deforms under load redistributing the stress transmitted to the underlying polycarbonate specimen over a larger area as shown schematically in Fig. 8.9a. However, the process time of the nail pull is on the order of 10 s, while the longest creep time of paper is on the order of minutes. In order to demonstrate the ability of different types of paper to redistribute load in the nail-pull-like processes, the normal stress inside the polycarbonate is measured at the instant the load on the force gauge (load at the paper surface) reached 300 N. This procedure is applied to all different types of paper studied in this work. A representative dependence of $\sigma_{yy}\big|_{x=0,\,Y=-4\text{ mm}}$ recorded by the load cell

during the punch movement versus the strain ε_{yy} experienced by paper layer is shown in Fig. 8.8c.

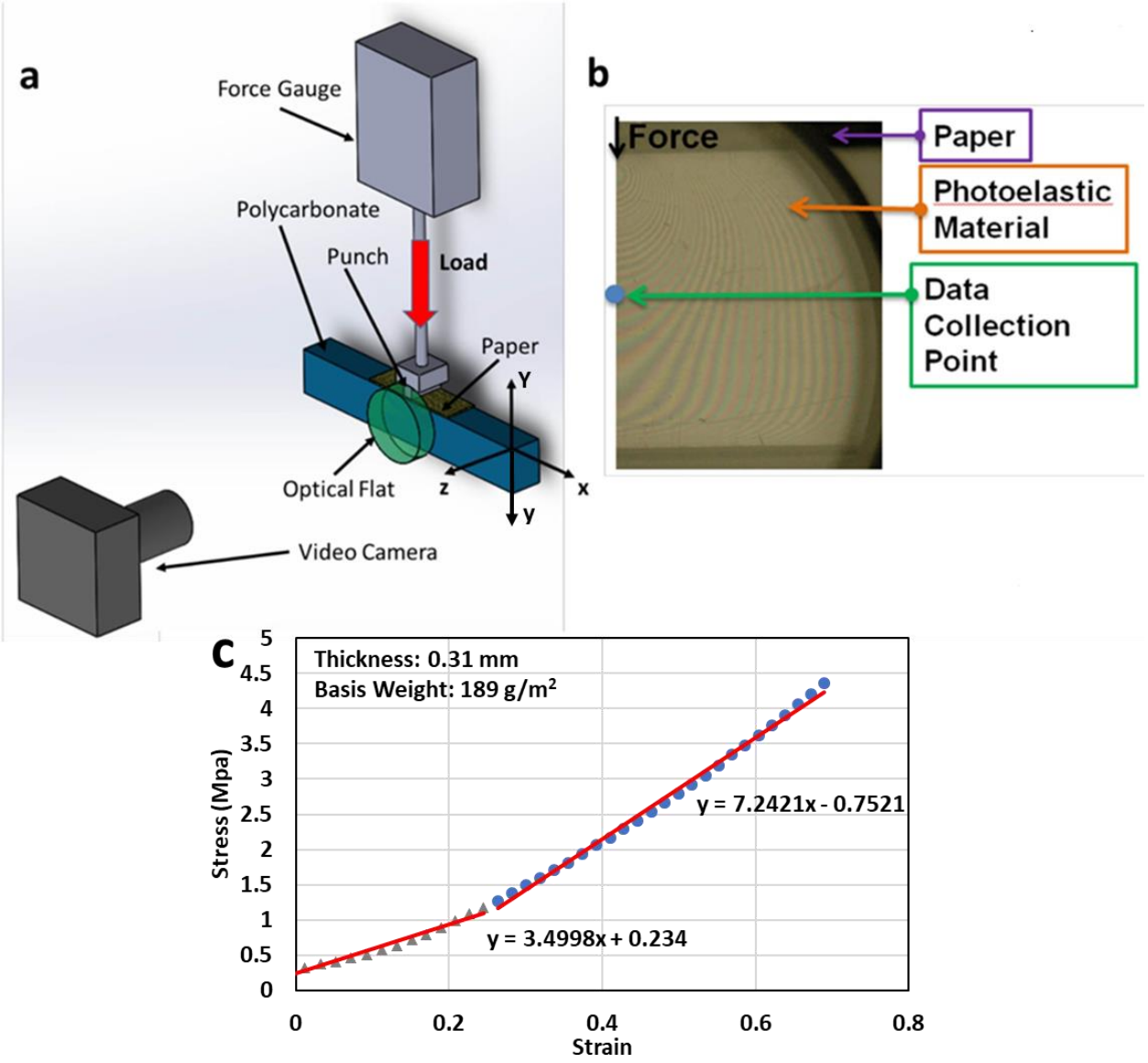

Fig. 8.8. (a) Schematic of the second experimental setup for measuring stress $\sigma_{yy}\big|_{x=0,\,Y=-4\text{ mm}}$ generated inside the polycarbonate core during loading. (b) Fringe pattern observed at the polycarbonate side due to the load transmitted through the bonded paper specimen. (c) Representative plot of stress $\sigma_{yy}\big|_{x=0,\,Y=-4\text{ mm}}$ versus strain ε_{yy} experienced by paper layer.

8.4. Experimental Results & Discussion

8.4.1. Micromechanics of paper behavior under load

Fig. 8c shows that the stress-strain relationship depicted there is nonlinear. It can be approximated as a crossover of two separate straight lines with very different slopes. Such a behavior can be interpreted using a simplified 2D model of paper (Fig. 8.9). Paper is a composite material consisting of interwoven filaments which as represented by loosely packed cylinders seen in the cross-sections in the 2D model in Fig.8. 9a. As the load is applied to the paper surface, the filaments begin to rearrange, i.e. to repack into a more compact form. Eventually the cylinders reach a fully packed state (Fig. 8.9b) which results in a sharp increase in resistance to further loading. However, the further loading continues to squeeze the paper filaments from under the punch (Fig. 8.9c). Accordingly, the stress-strain dependence in Fig. 8.8c shows that paper under the punch reveals two distinct domains: (i) the repacking domain with a lower slope, similar to Fig. 8.9a, and (ii) the packed-squeezing domain with a higher slope, similar to Fig. 8.9c. A detailed description of these two domains is given in sub-sections 8.4.1.1 and 8.4.1.2, respectively.

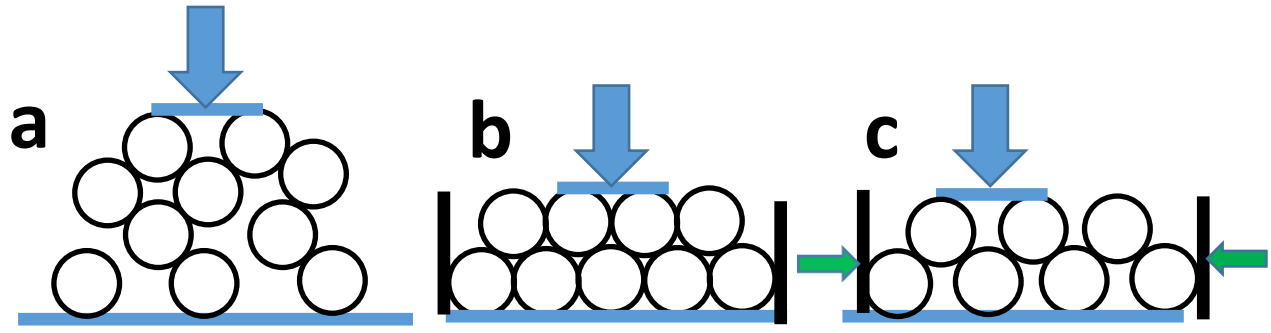

Fig. 8.9. 2D model of paper cross-section under load.

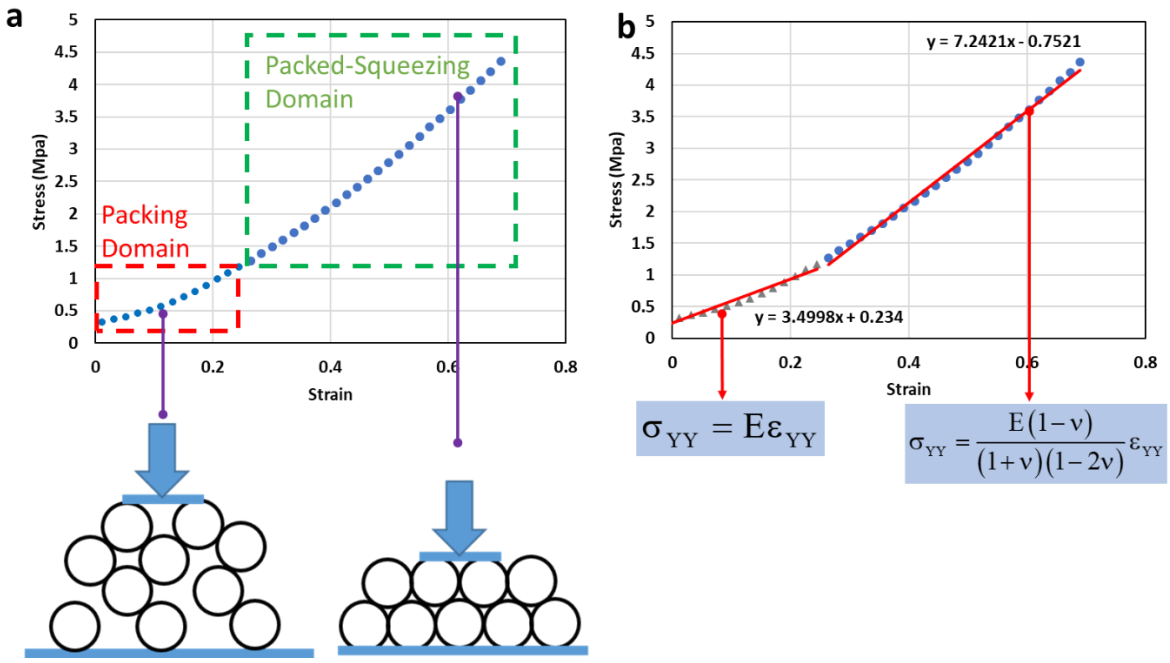

Fig. 8.10. (a) Two domains in the load-displacement dependence corresponding to the schematics in Fig. 8.9. (b) The stress-strain dependences corresponding to both domains.

8.4.1.1. The repacking domain

The linear stress-strain dependence corresponding to the repacking domain in Fig. 8.8c suggests a linearly elastic behavior of paper following Hooke's law (Landau & Lifshitz 1970)

$$\boldsymbol{\sigma} = \frac{E}{1+\nu}\boldsymbol{\varepsilon} + \mathbf{I}\frac{E\nu}{(1+\nu)(1-2\nu)}\mathrm{div}\mathbf{u} \qquad (8.88)$$

with $\boldsymbol{\sigma}$ being the stress tensor, $\boldsymbol{\varepsilon}$ = (1/2) $[\nabla\mathbf{u}+\nabla\mathbf{u}^{T}]$ being the strain tensor, $\mathbf{u}$ being the displacement vector, E being Young's modulus and ν being Poisson's ratio (of paper, in the preset case). Note that the strain in the present experiment is linearly increasing in time.

Denote the punch direction, which is normal to the paper sheet, as the Cartesian axis Y, while the two other Cartesian axes x and z being in the paper plane. Only the lower surface of paper specimen is bonded to a hard elastic foundation (the polycarbonate slab), while most of the paper bulk is practically unrestricted over its perimeter, which (together with the equations

of mechanical equilibrium) means that the stresses $\sigma_{xx}=\sigma_{zz}=0$ practically everywhere in the paper. Moreover, the paper bulk, being practically unrestricted, experiences a practically axisymmetric deformation due to punching, which means that $\varepsilon_{xx}=\varepsilon_{zz}$.

Equation (8.88) yields

$$\sigma_{xx}=\frac{E}{(1+\nu)(1-2\nu)}\left[(1-\nu)\varepsilon_{xx}+\nu\left(\varepsilon_{YY}+\varepsilon_{zz}\right)\right] \tag{8.89}$$

In the compression process under consideration, where $\sigma_{xx}=0$ and $\varepsilon_{xx}=\varepsilon_{zz}$, Eq. (8.89) yields

$$\varepsilon_{zz}=-\nu\varepsilon_{YY} \tag{8.90}$$

On the other hand, Eq. (8.88) yields the stress in the compression direction σ_{YY} as

$$\sigma_{YY}=\frac{E}{(1+\nu)(1-2\nu)}\left[(1-\nu)\varepsilon_{YY}+\nu\left(\varepsilon_{xx}+\varepsilon_{zz}\right)\right] \tag{8.91}$$

In the process under consideration (with $\varepsilon_{xx}=\varepsilon_{zz}$), Eqs. (8.90) and (8.91) reveal that irrespective of the value of Poisson's ratio,

$$\sigma_{YY}=E\varepsilon_{YY} \tag{8.92}$$

which corresponds to repacking domain in Fig. 8.10. Therefore, Young's modulus in compression normal to the paper specimen can be determined from the slope of the stress-strain dependence corresponding to the repacking domain in Fig. 8.10b.

8.4.1.2. The packed-squeezing domain

The linear stress-strain dependence corresponding to the packed-squeezing domain in Fig. 8.8c still suggests a linearly elastic behavior of paper following Hooke's law (8.88). However, here the lower part of the paper specimen is essentially packed as a filament monolayer bonded to a hard elastic substrate (cf. Fig. 8.9c). Such a dense paper layer reacts to punching elastically but different from the repacking domain. Indeed, because filaments are

essentially bonded to the hard substrate, in the packed-squeezing domain $\varepsilon_{xx} = \varepsilon_{zz} = 0$, while due to the axial symmetry, $\sigma_{xx} = \sigma_{zz}$. According to Hooke's law (8.88),

$$\varepsilon_{xx} = \frac{1}{E}\left[\sigma_{xx} - \nu\left(\sigma_{YY} + \sigma_{zz}\right)\right] \tag{8.93}$$

Therefore, (since $\varepsilon_{xx} = 0$ and $\sigma_{xx} = \sigma_{zz}$) Eq. (8.93) yields

$$\sigma_{XX} = \frac{\nu}{1-\nu}\sigma_{ZZ} \tag{8.94}$$

On the other hand, $\sigma_{xx} = \sigma_{zz}$ also yields

$$\varepsilon_{YY} = \frac{1}{E}\left[\sigma_{YY} - \nu\left(\sigma_{xx} + \sigma_{zz}\right)\right] \tag{8.95}$$

Using the fact that $\sigma_{xx} = \sigma_{zz}$ and Eq. (8.94), one obtains from Eq. (8.95) that

$$\sigma_{YY} = \frac{E(1-\nu)}{(1+\nu)(1-2\nu)}\varepsilon_{YY} \tag{8.96}$$

Equation (8.96) determines the paper behavior in the packed-squeezing domain, in particular, the slope of the stress-strain dependence corresponding to this domain in Fig. 8.10b. This means that Poisson's ratio of paper ν can be found from the slope of the stress-strain dependence in the packed-squeezing domain (Fig. 8.10b). Moreover, comparing Eqs. (8.92) and (8.96) note that the slope of the stress-strain dependence at the packed-squeezing stage is always steeper than at the repacking stage (cf. Fig. 8.10b), because

$$\frac{(1-\nu)}{(1+\nu)(1-2\nu)} > 1 \tag{8.97}$$

for any value of ν.

The predicted theoretically fact that the slope of the stress-strain dependence in the packed-squeezing domain is always steeper than the one in the repacking domain is confirmed by the experimental results for several types of paper discussed in the section 8.4.2.

It should be emphasized that the linear theory of elasticity can be used as much as the material behavior is linear, either spatially (but piecewise, as in section 8.2), or temporary (but

piecewise in time, or bilinearly, as here). The piecewise behavior in time is associated to a practically stepwise change in the fiber packing inside, from the incomplete packing, to the complete packing (see Fig. 8.10). As any continuum theory, the theory of elasticity does not consider the detailed micromechanics of a material. If at any internal structure, the material follows Hooke's law, the theory of elasticity could be applied. A fruitful analogy would be a vapor, which underwent full condensation. Both before the condensation and after it, the material can be considered as a Newtonian viscous fluid, albeit of different density and viscosity, even though both vapor and liquid are comprised of the same molecules. Similarly in the present case, different density and the effective Young's modulus arise from fiber repacking in the paper, even though in both states paper is comprised of the same fibers.

8.4.2. Comparison of the experimental data with theoretical predictions

8.4.2.1. Comparison of the data with the theory and measurement of Young's modulus and Poisson's ratio

The results of the dynamic-loading tests were converted into stress-strain curves. To do that, the stress was calculated as the load divided by the punch area of 36.9 mm^2, and the strain found as the punch displacement divided by the original paper thickness. The resultant stress-strain curves are shown in Fig. 8.11 where only 4 representative paper types of different thicknesses and basis weights per unit area, are presented of the data acquired for multiple paper types. Figures 8.11a-8.11d show the results for the paper thicknesses of 0.26, 0.31, 0.36, and 0.42 mm with basis weights of 165, 189, 229, 254 g/m^2, respectively. It should be emphasized that the papers used were formed differently and possessed a different number of plies.

As in Fig. 8.10b, all the stress-strain curves can be subdivided into two domains representing a crossover of two straight lines. In the two domains these two lines reveal two

distinct slopes (cf. Fig. 8.11). The slope of the line corresponding to the lower stresses is used to find the value of the corresponding Young's modulus E, according to Eq. (8.92). Then, the slope of the line corresponding to the higher stresses is used to find the value of the ratio $E(1-\nu)/\left[(1+\nu)(1-2\nu)\right]$ according to Eq. (8.96). Because the value of E is already established, the value of this ratio yields Poisson's ratio ν.

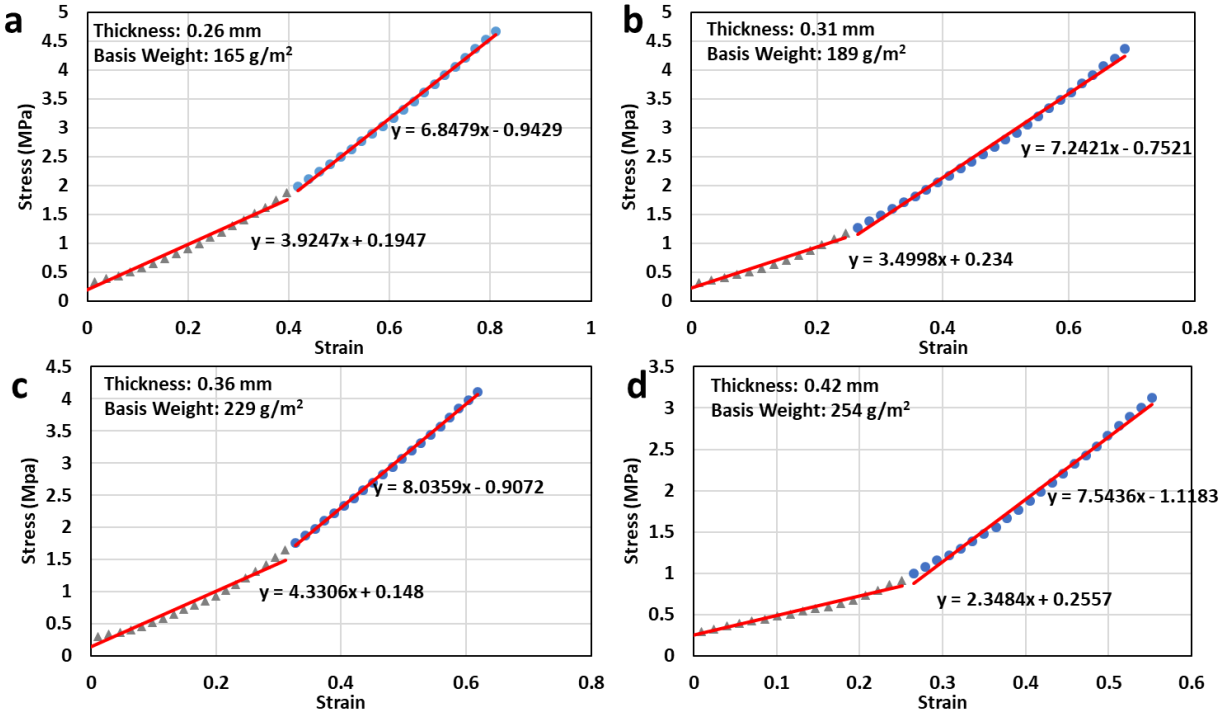

Fig. 8.11. Stress-strain curves for the following types of paper: (a) Paper A with the thickness of 0.26 mm, (b) Paper B with the thickness of 0.31 mm, (c) Paper C with the thickness of 0.36 mm, (d) Paper D with the thickness of 0.42 mm. The data is shown by blue symbols, the corresponding fitting lines in both domains – by straight red lines.

It should be emphasized that the second branch in the stress-strain curves in Figs. 8.8, 8.10 and 8.11 reaches the strain values in the 0.55-0.7 range being still linear. This is characteristic of multiple hyperelastic materials (Lurie 2005), in particular the fibrous ones (similar to papers; Khansari et al. 2012, Yarin et al. 2014), which allows one to approximate them using Hooke's law in the first approximation.

8.4.2.2. The compressive stress in the core material underlying paper.

Poisson's ratio ν and Young's modulus E measured in sub-section 8.4.2.1 are plotted in Figs. 8.12a and 8.12b, respectively, versus the corresponding stress magnitudes $\left|\sigma_{YY}\right|_{x=0,\ Y=-4\,mm}$ measured using the second experimental setup depicted in Fig. 8.8a in section 8.3. Fig. 8.12a reveals that as Poisson's ratio of papers increases, the stress magnitude $\left|\sigma_{YY}\right|_{x=0,\ Y=-4\,mm}$ decreases. This means that as paper becomes less compressible (an increase in ν) the magnitude of the compressive stress in the core material underneath decreases. The less compressible paper tends to stretch sideways more under punch, thus redistributing stresses in the core, and diminishing the most dangerous compressive component primarily responsible for failure.

On the other hand, Fig. 8.12b does not reveal any clear correlation between the Young's modulus of paper E and the magnitude of the compressive stress, which implies that the value of the elastic modulus of paper is immaterial for protection of the underlying core material against compressive failure.

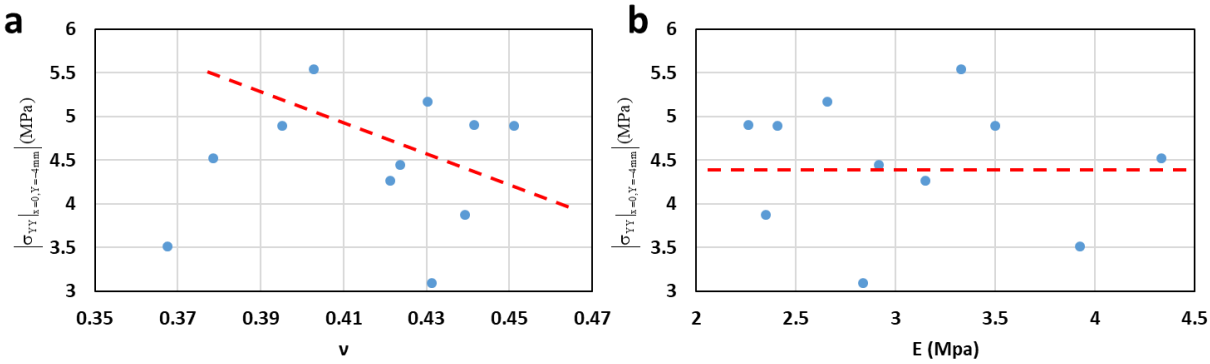

Fig. 8.12. Dependence of σ_{yy} on (a) Poisson's ratio and (b) elastic modulus is shown.

Note that a higher number of plies in a paper can result in a poor contact between plies and thus, a slip between plies and poor stress redistribution. However, the focus of the present work is not in the elucidation of the micromechanical characteristics of the paper, but rather in determining the effect of paper on stress redistribution inside the core. The ply-to-ply interaction manifests itself in the values of the elastic parameters of the paper (cf. Fig. 8.12), with one of them, Poisson's ratio, being important for the stress redistribution inside the core. Additionally, the physical properties of the plies in a paper were identical, which validates the uniformity assumption in the direction of compression.

8.5. Conclusion

The theoretical and experimental results of the present work explain and describe the mechanics of protection of the core material by the protective outer paper layer in punched laminate composites. Specifically, the micromechanics of paper behavior in compression reveals two distinct domains. In the first repacking domain corresponding to low stresses and strains the initial relatively loose network of filaments which comprise paper is compacted. In the second packed-squeezing domain, the compacted filament structure is squeezed aside from under the punch, thus redistributing the compressive stresses and protecting the core material. Novel methods developed in this work allow measurement of Young's modulus and Poisson's ratio of paper. The results showed that the higher is Poisson's ratio of paper, i.e. the less is its compressibility, the lower is the compressive stress magnitude in the core material underneath. That means that the less compressible paper provides a better protection to the core material because such paper has a higher propensity to spread aside under the punch, and thus to redistribute the dangerous compressive stresses. On the other hand, the Young's modulus of the paper plays practically no role in the protection of the underlying core material.

Note also that because of different imperfections of the formation process, in principle, paper can be non-uniform in all three directions. This would result in a non-uniform contact pattern between pulp fibers, in distinction from the micromechanical model. Still, the model captures the general physical trends of the fiber-fiber interaction, and thus, correctly elucidates the effect of Poisson's ratio.

It should be emphasized that the estimates of the load redistribution effect in the framework of the planar problem of the theory of elasticity provided in the present work underestimate this positive effect (cf. Yarin et al. 2017), which holds great promise for practical applications.

9. CONCLUSION

The present work dealt with different aspects of fibrous material formation and characterization of their physico-chemical and mechanical behavior. These aspects involved viscoelastic behavior of various liquids as an essential requirement for their spinnability required for fiber formation. Accordingly, viscoelastic behavior revealed by blood threads important in forensic applications puts them in the same category as viscoelastic jets of biopolymers used to form nano-textured membranes for heavy metal adsorption. Several novel experimental setups were designed, built and use to form threads and fibers of viscoelastic liquids and to study their behavior. A theoretical framework was developed and verified to explain the observations.

It was shown that the novel fiber forming process of solution blowing can be scaled up to industrial levels. This development leads to a significant increase in the nanofiber production rate, which holds great promise for such fields as water treatment and energy storage.

A novel method for the characterization of thin fibrous materials, i.e., paper, was proposed. This is important for protection of the core material by the protective outer paper layer in punched laminate composites. The method developed here allows for measurements of such mechanical parameters as Young’s modulus and Poisson’s ratio of fibrous materials under compression in the off-plane direction.

The findings of this work open ways for wide-scale application of novel fibrous in several industries with the full understanding and control of their properties and mechanisms of operation.

10. APPENDICES

Appendix A

Mechanical Properties of Biopolymer-containing Nanofiber Mats.

Using the extensional and load data, the true stress (σ_{true}) and strain (ε_{true}) of the tested nanofiber mat was calculated. Typical stress-strain curves for lignin-, soy- and oat-containing nanofiber mats are shown in Figure S1. The strain-stress relationships can be fitted by the elastic−plastic Green equation[1-2]

$$\sigma_{true} = Y \tanh\left(\frac{E\varepsilon_{true}}{Y}\right) \quad \text{(A1)}$$

where E is Young's modulus, and Y is the yield stress.

The experimental data was using eq A1 as shown in Figure A1. The average values of Young's modulus and the yield stress obtained are listed in Table A1.

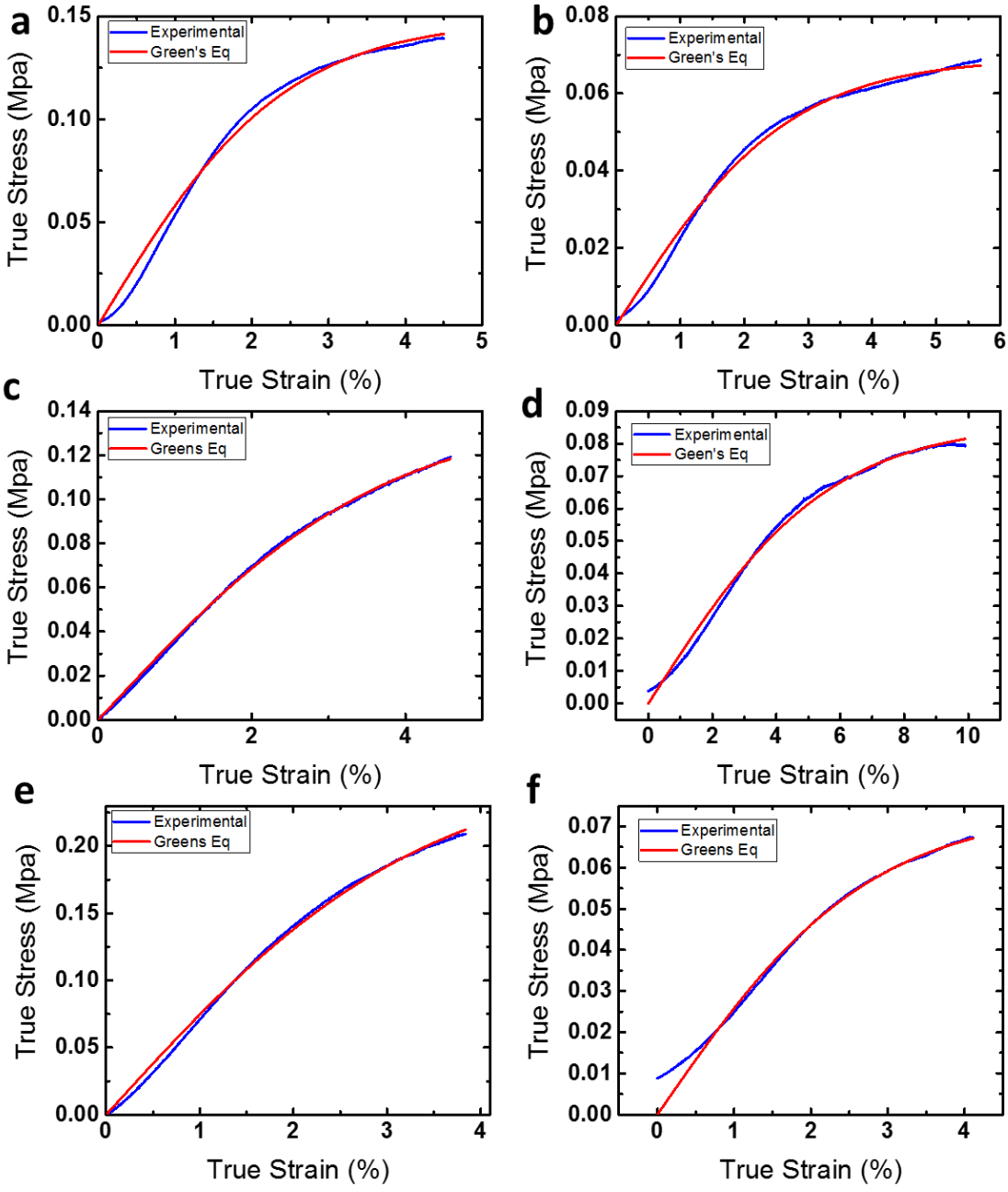

Figure A1. Stress−strain curves for biopolymer-containing solution-blown nanofiber mats. (a) Lignin/nylon-6 in the machine direction. (b) Lignin/nylon-6 in the cross-machine direction. (c) Soy/nylon-6 in the machine direction. (d) Soy/nylon-6 in the cross-machine direction. (e) Oats/nylon-6 in the machine direction. (f) Oats/nylon-6 in the cross-machine direction.

Table A2. Mechanical properties of biopolymer-containing nano-textured nonwovens.

Sample	Average thickness (mm)	Machine direction		Cross-machine direction	
		Average Young's modulus (MPa)	Average yield stress (kPa)	Average Young's modulus (MPa)	Average yield stress (kPa)
Lignin	0.4	6.1	148	2.6	70
Soy protein	0.3	3.7	141	1.5	86.4
Oats	0.4	7.6	260	2.7	74

Lignin Loss form Nonwoven Membrane

The raw lignin powder used to form nanofiber mats is fully soluble in water and, accordingly, it was observed that some lignin is lost during the adsorption experiment. To quantify this lignin loss, the mass of the nanofiber mats containing lignin was measured before and after submerging in the aqueous solution of lead for different time intervals. The results are shown in Figure A2. It was seen that lignin has been lost from the mats for about the first 20 min. During this time about 50% of the mass of the nanofiber mat was lost. It should be emphasized that the host polymer in the lignin-containing nanofiber mats was nylon-6, which is insoluble in water. Therefore the mass loss stemmed from the loss of lignin due to its high solubility in water. However, after that no lignin losses were recorded and the rest 50% of lignin stayed in the nanofiber mat. Although the maximum solubility of lignin was not measured in the present work, it was observed that 500 mg of lignin powder dissolved in 100 mL completely. This is significantly higher than 10-25 mg which was the total mass of lignin available in the nanofibers used for the adsorption experiments. Also, the effect of the dissolved lignin on the heavy metal concentration was studied by dissolving 100 mg of lignin powder in

100 mL of 5 ppm aqueous solution of lead. After dissolving the lignin completely, atomic absorption spectroscopy revealed that there was no change in the lead concentration in solution. It means that there was no precipitation caused by the dissolved lignin. Therefore, only the lignin remaining on the nanofiber mat surface plays a role in the adsorption kinetics.

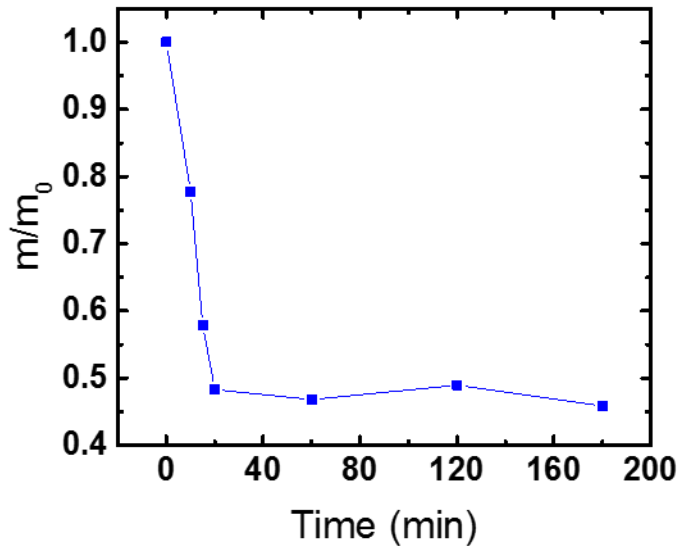

Figure A2. Fraction of the lignin remaining in a nanofiber mat versus time. Here m denotes the mass of lignin in the nanofiber mat at any given time and m_0 denotes the mass of lignin in the dry nanofiber mat.

Porosity Measurement of Nanofiber Mat

To measure porosity of nanofiber mats two different methods were used. Firstly, water filtration was used to measure sample permeability employing Darcy's law for filtration through porous medium

$$Q = \frac{-KA}{\mu}\frac{(p_f - p_0)}{\ell} \qquad \text{(A2)}$$

where Q is the flow rate, A is the projected sample face area, p_0 and p_f are the water pressures before and behind the sample, μ is the viscosity of water, ℓ is the sample thickness across the flow, and K is the sample permeability. The filtration setup used in these experiments is shown in Figure S3. In this setup, water pas pumped into the reservoir shown in Figure S3 until the maximum pump pressure and the pressure in the air supply line became equal. After that, the water column height in the reservoir remained constant. The pressure drop across the sample was then the sum of the hydrostatic pressure in the reservoir and the gage pressure in the air supply line. The air pressure was applied to the water column at its upper free surface. The flow rate was measured with a beaker and a stopwatch.

This approach, however, was not successful. The flow rate of water through the samples continuously dropped during the test (15 min). This was attributed to the hydrophilicity of nylon-6 contained in the nanofiber membranes together with lignin. As nylon-6 absorbed water, nanofibers changed in diameter altering the permeability and porosity of the sample.

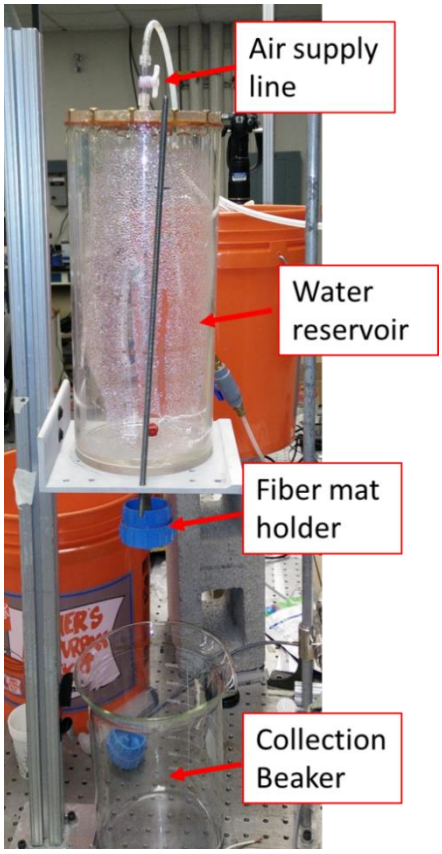

Figure A3. Porosity measurements of lignin/nylon-6 nanofiber mats in filtration setup with water.

Exactly the same approach was also used with air as the working medium. The corresponding setup is shown in Figure A4. In this setup, air was passed through the filter holder containing the membrane and a flowmeter at 9 liter/min. The pressure gauge was used to measure the pressure drop across the filter. The empty filter holder practically did not contribute to the pressure drop. The resulting permeability of the membranes was found to be $3\times 10^{-11}\,m^2$.

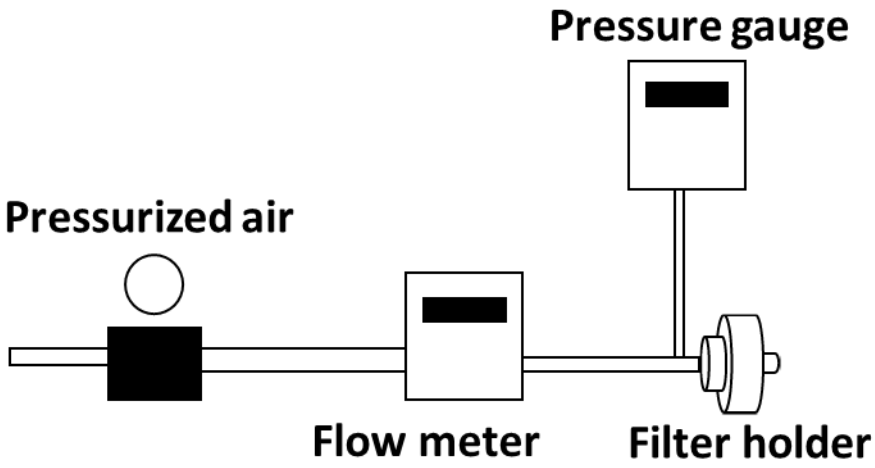

Figure A4. Porosity measurements of lignin/nylon-6 nanofiber mats in the filtration setup with air.

The sample porosity was measured using the analysis of SEM images of the nanofiber mats. The topmost layer of nanofibers in the SEM images (shown on the left in Figure A5) was isolated using Photoshop and revealed separately on the right in Figure A5. The contrast and brightness were adjusted so that it was possible to clearly recognize only the nanofibers which were in focus, i.e. in the topmost layer. A MATLAB program then converted the images from gray scale to black using a prescribed threshold. In the processed images nanofibers are black and the pores are white, as is seen in Figure A5 on the right. Finally, to calculate the porosity, the number of white pixels was divided by the total number of pixels in the image. SEM images at several location of the filter was taken. The resulting average porosity value was P=0.54.

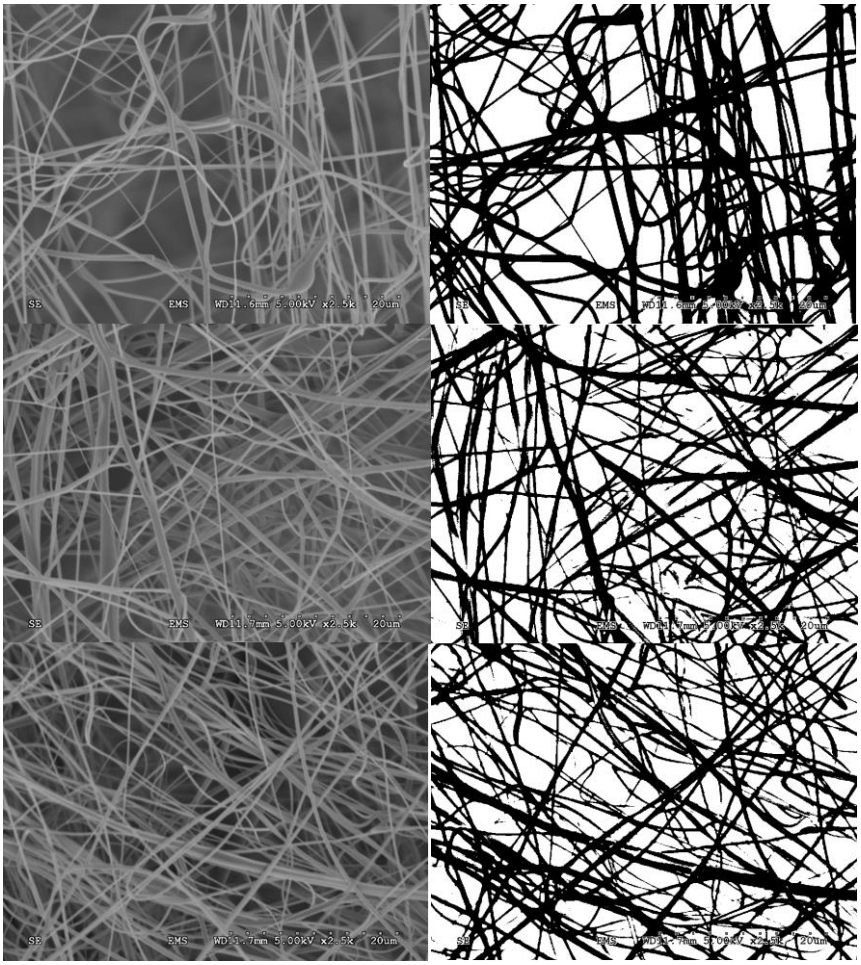

Figure A5. Lignin/nylon-6 sample with the average porosity of P=0.54.

Appendix B

Measurement of the principal stress sum

An optical flat is a common tool used to measure flatness. When an optical flat is placed on a flat reflective surface it rests on the high spots of the material forming a very thin gap everywhere else. When a light ray passes through the optical flat, a part of it is reflected off the rear surface of the flat and another part is reflected off the sample surface. These two rays superimpose and depending on the distance between the two surfaces they form a colorful interference patterns similar to those seen in thin films or in the Newton rings. Two adjacent lines correspond to the height difference of one wavelength of light of a certain color. It should be emphasized that the polycarbonate substrate before loading has surface undulations, which result in the interference pattern. After loading the pattern changes because of the polycarbonate surface bulging and thus, the redistribution of the gap thicknesses between the surface and optical flat. Using image analysis software developed in-house, prior to loading the total number of lines in the interference pattern between two reference points (cf. Fig. B1) is measured. Then, after loading, the total number of lines between the same reference points is measured again. It should be emphasized that the reference point on the left in Fig. S1 is located at the continuation of the centerline of the punch at a distance of 4 mm below the polycarbonate surface in contact with the punch. The second reference point in Fig. b1 is located on the same level as the first one but significantly aside from the punch and the effect from the punch there is negligibly small (a practically zero compressive stress).

The measured difference in the total number of lines between the two points prior and after loading ΔN results in the accurate measurement of the bulging displacement $u_z = \lambda \Delta N$, with λ being the wavelength of light. On the other hand, $u_z = \varepsilon_{zz} H$, where H is the thickness

of the substrate, and the bulging strain ε_{zz} is given by Eq. (8.87) in the main text. Then, from Eq. (8.87) the principal stress sum $\left(\sigma_{xx}+\sigma_{yy}\right)$ is found as

$$\left(\sigma_{xx}+\sigma_{yy}\right)=\frac{-E_{pol}}{\nu_{pol}}\frac{u_z}{H} \tag{B1}$$

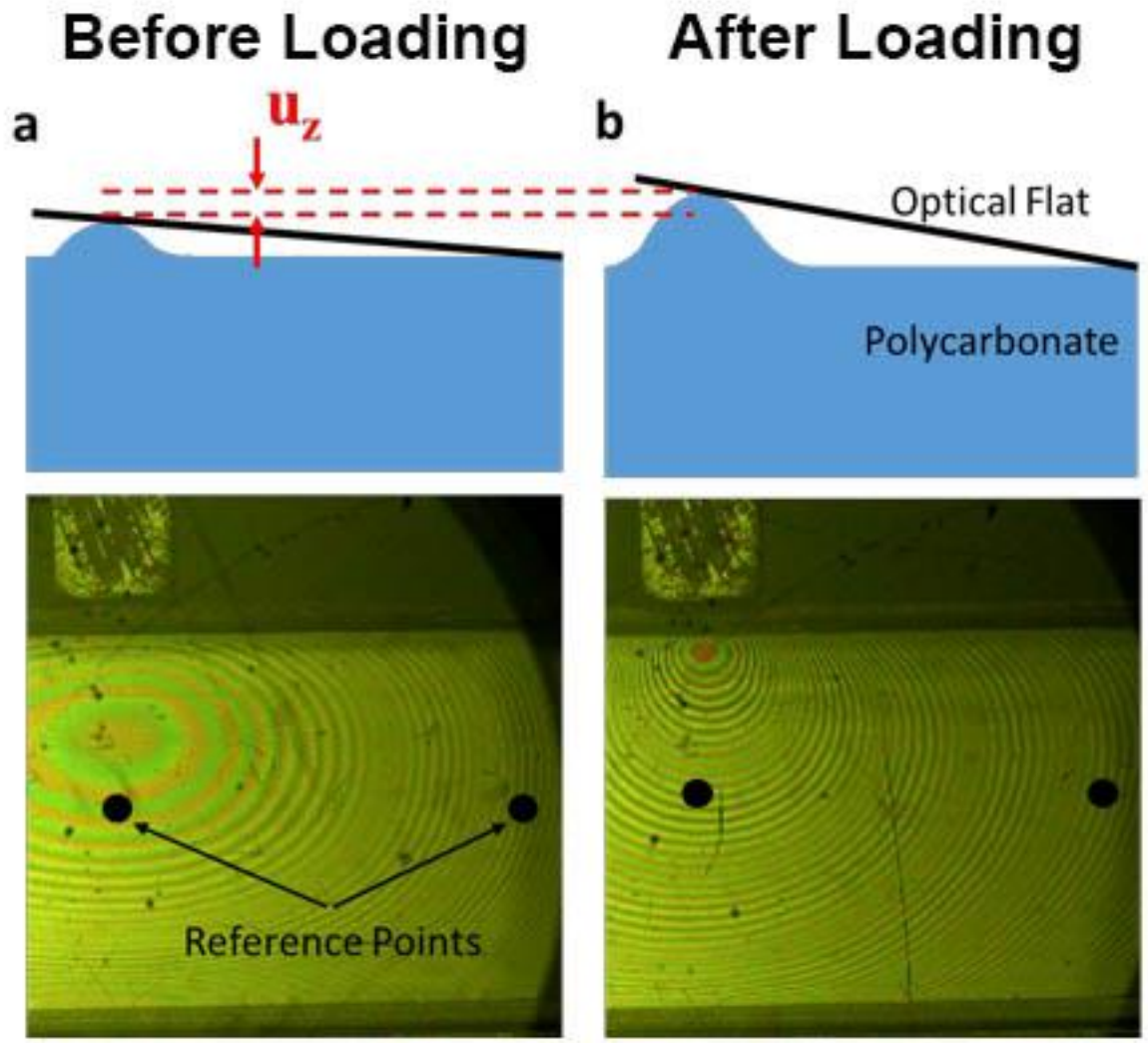

Fig. B1. The general scheme for measuring the bulging displacement using optical flat. (a) Before loading, and (b) after loading. The top parts of both panels show the schematics, whereas the lower parts - the observed fringe patterns.

Long-term paper creep of paper

The experimental setup shown in Fig. 8.8a was used to measure the stress in the polycarbonate substrate immediately after the load of 300 N was applied by punch at the paper surface on top of the substrate. If the sample remains loaded (the punch stops moving when the load of 300 N has been reached), it was observed that the load measured by the load cell attached to the punch decreases with time (Fig. B2). As a control, the polycarbonate substrate was also loaded without paper on top exactly as it was loaded with paper. In the case without paper it was found that there was no decrease in the load cell reading. This clearly shows that the reduction in stress happens entirely due to paper. That means that paper creeps under a constant load. The creep data (black symbols in Fig. B2) appeared to follow an exponential decay law (Rabotnov 1969)

$$F = Ae^{-t/\theta} + B \qquad \text{(B2)}$$

as the fitted red line in Fig. B2 shows.

In Eq. (B2) F is the measured load, A and B are constants, t is time, and θ is the characteristic creep time.

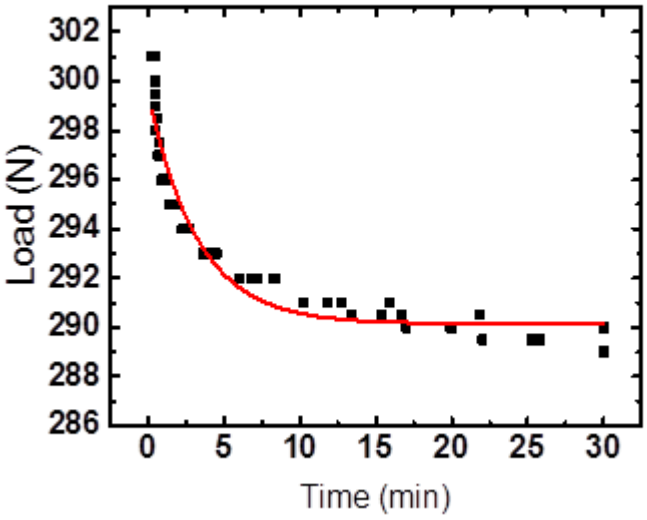

Fig. B2: Long-term paper creep. The data shown by black symbols is traced by the red line. The corresponding creep time is θ=3.24 min.

Appendix B

The following are the statements form the publisher granting permission to use previously published articles of the present author in this thesis.

Permission granted by Springer Nature addresses the work on the rheology of blood from sections 2.1, 3.1, and Chapter 4. These sections are reproduced by permission of Springer Nature and the links of the papers are as follows:

https://link.springer.com/article/10.1007/s00397-016-0964-1

Permission granted by American Chemical Society addresses the work on the industrialization of solution blowing from sections 2.2, 3.2, and Chapter 5. These sections are reproduced by permission of American Chemical Society and the links of the papers are as follows:

https://pubs.acs.org/doi/abs/10.1021/acs.iecr.5b04277

Permission granted by ELSEVIER addresses the work on heavy metal adsorption from sections 2.4, 3.4 and Chapter 7, and also for the work on the mechanical behavior of fibrous materials in the z-direction from sections 2.5, 3.5 and Chapter 8. These sections are reproduced by permission of ELSEVIER and the links of the papers are as follows:

https://www.sciencedirect.com/science/article/pii/S0376738817301618

https://www.sciencedirect.com/science/article/pii/S0022509619301383

Title: Heavy metal adsorption on solution-blown biopolymer nanofiber membranes

Author: A. Kolbasov,S. Sinha-Ray,A.L. Yarin,B. Pourdeyhimi

Publication: Journal of Membrane Science

Publisher: Elsevier

Date: 15 May 2017

Order Completed

Thank you for your order.

This Agreement between 6447 Berkshire Ct. ("You") and Springer Nature ("Springer Nature") consists of your license details and the terms and conditions provided by Springer Nature and Copyright Clearance Center.

Your confirmation email will contain your order number for future reference.

printable details

License Number	4656681077052
License date	Aug 26, 2019
Licensed Content Publisher	Springer Nature
Licensed Content Publication	Rheologica Acta
Licensed Content Title	Blood rheology in shear and uniaxial elongation
Licensed Content Author	Alexander Kolbasov, Patrick M. Comiskey, Rakesh Prasad Sahu et al
Licensed Content Date	Jan 1, 2016
Licensed Content Volume	55
Licensed Content Issue	11
Type of Use	Thesis/Dissertation
Requestor type	academic/university or research institute
Format	print and electronic
Portion	full article/chapter
Will you be translating?	no
Circulation/distribution	<501
Author of this Springer Nature content	yes
Title	Rheological, Mechanical and Physico-chemical Behavior of Fibrous Materials
Institution name	University of Illinois at Chicago
Expected presentation date	Aug 2019
Requestor Location	6447 Berkshire Ct. 6447 Berkshire Ct. LISLE, IL 60532 United States Attn: 6447 Berkshire Ct.
Total	0.00 USD

Title: Industrial-Scale Solution Blowing of Soy Protein Nanofibers

Author: Alexander Kolbasov, Suman Sinha-Ray, Abhay Joijode, et al

Publication: Industrial & Engineering Chemistry Research

Publisher: American Chemical Society

Date: Jan 1, 2016

PERMISSION/LICENSE IS GRANTED FOR YOUR ORDER AT NO CHARGE

This type of permission/license, instead of the standard Terms & Conditions, is sent to you because no fee is being charged for your order. Please note the following:

- Permission is granted for your request in both print and electronic formats, and translations.
- If figures and/or tables were requested, they may be adapted or used in part.
- Please print this page for your records and send a copy of it to your publisher/graduate school.
- Appropriate credit for the requested material should be given as follows: "Reprinted (adapted) with permission from (COMPLETE REFERENCE CITATION). Copyright (YEAR) American Chemical Society." Insert appropriate information in place of the capitalized words.
- One-time permission is granted only for the use specified in your request. No additional uses are granted (such as derivative works or other editions). For any other uses, please submit a new request.

Title: Theoretical and experimental study of punched laminate composites protected by outer paper layer

Author: Alexander Kolbasov,Suman Sinha-Ray,Alexander L. Yarin

Publication: Journal of the Mechanics and Physics of Solids

Publisher: Elsevier

Date: July 2019

11. CITED LITERATURE

Aksu, Z. Application of biosorption for the removal of organic pollutants: a review. Process Biochemistry 40, 3 (2005), 997 – 1026.

Allain, C., and Limat, L. Regular patterns of cracks formed by directional drying of a collodial suspension. Physical review letters 74, 15 (1995), 2981.

Angot, A. Complements de Mathematiques. Éd. de la Revue d&optique, Paris.1965.

Apostolidis, A. J., and Beris, A. N. Modeling of the blood rheology in steady-state shear flows. Journal of Rheology 58, 3 (2014), 607–633.

Assembly, U. G. Resolution 64/292: The human right to water and sanitation. 64th Session. (2010).

Attinger, D., Haferl, S., Zhao, Z., and Poulikakos, D. Transport phenomena in the impact of a molten droplet on a surface: Part ii: Heat transfer and solidification. Annual Review of Heat Transfer 11 (2000).

Attinger, D., Moore, C., Donaldson, A., Jafari, A., and Stone, H. A. Fluid dynamics topics in bloodstain pattern analysis: comparative review and research opportunities. Forensic science international 231, 1-3 (2013), 375–396.

Babel, S., and Kurniawan, T. A. Low-cost adsorbents for heavy metals uptake from contaminated water: a review. Journal of Hazardous Materials 97, 1 (2003), 219 – 243.

Bailey, S. E., Olin, T. J., Bricka, R., and Adrian, D. A review of potentially low-cost sorbents for heavy metals. Water Research 33, 11 (1999), 2469 – 2479.

Barakat, M. New trends in removing heavy metals from industrial wastewater. Arabian Journal of Chemistry 4, 4 (2011), 361 – 377.

Bartolo, D., Bouamrirene, F., Verneuil, E., Buguin, A., Silberzan, P., and Moulinet, S. Bouncing or sticky droplets:Impalement transitions on superhydrophobic micropatterned surfaces. EPL (Europhysics Letters) 74, 2 (2006), 299.

Behrens, A. M., Casey, B. J., Sikorski, M. J., Wu, K. L., Tutak, W., Sandler, A. D., and Kofinas, P. In situ deposition of PLGA nanofibers via solution blow spinning. ACS Macro Letters 3, 3 (2014), 249–254.

Behrooz, N., Hulse-Smith, L., and Chandra, S. An evaluation of the underlying mechanisms of bloodstain pattern analysis error. Journal of forensic sciences 56, 5 (2011), 1136–1142.

Bertola, V. An experimental study of bouncing leidenfrost drops: Comparison between newtonian and viscoelastic liquids. International Journal of Heat and Mass Transfer 52, 7 (2009), 1786 – 1793.

Bevel, T., and Gardner, R. M. Bloodstain Pattern Analysis with an Introduction to Crime Scene Reconstruction. CRC Press, Boca Raton 2008.

Bouterf, A., Adrien, J., Maire, E., Brajer, X., Hild, F., and Roux, S. Failure mechanisms of plasterboard in nail pull test determined by x-ray microtomography and digital volume correlation. Experimental Mechanics 56, 8 (2016), 1427–1437.

Bouterf, A., Adrien, J., Maire, E., Brajer, X., Hild, F., and Roux, S. Identification of the crushing behavior of brittle foam: From indentation to oedometric tests. Journal of the Mechanics and Physics of Solids 98 (2017), 181 – 200.

Brust, M., Schaefer, C., Doerr, R., Pan, L., Garcia, M., Arratia, P. E., and Wagner, C. Rheology of human blood plasma: Viscoelastic versus newtonian behavior. Phys. Rev. Lett. 110 (2013), 078305.

Carre, A., Gastel, J.C., and Shanahan, M. E. Viscoelastic effects in the spreading of liquids. Nature 379, 6564 (1996), 432.

Caviezel, D., Narayanan, C., and Lakehal, D. Adherence and bouncing of liquid droplets impacting on dry surfaces. Microfluidics and Nanofluidics 5, 4 (2008), 469–478.

Chandrasekhar, S. Hydrodynamic and hydromagnetic stability. Courier Corporation, 2013.

Charm, S., and Kurland, G. Viscometry of human blood for shear rates of 0-100,000 sec- 1. Nature 206, 4984 (1965), 617.

Chen, L., and Li, Z. Bouncing droplets on nonsuperhydrophobic surfaces. Phys. Rev. E 82 (2010), 016308.

Chen, Z., and Yan, N. Investigation of elastic moduli of kraft paper honeycomb core sandwich panels. Composites Part B: Engineering 43, 5 (2012), 2107 – 2114.

Cherepanov, G. P. Mechanics of Brittle Fracture. McGraw Hill., New York, 1979.

Chien, S., King, R., Skalak, R., Usami, S., and Copley, Viscoelastic properties of human blood and red cell suspensions. Biorheology 12, 6 (1975), 341–346.

Clasen, C., Bico, J., Entov, V. M., and McKinley, G. H. ‘Gobbling drops’: the jetting–dripping transition in flows of polymer solutions. Journal of Fluid Mechanics 636 (2009), 5–40.

Cooper-White, J., Crooks, R., and Boger, D. A drop impact study of worm-like viscoelastic surfactant solutions. Colloids and Surfaces A: Physicochemical and Engineering Aspects 210, 1 (2002), 105 – 123.

Copley, A., King, R., Chien, S., Usami, S., Skalak, R., and Huang, C. Microscopic observations of viscoelasticity of human blood in steady and oscillatory shear. Biorheology 12, 5 (1975), 257—263.

Cox, H. L. The elasticity and strength of paper and other fibrous materials. British Journal of Applied Physics 3, 3 (1952), 72–79.

Cramer, S., Friday, O., White, R., and Sriprutkiat, G. Mechanical properties of gypsum board at elevated temperatures. In Fire and materials 2003: 8th International Conference, January 2003, San Francisco, CA, USA. London: Interscience Communications Limited, c2003: pages 33-42. (2003).

Davidson, E. A., and Trumbore, S. E. Gas diffusivity and production of co2 in deep soils of the eastern amazon. Tellus B: Chemical and Physical Meteorology 47, 5 (1995), 550–565.

De Gennes, P. Coil-stretch transition of dilute flexible polymers under ultrahigh velocity gradients. The Journal of Chemical Physics 60, 12 (1974), 5030–5042.

De Gruttola, S., Boomsma, K., and Poulikakos, D. Computational simulation of a non-newtonian model of the blood separation process. Artificial Organs 29, 12 (2005), 949–959.

Devarayan, K., Hanaoka, H., Hachisu, M., Araki, J., Ohguchi, M., Behera, B. K., and Ohkawa, K. Direct electrospinning of cellulose–chitosan composite nanofiber. Macromolecular Materials and Engineering 298, 10 (2013), 1059–1064.

Dikin, D. A., Stankovich, S., Zimney, E. J., Piner, R. D., Dommett, G. H., Evmenenko, G., Nguyen, S. T., and Ruoff, R. S. Preparation and characterization of graphene oxide paper. Nature 448, 7152 (2007), 457.

Du, X., and He, J. Hierarchically mesoporous silica nanoparticles: Extraction, amino-functionalization, and their multipurpose potentials. Langmuir 27, 6 (2011), 2972–2979.

Eggers, J., and Villermaux, E. Physics of liquid jets. Reports on Progress in Physics 71, 3 (2008), 036601.

England, A. H. Complex Variable Methods in Elasticity.. John Wiley & Sons, New York, 1971.

Errill, E. W. Rheology of blood. Physiological Reviews 49, 4 (1969), 863–888.

Farooq, U., Kozinski, J. A., Khan, M. A., and Athar, M. Biosorption of heavy metal ions using wheat based biosorbents – a review of the recent literature. Bioresource Technology 101, 14 (2010), 5043 – 5053.

F˚ahræus, R., and Lindqvist, T. The viscosity of the blood in narrow capillary tubes. American Journal of Physiology-Legacy Content 96, 3 (1931), 562–568.

Friberg, L., and Elinder, C. Encyclopedia of occupational Health. International Labor Organization, Geneva (1985).

Fu, F., and Wang, Q. Removal of heavy metal ions from wastewaters: A review. Journal of Environmental Management 92, 3 (2011), 407 – 418.

Galin, L. A. Contact Problems: the Legacy of LA Galin, Springer Science & Business Media, Heidelberg 2008.

Gardea-Torresdey, J., Tiemann, K., Armendariz, V., BessOberto, L., Chianelli, R., Rios, J., Parsons, J., and Gamez, G. Characterization of cr(vi) binding and reduction to cr(iii) by the agricultural byproducts of avena monida (oat) biomass. Journal of Hazardous Materials 80, 1 (2000), 175 – 188.

Garg, U. K., Kaur, M., Garg, V., and Sud, D. Removal of hexavalent chromium from aqueous solution by agricultural waste biomass. Journal of Hazardous Materials 140, 1 (2007), 60 – 68.

Gibson, L. J., and Ashby, M. F. Cellular Solids: Structure and Properties. Cambridge University Press, Cambridge (1999).

Green, A. E. Hypo-elasticity and plasticity. Proceedings of the Royal Society of London. Series A. Mathematical and Physical Sciences 234, 1196 (1956), 46–59.

Guo, X., Zhang, S., and quan Shan, X. Adsorption of metal ions on lignin. Journal of Hazardous Materials 151, 1 (2008), 134 – 142.

Haider, S., and Park, S.-Y. Preparation of the electrospun chitosan nanofibers and their applications to the adsorption of cu(ii) and pb(ii) ions from an aqueous solution. Journal of Membrane Science 328, 1 (2009), 90 – 96.

Hanssen, A., Girard, Y., Olovsson, L., Berstad, T., and Langseth, M. A numerical model for bird strike of aluminium foambased sandwich panels. International Journal of Impact Engineering 32, 7 (2006), 1127 – 1144.

Harrysson, A., and Ristinmaa, M. Large strain elasto-plastic model of paper and corrugated board. International Journal of Solids and Structures 45, 11 (2008), 3334 – 3352.

Hassan, S. A. Amino acid side chain interactions in the presence of salts. The Journal of Physical Chemistry B 109, 46 (2005), 21989– 21996.

Havl´ınova, B., Katu´ ˇscˇak, S., Petrovi´ covˇ a, M., Makov´ a, A.,´ and Brezova, V.´ A study of mechanical properties of papers exposed to various methods of accelerated ageing. part i. the effect of heat and humidity on original wood-pulp papers. Journal of Cultural Heritage 10, 2 (2009), 222 – 231.

Henrici, P. Applied and Computational Complex Analysis. John Wiley & Sons, New York 1974.

Hettiarachchy, N. S., Kalapathy, U., and Myers, D. J. Alkali-modified soy protein with improved adhesive and hydrophobic properties. Journal of the American Oil Chemists' Society 72, 12 (1995), 1461–1464.

Hirn, U., and Schennach, R. Comprehensive analysis of individual pulp fiber bonds quantifies the mechanisms of fiber bonding in paper. Scientific Reports 5 (2015), 10503.

Hou, W., Zhu, F., Lu, G., and Fang, D.-N. Ballistic impact experiments of metallic sandwich panels with aluminium foam core. International Journal of Impact Engineering 37, 10 (2010), 1045 – 1055.

Hoyt, J. W., and Taylor, J. J. Turbulence structure in a water jet discharging in air. The Physics of Fluids 20, 10 (1977), S253–S257.

Huang, C., Chen, H., Pan, W., Shih, T., Kristol, D., and Copley, A. Effects of hematocrit on thixotropic properties of human blood. Biorheology 24, 6 (1987), 803–810.

Hung, T., Hochmuth, R., Joist, J., and Sutera, S. Shearinduced aggregation and lysis of platelets. ASAIO Journal 22, 1 (1976), 285–290.

Ibrahim, R. Structural, mechanical and optical properties of recycled paper blended with empty oil palm fruit bunch pulp. Journal of Oil Palm Research 15, 2 (2003), 28–34.

Ignatova, M., Manolova, N., and Rashkov, I. Electrospun antibacterial chitosan-based fibers. Macromolecular Bioscience 13, 7 (2013), 860–872.

Jain, C. K., Malik, D. S., and Yadav, A. K. Applicability of plant based biosorbents in the removal of heavy metals: a review. Environmental Processes 3, 2 (Jun 2016), 495–523.

Jiang, T., Ouyang, J., Yang, B., and Ren, J. The sph method for simulating a viscoelastic drop impact and spreading on an inclined plate. Computational Mechanics 45, 6 (May 2010), 573–583.

Johnson, L., Myers, D., Burden, D., et al. Early uses of soy protein in far east. Inform 3 (1984), 282–284.

Johnston, B. M., Johnston, P. R., Corney, S., and Kilpatrick, D. Non-newtonian blood flow in human right coronary arteries: steady state simulations. Journal of Biomechanics 37, 5 (2004), 709 – 720.

Joseph, D., Belanger, J., and Beavers, G. Breakup of a liquid drop suddenly exposed to a high-speed airstream. International Journal of Multiphase Flow 25, 6 (1999), 1263 – 1303.

Kalapathy, U., Hettiarachchy, N. S., Myers, D., and Hanna, M. A. Modification of soy proteins and their adhesive properties on woods. Journal of the American Oil Chemists' Society 72, 5 (1995), 507–510.

Khansari, S., Duzyer, S., Sinha-Ray, S., Hockenberger, A., Yarin, A. L., and Pourdeyhimi, B. Two-stage desorptioncontrolled release of fluorescent dye and vitamin from solution-blown and electrospun nanofiber mats containing porogens. Molecular Pharmaceutics 10, 12 (2013), 4509–4526.

Khansari, S., Sinha-Ray, S., Yarin, A. L., and Pourdeyhimi, Stress-strain dependence for soy-protein nanofiber mats. Journal of Applied Physics 111, 4 (2012), 044906.

Khansari, S., Sinha-Ray, S., Yarin, A. L., and Pourdeyhimi, Biopolymer-based nanofiber mats and their mechanical characterization. Industrial & Engineering Chemistry Research 52, 43 (2013), 15104–15113.

Klass, D. L. Biomass for Renewable Energy, Fuels, and Chemicals. Academic Press, San Diego, 1998.

Kolbasov, A., Sinha-Ray, S., Joijode, A., Hassan, M. A., Brown, D., Maze, B., Pourdeyhimi, B., and Yarin, A. L. Industrial-scale solution blowing of soy protein nanofibers. Industrial & Engineering Chemistry Research 55, 1 (2016), 323–333.

Koombhongse, S., Liu, W., and Reneker, D. H. Flat polymer ribbons and other shapes by electrospinning. Journal of Polymer Science Part B: Polymer Physics 39, 21 (2001), 2598–2606.

Koubaa, A., and Koran, Z. Measure of the internal bond strength of paper/board. Tappi Journal 78, 3 (1995), 103–112.

Kurniawan, T. A., Chan, G. Y., hung Lo, W., and Babel, S. Comparisons of low-cost adsorbents for treating wastewaters laden with heavy metals. Science of The Total Environment 366, 2 (2006), 409 – 426.

Laber, T. L., Epstein, B. P., and Taylor, M. C. High speed digital video analysis of bloodstain pattern formation from common bloodletting mechanisms. IABPA News 24, 2 (2008), 4–12.

Landau, L. D., and Lifshitz, E. M. Theory of Elasticity. Pergamon Press, Oxford, 1970.

Lee, H. C. Drop formation in a liquid jet. IBM Journal of Research and Development 18, 4 (July 1974), 364–369.

Leech, H. J. An investigation of the reasons for increase in paper strength when beater adhesives are used. PhD thesis, Georgia Institute of Technology, 1953.

Leuprecht, A., and Perktold, K. Computer simulation of non-Newtonian effects on blood flow in large arteries. Computer Methods in Biomechanics and Biomedical Engineering 4, 2 (2001), 149– 163.

Lin, S. P., and Reitz, R. D. Drop and spray formation from a liquid jet. Annual Review of Fluid Mechanics 30, 1 (1998), 85–105.

Lin, Y.-F., and Chen, J.-L. Magnetic mesoporous fe/carbon aerogel structures with enhanced arsenic removal efficiency. Journal of Colloid and Interface Science 420 (2014), 74 – 79.

Liu, C., Zhang, Y., and Ye, L. High velocity impact responses of sandwich panels with metal fibre laminate skins and aluminium foam core. International Journal of Impact Engineering 100 (2017), 139 – 153.

Liu, D., Li, Z., Li, W., Zhong, Z., Xu, J., Ren, J., and Ma, Z. Adsorption behavior of heavy metal ions from aqueous solution by soy protein hollow microspheres. Industrial & Engineering Chemistry Research 52, 32 (2013), 11036–11044.

Lurie, A., and Belyaev, A. Three-dimensional problems in the theory of elasticity. In Theory of Elasticity. Springer, Heidelberg, 2005, pp. 243– 407.

Mann, R. W., Baum, G. A., and Habeger Jr, C. C. Determination of All Nine Orthotropic Elastic Constants for Machine-Made Paper. The Institute of Paper Chemistry, Technical Paper Series, N 84, Appleton, Wisconsin, 1979.

Matovich, M. A., and Pearson, J. R. A. Spinning a molten threadline. steady-state isothermal viscous flows. Industrial & Engineering Chemistry Fundamentals 8, 3 (1969), 512–520.

Medeiros, E. S., Glenn, G. M., Klamczynski, A. P., Orts, W. J., and Mattoso, L. H. C. Solution blow spinning: A new method to produce micro- and nanofibers from polymer solutions. Journal of Applied Polymer Science 113, 4 (2009), 2322–2330.

Medhekar, N. V., Ramasubramaniam, A., Ruoff, R. S., and Shenoy, V. B. Hydrogen bond networks in graphene oxide composite paper: Structure and mechanical properties. ACS Nano 4, 4 (2010), 2300–2306.

Meiselman, H., Neu, B., Rampling, M., and Baskurt, O. Rbc aggregation: laboratory data and models. Indian Journal of Experfimental Biology 45 (2007), 9–17.

Mighri, F., Carreau, P. J., and Ajji, A. Influence of elastic properties on drop deformation and breakup in shear flow. Journal of Rheology 42, 6 (1998), 1477–1490.

Mäkelä, P., and Östlund, S Orthotropic elastic–plastic material model for paper materials. International Journal of Solids and Structures 40, 21 (2003), 5599 – 5620.

Morshed, K. N., Bark Jr., D., Forleo, M., and Dasi, L. P. Theory to predict shear stress on cells in turbulent blood flow. PLOS ONE 9, 8 (08 2014), 1–17.

Muskhelishvili, N. I. Some Basic Problems of the Mathematical Theory Of Elasticity. Nordhoff Intern. Publishing, Leyden, 1975.

Ngah, W. W., and Hanafiah, M. Removal of heavy metal ions from wastewater by chemically modified plant wastes as adsorbents: A review. Bioresource Technology 99, 10 (2008), 3935 – 3948.

Oliveira, J. E., Zucolotto, V., Mattoso, L. H., and Medeiros, E. S. Multi-walled carbon nanotubes and poly (lactic acid) nanocomposite fibrous membranes prepared by solution blow spinning. Journal of Nanoscience and Nanotechnology 12, 3 (2012), 2733–2741.

Patterson, J. Industrial Wastewater Treatment Technology, Second edition. Butterworth, Stoneham, 1985.

Pinchuk, L. S., Goldade, V. A., Makarevich, A., and Kestelman, V. Melt Blowing: Equipment, Technology, and Polymer Fibrous Materials. Springer Science & Business Media, Berlin, 2002.

Poole, R., and Ridley, B. Development-length requirements for fully developed laminar pipe flow of inelastic non-newtonian liquids. Journal of Fluids Engineering 129, 10 (2007), 1281–1287.

Poulios, K., and Niordson, C. F. Homogenization of long fiber reinforced composites including fiber bending effects. Journal of the Mechanics and Physics of Solids 94 (2016), 433 – 452.

Qu, R., Zhang, Z., Zhang, P., Liu, Z., and Zhang, Z. Generalized energy failure criterion. Scientific Reports 6 (2016), 23359.

Radford, D., McShane, G., Deshpande, V., and Fleck, N. The response of clamped sandwich plates with metallic foam cores to simulated blast loading. International Journal of Solids and Structures 43, 7 (2006), 2243 – 2259.

Rahmanian, I. Thermal and mechanical properties of gypsum boards and their influences on fire resistance of gypsum board based systems. PhD thesis, The University of Manchester (United Kingdom), 2011.

Ramstack, J., Zuckerman, L., and Mockros, L. Shear-induced activation of platelets. Journal of Biomechanics 12, 2 (1979), 113 – 125.

Rein, M. Phenomena of liquid drop impact on solid and liquid surfaces. Fluid Dynamics Research 12, 2 (1993), 61–93.

Reneker, D., Yarin, A., Zussman, E., and Xu, H. Electrospinning of Nanofibers from Polymer Solutions and Melts. Advances in Applied Mechanics. 41 , (2007) 43-195.

Reneker, D. H., Yarin, A. L., Fong, H., and Koombhongse, S. Bending instability of electrically charged liquid jets of polymer solutions in electrospinning. Journal of Applied Physics 87, 9 (2000), 4531–4547.

Rostamian, R., Najafi, M., and Rafati, A. A. Synthesis and characterization of thiol-functionalized silica nano hollow sphere as a novel adsorbent for removal of poisonous heavy metal ions from water: Kinetics, isotherms and error analysis. Chemical Engineering Journal 171, 3 (2011), 1004 – 1011

Rudra, S., Singh, V., Jyoti, S., and Shivhare, U. Mechanical properties and antimicrobial efficacy of active wrapping paper for primary packaging of fruits. Food Bioscience 3 (2013), 49 – 58.

Shambaugh, R. L. A macroscopic view of the melt-blowing process for producing microfibers. Industrial & Engineering Chemistry Research 27, 12 (1988), 2363–2372.

Sinha-Ray, S., Khansari, S., Yarin, A. L., and Pourdeyhimi, Effect of chemical and physical cross-linking on tensile characteristics of solution-blown soy protein nanofiber mats. Industrial & Engineering Chemistry Research 51, 46 (2012), 15109–15121.

Sinha-Ray, S., Lee, M. W., Sinha-Ray, S., An, S., Pourdeyhimi, B., Yoon, S. S., and Yarin, A. L. Supersonic nanoblowing: a new ultra-stiff phase of nylon 6 in 20–50 nm confinement. J. Mater. Chem. C 1 (2013), 3491–3498.

Sinha-Ray, S., Sinha-Ray, S., Yarin, A. L., and Pourdeyhimi, B. Theoretical and experimental investigation of physical mechanisms responsible for polymer nanofiber formation in solution blowing. Polymer 56 (2015), 452 – 463.

Sinha-Ray, S., Srikar, R., Lee, C., Li, A., and Yarin, A. Shear and elongational rheology of gypsum slurries. Applied Rheology 21, 6 (12 2011).

Sinha-Ray, S., Yarin, A., and Pourdeyhimi, B. The production of 100/400nm inner/outer diameter carbon tubes by solution blowing and carbonization of core–shell nanofibers. Carbon 48, 12 (2010), 3575 – 3578.

Sinha-Ray, S., Yarin, A. L., and Pourdeyhimi, B. Meltblowing: I-basic physical mechanisms and threadline model. Journal of Applied Physics 108, 3 (2010), 034912.

Sinha-Ray, S., Zhang, Y., Yarin, A. L., Davis, S. C., and Pourdeyhimi, B. Solution blowing of soy protein fibers. Biomacromolecules 12, 6 (2011), 2357–2363.

Skorik, Y. A., Pestov, A. V., and Yatluk, Y. G. Evaluation of various chitin-glucan derivatives from aspergillus niger as transition metal adsorbents. Bioresource Technology 101, 6 (2010), 1769 – 1775.

Soltani, M., Andalib, M., and Ravanbakhsh, M. Some physical and mechanical properties of uncatalysed acetylated paper. BioResources 8, 1 (2013), 1274–1282.

Steffe, J. F. Rheological methods in food process engineering. Freeman press, 1996.

Stenberg, N. On the out-of-plane mechanical behaviour of paper materials. PhD thesis, KTH, Solid Mechanics, 2002.

Stenberg, N. A model for the through-thickness elastic–plastic behaviour of paper. International Journal of Solids and Structures 40, 26 (2003), 7483–7498.

Sud, D., Mahajan, G., and Kaur, M. Agricultural waste material as potential adsorbent for sequestering heavy metal ions from aqueous solutions – a review. Bioresource Technology 99, 14 (2008), 6017 – 6027.

Thoroddsen, S., Etoh, T., and Takehara, K. High-speed imaging of drops and bubbles. Annual Review of Fluid Mechanics 40, 1 (2008), 257–285.

Tiwari, M. K., Bazilevsky, A. V., Yarin, A. L., and Megaridis, C. M. Elongational and shear rheology of carbon nanotube suspensions. Rheologica Acta 48, 6 (Jul 2009), 597–609.

Tropea, C.,Yarin, A. L. Foss, J. (Editors) Springer Handbook of Experimental Fluid Mechanics, vol. 1. Springer Science & Business Media, Heidelberg, 2007.

Uddin, M. N., Huang, Z.-D., Mai, Y.-W., and Kim, J.-K. Tensile and tearing fracture properties of graphene oxide papers intercalated with carbon nanotubes. Carbon 77 (2014), 481–491.

Vadahanambi, S., Lee, S.-H., Kim, W.-J., and Oh, I.-K. Arsenic removal from contaminated water using three-dimensional graphenecarbon nanotube-iron oxide nanostructures. Environmental Science & Technology 47, 18 (2013), 10510–10517.

Van Liew, G. P. The deformation of paper in the z-direction. PhD thesis, Georgia Institute of Technology, 1973.

Villanueva, G. R., and Cantwell, W. The high velocity impact response of composite and fml-reinforced sandwich structures. Composites Science and Technology 64, 1 (2004), 35–54.

Walker, H. K., Hall, W. D., and Hurst, J. W. Diplopia–Clinical Methods: The History, Physical, and Laboratory Examinations. Butterworths, Boston**,** 1990.

Wang, D. Impact behavior and energy absorption of paper honeycomb sandwich panels. International Journal of Impact Engineering 36, 1 (2009), 110–114.

Waterhouse, J. F. The failure envelope of paper when subjected to combined out-of-plane stresses. In Proceedings of the 1991 International Paper Physics Conference, Hawaii, Tappi, 1991.

Wickham, L., Bauersachs, R., Wenby, R., Sowemimo-Coker, S., Meiselman, H., and Elsner, R. Red cell aggregation and viscoelasticity of blood from seals, swine and man. Biorheology 27, 2 (1990), 191–204.

Williams, E., and Taylor, M. Standardising blood physical properties: implications for precision bloodstain pattern analysis research. In IABPA (International Association of Bloodstain Pattern Analysts) Training Conference, San Diego, CA (2013).

Windberger, U., Bartholovitsch, A., Plasenzotti, R., Korak, K. J., and Heinze, G. Whole blood viscosity, plasma viscosity and erythrocyte aggregation in nine mammalian species: reference values and comparison of data. Experimental Physiology 88, 3 (2003), 431–440.

Wittbold, J. R., Petersen, B. L., and Li, A. Foamed slurry and building panel made therefrom, 2011. US Patent 7,875,114.

Wurzinger, L., Opitz, R., Blasberg, P., and Schmid-Schonbein, H.¨ Platelet and coagulation parameters following millisecond exposure to laminar shear stress. Thrombosis and haemostasis 53, 02 (1985), 381–386.

Yarin, A. Drop impact dynamics: Splashing, spreading, receding, bouncing.... Annual Review of Fluid Mechanics 38, 1 (2006), 159–192.

Yarin, A., Pourdeyhimi, B., and Ramakrishna, S. Fundamentals and Applications of Micro and Nanofibers. Cambridge University Press, Cambridge, 2014.

Yarin, A., Sinha-Ray, S., and Pourdeyhimi, B. Meltblowing: Multiple polymer jets and fiber-size distribution and lay-down patterns. Polymer 52, 13 (2011), 2929 – 2938.

Yarin, A. L. Free Liquid Jets and Films: Hydrodynamics and Rheology. Longman Publishing Group, Harlow and John Wiley & Sons, New York 1993.

Yarin, A. L., Sinha-Ray, S., and Pourdeyhimi, B. Meltblowing: Linear and nonlinear waves on viscoelastic polymer jets. Journal of Applied Physics 108, 3 (2010), 034913.

Yarin, A. L., Zussman, E., Wendorff, J. H., and Greiner, A. Material encapsulation and transport in core–shell micro/nanofibers, polymer and carbon nanotubes and micro/nanochannels. J. Mater. Chem. 17 (2007), 2585–2599.

Yilmaz, F., and Gundogdu, M. Y. A critical review on blood flow in large arteries; relevance to blood rheology, viscosity models, and physiologic conditions. Korea-Australia Rheology Journal 20, 4 (2008), 197–211.

Yue, P., Zhou, C., Feng, J. J., Ollivier-Gooch, C. F., and Hu, H. H. Phase-field simulations of interfacial dynamics in viscoelastic fluids using finite elements with adaptive meshing. Journal of Computational Physics 219, 1 (2006), 47 – 67.

Zhang, L., Zhao, L., Yu, Y., and Chen, C. Removal of lead from aqueous solution by non-living rhizopus nigricans. Water Research 32, 5 (1998), 1437 – 1444.

Zhang, Y., Lee, M. W., An, S., Sinha-Ray, S., Khansari, S., Joshi, B., Hong, S., Hong, J.-H., Kim, J.-J., Pourdeyhimi, B., Yoon, S. S., and Yarin, A. L. Antibacterial activity of photocatalytic electrospun titania nanofiber mats and solution-blown soy protein nanofiber mats decorated with silver nanoparticles. Catalysis Communications 34 (2013), 35 – 40.

Zhuang, X., Shi, L., Jia, K., Cheng, B., and Kang, W. Solution blown nanofibrous membrane for microfiltration. Journal of Membrane Science 429 (2013), 66 – 70.

12. CURRICULUM VITAE

ALEXANDER KOLBASOV

Department of Mechanical and Industrial Engineering University of Illinois at Chicago (UIC)

842 West Taylor Street, M/C 251, Room 2039ERF Chicago, Illinois 60607-7022

Tel: (312) 714-3910 Fax: (312) 413-0447

Research Interests

- Biopolymer materials and bio-waste utilization in nano-textured materials.
- Solution blowing and electrospinning of nanofibers.
- Mechanical behavior of nonwoven materials.
- Rheology of non-Newtonian fluids.

Education

Doctoral Candidate, Mechanical and Industrial Engineering, University of Illinois at Chicago, Chicago Illinois, Jan 2014-present.

B.S., Mechanical Engineering, Illinois Institute of Technology, Chicago Illinois, 2006-2010

Teaching Experience

Teaching Assistant

- Introduction to Thermodynamics (ME 205), Graded students' performances of class and held regular office hours.
- Fluid mechanics I (ME 211), Conducted and coordinated laboratory experiments and held regular problem solving sessions. Graded students' performances of class.
- Intermediate Thermodynamics (ME 325) Graded students' performances of class and held regular office hours.

Professional Experience

University of Illinois at Chicago – IL

- Project Support Engineer at UTC Aerospace Systems 2011-2013
- Teaching Assistant, 2015,2016,2017,2018,2019
- Research Assistant, 2015,2016,2017,2018

Published Work

- Kolbasov A., Comiskey P., Sahu R., Sinha-Ray S., Yarin A., Sikarwar B., Kim S,. Jubery T,. Attinger D. (2016) Blood rheology in shear and uniaxial elongation. Rheologica Acta, 55(11-12), 901-908
- Kolbasov, A., Sinha-Ray, S., Joijode, A., Hassan, M. A., Brown, D., Maze, B., Pourdeyhimi, B., and Yarin, A. L. (2016) Industrial-scale solution blowing of soy protein nanofibers. Industrial & Engineering Chemistry Research 55, 1, 323–333
- Kolbasov, A., Sinha-Ray, S., Yarin, A. L., & Pourdeyhimi, B. (2017). Heavy metal adsorption on solution-blown biopolymer nanofiber membranes. Journal of Membrane Science, 530, 250-263

- Kolbasov, A., Sinha-Ray, S., & Yarin, A. L. (2019). Theoretical and experimental study of punched laminate composites protected by outer paper layer. Journal of the Mechanics and Physics of Solids, 128, 117-136

Computational Skills
FORTRAN, MATLAB, Origin Pro.

Characterization Skills
- Scanning Electron Microscopy.
- Transmission Electron Microscopy.
- Atomic Absorption Spectroscopy.